RIJKSUNIVERSITEIT GRONINGEN

Stress and dislocations in thin metal layers

Proefschrift

ter verkrijging van het doctoraat in de
Wiskunde en Natuurwetenschappen
aan de Rijksuniversiteit Groningen
op gezag van de
Rector Magnificus, dr. F. Zwarts,
in het openbaar te verdedigen op
vrijdag 3 september 2004
om 16.15 uur

door

Lucia Nicola

geboren op 25 februari 1973
te Bolzano, Italië

Promotor:	Prof. dr. ir. E. van der Giessen
Beoordelingscommissie:	Prof. dr. J.Th.M. De Hosson
	Prof. dr. H.A. De Raedt
	Prof. dr. B.J. van Wees

ISBN 90-77172-11-4

Netherlands Institute
for Metals Research

This research was carried out under project number MS97007 in the framework of the Strategic Research Program of the Netherlands Institute for Metals Research in the Netherlands (www.nimr.nl).

Contents

Introduction

Since ancient times, metal has primarily served as a material for structural, load-bearing applications and for the fabrication of tools. Thus, the importance of the mechanical properties of metals has been recognized since many centuries. The strong interest in understanding the mechanical behavior of structural materials has led to much research and, to date, to an appreciably good knowledge of bulk metal behavior.

With the advent of the information revolution, metal has found a new field of applicability in the electronics industry. Integrated circuits and electronic devices make wide use of metal in the form of thin films and connecting wires. In such kind of applications, metal does not serve as structural material and seems to not have any load to bear. The same holds for all the other materials used in electronics. For this reason the mechanical properties of electronic components have been considered unimportant for quite a long time. Materials to be used, have always been selected on the basis of their electronic, magnetic or optical properties and not on the base of their mechanical reliability.

Quite unexpectedly, however, a significant number of electronic components turned out to fail mechanically, sometimes during operation and sometimes already during processing. Together with the overall tendency of making the devices smaller and smaller, the frequency of mechanical failure has increased. This observation has promoted extensive research on the mechanical behavior of small structures in the last few decades.

What has been found is that classical continuum plasticity is not applicable when at least one of the dimensions of the structure is in the micrometer range. When this happens, characteristic material length scales, such as the Burgers vector of the dislocation, dimensions related to dislocation patterning or to the microstructure, are not negligible anymore because they are comparable to the structure dimensions. These characteristic material lengths are related to strain and stress gradients which develop in the small structure when it is subjected to loading, in a way that is not well understood. Clearly, the dimensional constraint has an effect on plastic relaxation of small metal structures, like thin films. Several

experiments have shown that thin metal films on a rigid substrate strengthen more than the corresponding bulk material. Moreover, with decreasing thickness the films show less and less plasticity. This phenomenon, frequently referred to as the thin film size effect, is still under investigation and this thesis is intended as a contribution to its understanding.

Thermal stress in thin films

Thermal stress is one of the main causes for the observed failure of electronic devices. In those structures, materials with very different elastic properties are packed closely together with deposition techniques that require high temperatures. During cooling to room temperature high thermal stresses develop because the various components have different thermal expansion coefficients. Plastic deformation in the metallic film can relax these stresses. Since plastic relaxation appears to be hindered in small metal structures, the residual stress present after manufacturing can be high enough to induce fracture or delamination of the thin metal films involved. Thermal stresses and relaxation also occur in service when devices are switched on or off.

When a thin metal film is thermally cycled on a rigid substrate, the imposed thermal strain is accommodated as elastic and plastic strain in the film, so that

$$\varepsilon_{\text{thermal}} + \varepsilon_{\text{elastic}} + \varepsilon_{\text{plastic}} = 0, \tag{1}$$

where, for a change in temperature ΔT, the thermal strain can be written as

$$\varepsilon_{\text{thermal}} = \Delta\alpha\Delta T. \tag{2}$$

Here $\Delta\alpha$ is the difference in the linear thermal expansion coefficients between the film and the substrate.

Let us assume that the film is elastic and isotropic. Since the film is thin, it can safely be assumed to be in a state of uniform plane stress, i.e.,

$$\sigma_{zz} = \sigma_{xz} = \sigma_{yz} = 0, \tag{3}$$

z being the direction normal to the film-substrate interface, while the in-plane principal stresses σ_x and σ_y are identical because of symmetry and $\sigma_{xy} = 0$. The elastic stress–strain relationship (Hooke's law) takes the simple form

$$\varepsilon_x = \varepsilon_y = \frac{1}{E}(\sigma_x - \nu\sigma_y), \tag{4}$$

with E being Young's modulus and ν Poisson's ratio. Since the thermal strain is also the same in x- and y-direction, the biaxial stress becomes

$$\sigma = \frac{E}{(1-\nu)}\Delta\alpha\Delta T. \tag{5}$$

Thus, in curves representing stress versus temperature the slope can never exceed the thermoelastic slope $[E/(1-\nu)]\Delta\alpha$. Deviation from the elastic slope gives a measure of plasticity in the film.

The stress in an elastic film is independent of film thickness. A dependence on thickness does also not appear by accounting for plasticity in the classical way. Yield functions do not depend on film thickness, neither do hardening laws. But, yield strength and hardening of real thin layers do, as we will see in the following section.

Experimental observation

Figure 1 shows typical experimental stress–temperature curves for thin films under thermal cycling. Wafer curvature measurements have been performed on bare and passivated gold films on a silicon substrate. The figure shows that, after cooling by 600K, the biaxial stress in films of thickness $h = 0.75\mu$m (in Fig. 1a) is more relaxed than in films of thickness $h = 0.5\mu$m (in Fig. 1b). The presence of a passivation layer influences the behavior of the thinner film by increasing its hardness even further.

Experimental techniques

The traditional technique used to experimentally measure the stress in a thin film on a substrate is the wafer curvature technique. The method is based on the observation that the stress in the film exerts forces on the substrate that tend to bend the substrate elastically. By measuring the curvature of the substrate the biaxial stress in the film is calculated through Stoney's equation

$$\sigma = \frac{1}{6}\frac{E_s}{1-\nu_s}\frac{h_s}{h_f}\frac{h_s}{R}, \tag{6}$$

where h_s and h_f are the substrate and film thickness, R the substrate curvature. It should be noted that Stoney's equation does not contain the elastic constants of the

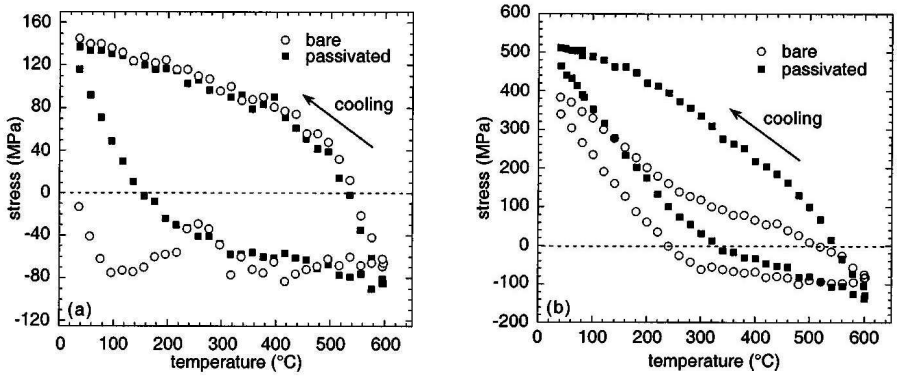

Figure 1 Thermal cycling of gold films on silicon of thickness (a) $h = 0.75\mu$m and (b) $h = 0.5\mu$m (from [1]).

film, only those of the substrate (which are generally known). The influence of the film response is negligible as long as the thickness of the film is much smaller than the thickness of the substrate. Equation (6) is valid if the film deforms elastically and/or plastically, but obviously does not hold in case the substrate also becomes plastic.

Various techniques are available to measure the change in curvature; the most widely used ones are X-ray diffraction, optical interferometry and laser scanning. The wafer curvature technique is well-suited for in-situ stress measurements during heating and cooling of films and is commonly used to obtain stress–temperature curves. Since this is an indirect method, it only measures the average stress in the film, possible variations of the stress through the film thickness are not detected. In principle, X-ray diffraction would enable to see stress gradients across the film thickness by directly measuring the lattice strain in the film. Unfortunately the penetration depth of the beam cannot be tuned accurately and the presence of strain gradients across fractions of a micrometer are very difficult to detect. The most accurate technics in this respect are the glancing angle X-ray diffraction [2] and the energy-filtered electron diffraction techniques [3].

Freund-Nix model

Considering that stress relaxation in thin metal films occurs by dislocation glide, as shown experimentally for instance by Dehm et al. [4] (see Fig. 2), Freund [5] and Nix [6] proposed a model based on the motion of a single threading dislocation. Threading dislocations are dislocations that are present in the substrate before the film is deposited and grow naturally into the film during film growth by a glide and climb process, reaching the free surface. When stress develops in the film the part of threading dislocation in the film start to move, while the part in the substrate stays stationary. Thus, the dislocation bends over in the film as it moves and eventually leaves a misfit dislocation in the film. The minimum biaxial stress necessary to move a dislocation in the film, depositing dislocation length at the film–substrate interface, is given by

$$\sigma = \frac{\sin\phi}{\cos\phi\cos\lambda}\frac{b}{2\pi(1-\nu)h}\left[\frac{\mu_f\mu_s}{\mu_f+\mu_s}\ln\frac{\beta_s h}{b}\right], \tag{7}$$

where ϕ is the angle between the normal to the plane of the film and the normal to the glide plane, λ is the angle between the normal to the plane of the film and the Burgers vector b, and μ_f and μ_s are the elastic shear moduli of film and substrate. One of the key characteristics of the model is that it predicts that the stress is inversely proportional to the film thickness h.

The limitation of this model is that it only accounts for a single dislocation and its interaction with the interface. Since it neglects the effect of interaction among dislocations or between dislocations and other obstacles that might be present in the film, the model tends to underestimate the stress measured experimentally. For this reason, this thesis is concerned with the analysis of stress relaxation caused by the collective behavior of many dislocations. In addition to thin films, also interconnect lines are studied.

References

[1] O.S. Leung, A. Munkholm, S. Brennan and W.D. Nix, J. Appl. Phys. **88** (2000) 1389.

[2] B.A. van Brussel and J.Th. De Hosson, Appl. Phys. Lett. **64** (1994) 1585.

[3] S. Krämer, J. Mayer, C. Witt, A. Weickenmeier and M. Rühle, Ultramicroscopy **81** (2000) 245.

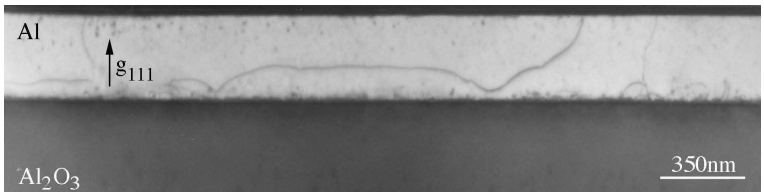

Figure 2 TEM image of a threading dislocation in a thin film (from [4]).

[4] G. Dehm, B.J. Inkson, T.J. Balk, T. Wagner, and E. Arzt, Mat. Res. Soc. Symp. Proc. **673** (2001) paper P2.6.

[5] L.B. Freund, J. Appl. Mech. **54** (1987), 553.

[6] W.D. Nix, Metall. Trans **20A** (1989) 2217.

Chapter 1

Discrete dislocation plasticity

Plastic deformation of crystalline metals is caused by glide of a large number of dislocations. In the case of massive pieces of material, keeping track of the motion of all the individual dislocations would be a very impractical way of measuring plastic relaxation. Fortunately, plasticity in sufficiently large samples often can be efficiently described by continuum models, which neglect the discrete nature of dislocations and only account for the effect of their collective motion. This is made possible by the fact that dislocations are so small with respect to the dimensions of the sample.

However, when one of the dimensions of the specimen is at the micrometer scale, these requirements stop being valid and continuum models may cease to be useful. In confined small structures, dislocation loops cannot form and move as freely as in bulk metal. Moreover, the patterns that dislocations form in order to reduce the stress state in the material, can be comparable in size to the size of the sample itself. If this happens, the stress state associated to the patterning needs to be taken into account.

The above forms the motivation to study plasticity in thin metal films using a model that considers all the dislocations which are generated during the deformation process, their stress and strain fields, their motion and their interactions.

1.1 About the method

Various discrete dislocation models have been presented in the last 15 years which describe individual dislocations as line singularities in an elastic medium, e.g. [1]–[10]. This seems to be a good representation of a dislocation beyond 10 atomic distances from the dislocation core [11, 12, 13]. The framework we will use in this thesis is the one formulated in 1995 by Van der Giessen and Needleman [14] to solve quasi-static boundary value problems for dislocated bodies. It is based on the formulation of Lubarda et al. [5] for equilibrium dislocation arrangements:

stress, strain and displacement fields in the body are given as superposition of the fields describing the dislocations as if they were singularities in an infinite elastic body and complementary fields which enforce the prescribed boundary conditions on the actual body. The Van der Giessen-Needleman approach describes the evolution of the dislocation structure during quasi-static deformation of the body. This is done by using constitutive rules for dislocation glide, nucleation and annihilation of the kind proposed by Kubin [3]. The simulations follow an incremental procedure: at each time step the fields are calculated in the body and then the dislocation structure is updated.

1.1.1 The dislocated body at a given time increment

At a generic time of deformation the body contains a certain distribution of dislocations, see Fig. 1.1(a). They are regarded as line defects in the body which is elsewhere described as a linear elastic continuum. At the boundary $S = S_u \cup S_f$ mixed periodic boundary conditions are prescribed: S_f is the portion of the boundary on which tractions $\boldsymbol{T}_0$ are prescribed, S_u is the portion of the boundary on which displacements $\boldsymbol{u}_0$ are prescribed and $\boldsymbol{n}$ is the outer unit normal to S.

As shown in Fig. 1.1 the current state of the body in terms of the displacement, strain and stress fields is calculated as the sum of two contributions:

$$\boldsymbol{u} = \tilde{\boldsymbol{u}} + \hat{\boldsymbol{u}}\,, \quad \boldsymbol{\varepsilon} = \tilde{\boldsymbol{\varepsilon}} + \hat{\boldsymbol{\varepsilon}}\,, \quad \boldsymbol{\sigma} = \tilde{\boldsymbol{\sigma}} + \hat{\boldsymbol{\sigma}}\,. \tag{1.1}$$

Here, the $\tilde{(\,)}$-fields are the superpositions of the fields of the individual dislocations as if they were in in infinite space,

$$\tilde{\boldsymbol{u}} = \sum_I \boldsymbol{u}^{(I)}\,, \quad \tilde{\boldsymbol{\varepsilon}} = \sum_I \boldsymbol{\varepsilon}^{(I)}\,, \quad \tilde{\boldsymbol{\sigma}} = \sum_I \boldsymbol{\sigma}^{(I)}\,. \tag{1.2}$$

(the superscript (I) denotes the Ith dislocation), and are singular at the positions of the dislocations. The analytical expression for these infinite-body fields can be found in textbooks [15, 16].

The $\hat{(\,)}$-fields in (1.1) represent the image fields that correct for the actual boundary conditions on S. Provided that the displacement fields are continuous on S_u, the $\hat{(\,)}$-fields are smooth and can therefore be solved for by numerical techniques such as the finite element method. The governing equations for the $\hat{(\,)}$ fields are

$$\left.\begin{array}{l} \boldsymbol{\nabla}\cdot\hat{\boldsymbol{\sigma}} = \boldsymbol{0} \\ \hat{\boldsymbol{\varepsilon}} = \mathrm{sym}(\boldsymbol{\nabla}\otimes\hat{\boldsymbol{u}}) \end{array}\right\} \text{ in } V \tag{1.3}$$

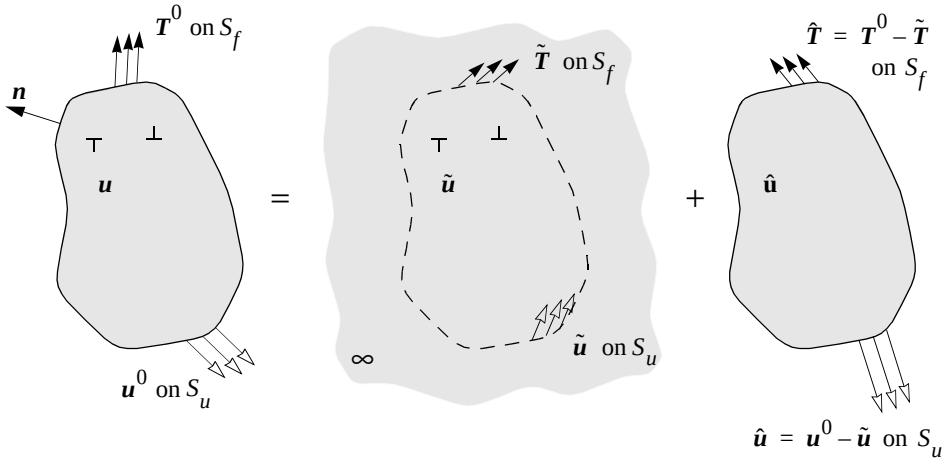

Figure 1.1 Decomposition of the problem for the dislocated body into the problem of interacting dislocations in the homogeneous infinite solid ($\tilde{(\,)}$-fields) and the complementary problem for the nonhomogeneous body without dislocations ($\hat{(\,)}$-fields).

$$\hat{\boldsymbol{\sigma}} = \boldsymbol{\mathcal{L}} : \hat{\boldsymbol{\varepsilon}} \quad \text{in } V \tag{1.4}$$

$$\begin{aligned} \boldsymbol{n}\cdot\hat{\boldsymbol{\sigma}} = \hat{\boldsymbol{T}} &= \boldsymbol{T}_0 - \tilde{\boldsymbol{T}} \quad \text{on } S_f \\ \boldsymbol{u} = \hat{\boldsymbol{U}} &= \boldsymbol{u}_0 - \tilde{\boldsymbol{U}} \quad \text{on } S_u \end{aligned} \tag{1.5}$$

Here, $\boldsymbol{\mathcal{L}}$ is the tensor of elastic moduli of the body, which is taken to be isotropic. While the formulation holds in general, the problems addressed in this thesis are two dimensional.

1.2 The evolving dislocation ensemble

The connection between the stress state in the body and the evolution of the dislocation structure is made by a set of constitutive rules. These rules relate the resolved shear stress on the slip planes in the body to the dislocation activity. The constitutive relations control nucleation, glide, annihilation and pinning of dislocations at an obstacle. Figure 1.2 shows schematically the main steps of the program used to simulate dislocation dynamics.

1.2.1 Nucleation

Nucleation occurs by activation of Frank-Read sources, already present in the material due to previous plastic activity. The dislocation sources are positioned on the slip planes and their density is taken to be constant during the simulation. A certain stress must act on a source to make it operate by bowing out the Frank-Read segment and form a new dislocation loop.

In the two-dimensional formulation used in this thesis, we just consider traces of the slip planes intersecting the plane of deformation and Frank-Read segments are approximated as point sources on those traces. The dislocation loop generated by the source, intersects the plane of deformation in two points. Assuming that the loop opens and expands symmetrically with respect to the source, these two points are two purely edge dislocations of opposite sign. Since relaxation of thin films is controlled by glide of the straight part of dislocation loops, keeping track of the motion of edge dislocations pairs seems to be an appropriate way to approach the thin film problem in two dimensions.

Three parameters are associated to each source: a critical strength τ_{nuc} necessary to create the new dislocation loop, the critical time t_{nuc} required for its formation and the diameter of the loop at nucleation, L_{nuc}. This distance is such that the attractive stress field that the dislocations exert on each other is equilibrated by the resolved shear stress at nucleation (τ_{nuc}),

$$L_{\text{nuc}} = \frac{\mu}{2\pi(1-\nu)}\frac{b}{\tau_{\text{nuc}}}\,. \tag{1.6}$$

1.2.2 Glide

Glide of the dislocation loop on the slip plane is driven by the Peach-Koehler force. The component of the Peach-Koehler force acting on the I-th dislocation is

$$f^{(I)} = \boldsymbol{n}^{(I)} \cdot (\hat{\boldsymbol{\sigma}} + \sum_{J \neq I} \boldsymbol{\sigma}^{(J)}) \cdot \boldsymbol{b}^{(I)}\,, \tag{1.7}$$

where $\boldsymbol{t}^{(I)}$ is the unit vector tangent to the I-th dislocation line and $\boldsymbol{b}^{(I)}$ is its Burgers vector. For edge dislocations equation 1.7 reduces to:

$$f^{(I)} = \tau^{(I)} b^{(I)}, \tag{1.8}$$

where τ^I is the resolved shear stress on the slip plane containing dislocation I.

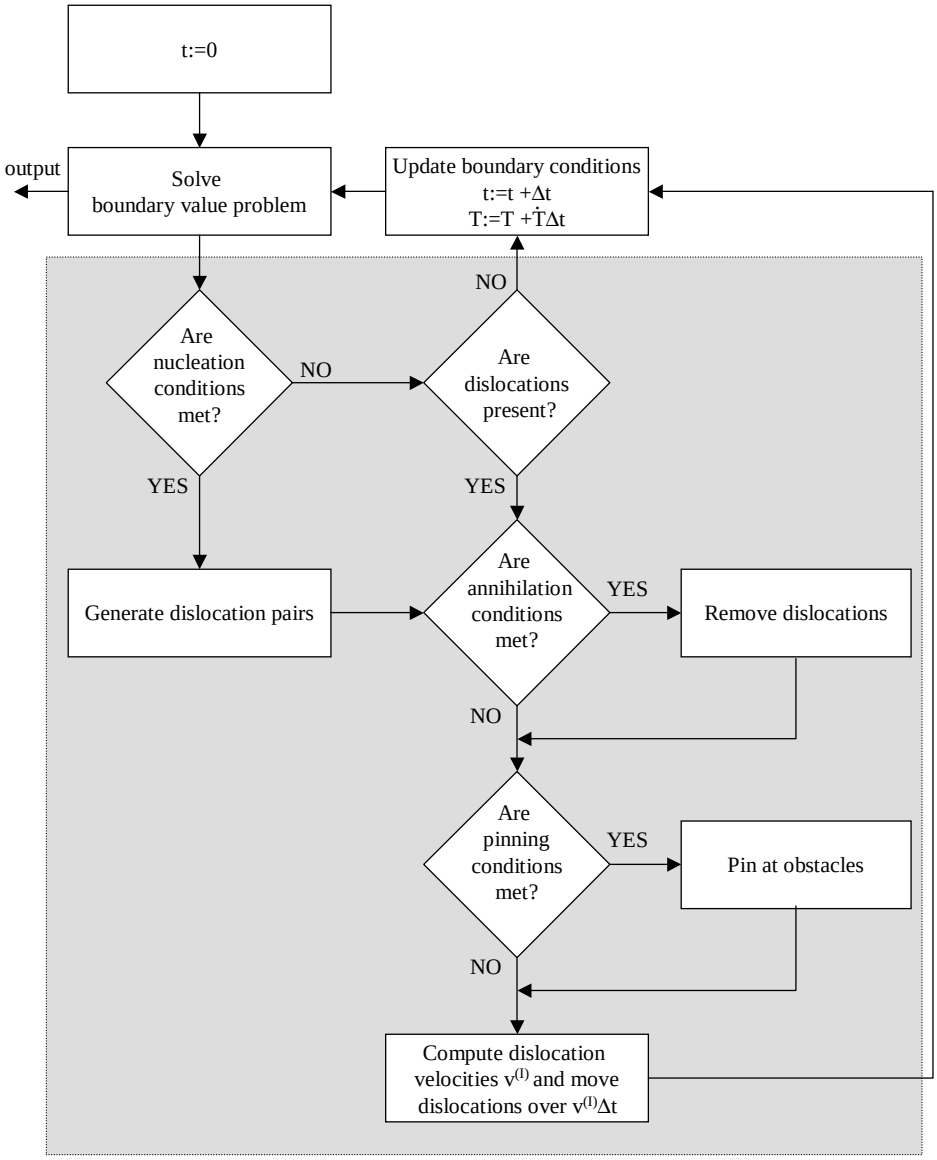

Figure 1.2 Schematic representation of the program. The computations which treat dislocation dynamics are listed in the gray box.

In this quasi-static framework glide is assumed to be drag controlled; thus the velocity of dislocation I, v^I, in the direction of $\boldsymbol{s}^I$ is proportional to the resolved

shear stress according to the drag relation

$$\tau^{(I)} b^{(I)} = B v^{(I)} \tag{1.9}$$

with B the drag coefficient.

1.2.3 Pinning at obstacles

Dislocation glide can be hindered in real metals by different kinds of obstacles like precipitates, grain boundaries or other dislocations on intersecting slip planes. In principle it is possible to map the defects with their properties from a three dimensional crystal into a two dimensional representation [17]. Here, the obstacles are just modeled as point obstacles on the slip planes at which dislocations get pinned. Each obstacle is characterized by a critical strength, τ_{obs}. As long as the resolved shear stress acting on the pinned dislocation is lower than the obstacle strength, the dislocation cannot overtake the obstacle. Often the presence of an obstacle causes the formation of a dislocation pile-up which induces a high shear stress on the leading dislocation. If the shear stress exceeds the critical strength of the obstacle, the dislocation is released.

1.2.4 Annihilation

Occasionally, dislocation loops collapse on themselves, because the stress state which caused their nucleation suddenly decreases, or is not sufficiently large to promote their growth. When this happens the couple of opposite signed edge dislocations (which represent the loop's cross-section) approach each other until they annihilate. This is modeled by removing dislocations of opposite sign from the simulation when they are on the same slip plane closer to each other than the critical material-dependent distance L_{ann}.

References

[1] A.N. Gulluoglu, D.J. Srolovitz, R. LeSar and P.S. Lomdahl, Scripta Metall. **23** (1989) 1347.

[2] R.J. Amodeo and N.M. Ghoniem, Phys. Rev. B **41** (1990) 6968.

[3] L.P. Kubin, G. Canova, M. Condat, B. Devincre, V. Pontikis and Y. Bréchet, in Nonlinear Phenomena in Materials Science II (edited by G. Martin and L.P. Kubin), Sci-Tech, Vaduz (1992) 455.

[4] A.N. Gulluoglu and C.S. Hartley, Model. Simul. Mater. Sci. Eng. **1** (1993) 383.

[5] V. Lubarda, J.A. Blume and A. Needleman, Acta Metall. Mater. **41** (1993) 625.

[6] X.F. Fang and W. Dahl, Mater. Sci. Eng. **A164** (1993) 300.

[7] I. Groma and G.S. Pawley, Mater. Sci. Eng. **A164** (1993) 306.

[8] Y. Bréchet, G. Canova, L.P. Kubin, Acta Mater. **44** (1996) 4261.

[9] M.C. Fivel, T.J. Gosling, G.R. Canova, Model. Simul. Mater. Sci. Eng. **4** (1996) 581.

[10] H.M. Zbib, M. Rhee and J.P. Hirth, Int. J. Mech. Sci. **40** (1998) 113.

[11] H.C. Choi, A.F. Schwartzman and K.-S. Kim, Mater. Sci. Symp. Proc. **239** (1992) 419.

[12] V. Vitek, Prog. Mat. Sci. **3** (1992) 1.

[13] R. Gallego, M. Ortiz, Model. Simul. Mater. Sci. Eng. **1** (1993) 383.

[14] E. Van der Giessen, A. Needleman, Simul. Mater. Sci. Eng. **3** (1995) 689.

[15] F.R.N. Nabarro, Theory of crystal dislocations, (Oxford: Oxford University Press) (1967).

[16] J.P. Hirth and J. Lothe, Theory of dislocations, (New York: McGraw-Hill) (1968).

[17] A. Roos, J.Th.M. De Hosson, E. Van der Giessen, Computational Material Science **20** (2001) 19.

Chapter 2

Size effects in single crystal thin films*

An important source of stress in thin films arises from the thermal mismatch between the film and the substrate. Experiments that reveal this, typically involve cooling, heating or an alternating sequence of cooling and heating, with the average stress in the film recorded by wafer curvature measurements [1, 2] or by X-ray diffraction [1, 3, 4]. On cooling a film from an almost stress-free state at a relatively high temperature, the deformation is initially elastic, but as cooling proceeds plastic deformation eventually occurs. When the film is re-heated, the stress level in the film at first reduces (in absolute value) elastically, with reverse plastic deformation subsequently occurring for a sufficiently large temperature change. Reverse plastic deformation occurs earlier and stress levels increase more rapidly for thinner films. These effects have been observed for fine-grained as well as coarse-grained films [2] and also in passivated films [1, 3]. Unfortunately, experimental results on single crystalline films are not yet available, due to the difficulty in the sample preparation.

This size effect is not captured by conventional continuum plasticity theories because they lack an internal length scale. Nonlocal phenomenological continuum plasticity theories have been proposed, e.g. [5]–[9], that can capture size effects within a phenomenological theory of plasticity. There have also been studies aimed at explaining the thin film size effect based on considerations of dislocation nucleation and motion. In addition to arguments that make reference to well-known concepts such as the Hall-Petch relation [2], single dislocation models have

*Based on *Discrete dislocation analysis of size effects in single crystal thin films*, L. Nicola, E. Van der Giessen, A. Needleman, J. Appl. Phys. **93** (2003) 5920 and on *Plastic response of thin films due to thermal cycling*, L. Nicola, E. Van der Giessen, A. Needleman, Proceedings of the IUTAM Symposium on Multiscale Modeling and Characterization of Elastic-Inelastic Behavior of Engineering Materials held in Marrakech, Morocco, 20–25 October 2002, ed. by S. Ahzi, M. Cherkaoui, M.A. Kahleel, H.M. Zbib, M.A. Zikry, B. LaMatina, Kluwer Academic Publishers (2002) 97.

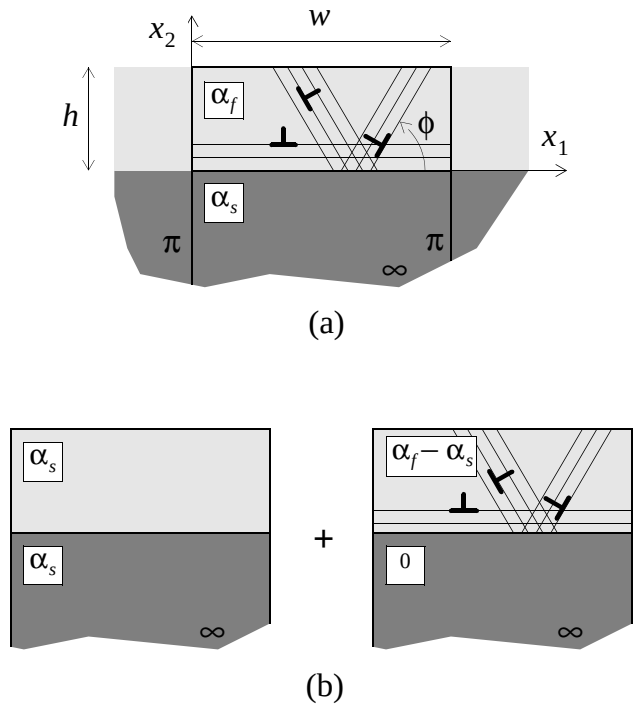

Figure 2.1 (a) Geometry of the film-substrate problem studied in this chapter. The symbol π indicates periodicity. (b) Decomposition of the unit-cell problem into a thermo-elastic problem and a plastic relaxation problem. The solution of the latter part uses another decomposition, following [17]. (See fig 1.1.)

been proposed for thin films. As already mentioned in the preface, Freund [10] and Nix [11] have proposed a model based on the confined motion of a threading dislocation in a single crystal film, which suggests that the yield strength scales with the film thickness h as h^{-1} . Similar single dislocation arguments have been used for polycrystalline films in [13, 14]. Hartmaier et al. [15] have discussed the role of thickness on the possibility of generation of new dislocations.

In this chapter we carry out a dislocation dynamics simulation of the evolution of plastic deformation in single crystal thin films subject to thermal loading.

2.1 Problem formulation

We consider a single-crystalline film, of thickness h, perfectly bonded to an elastic half-plane, as illustrated in Fig. 2.1. A two-dimensional, plane strain study ($\varepsilon_{33} = 0$) is carried out. The two-dimensional nature of the model is motivated by the consideration that it is the long straight edge part of threading dislocations that provides most of the plastic relaxation. Three dimensional effects such as line tension and the interaction between dislocation lines not parallel to existing misfit dislocation lines along the interface, as discussed in [11], are not accounted for. The substrate remains elastic, while the film can relax by dislocation activity on a set of discrete slip systems defined by the angle ϕ relative to the interface, see Fig. 2.1a. The dislocations are all of edge character with a Burgers vector in the x_1-x_2-plane of length b. Individual dislocations are modeled as singularities in an isotropic thermo-elastic continuum.

The boundary value problem is governed by the equilibrium and compatibility equations,

$$\sigma_{ij,j} = 0\,, \quad \varepsilon_{ij} = \frac{1}{2}(u_{i,j} + u_{j,i}) \tag{2.1}$$

where σ_{ij} denotes the stresses, ε_{ij} the strains and u_i the displacements; $()_{,i}$ denotes partial differentiation with respect to x_i.

The constitutive relation is specified by

$$\varepsilon_{ij} = \frac{1+\nu}{E}\left(\sigma_{ij} - \frac{\nu}{1+\nu}\delta_{ij}\sigma_{kk}\right) + \alpha\Delta T\delta_{ij}\,. \tag{2.2}$$

Here, ΔT is the temperature change from the undeformed state. The linear thermal expansion coefficient α for the film is denoted by α_f and that for the substrate by α_s; Young's modulus E and Poisson's ratio ν are taken to be identical for the film and the substrate. In [16] it was found that elastic property differences did not qualitatively affect the predictions and quantitatively even a factor of two difference in E changed predictions by only a few percent. The values of $E = 70$ GPa and $\nu = 0.33$ used in the calculations are representative of aluminum.

To implement the boundary conditions, the problem is decomposed in two linearly additive parts as illustrated in Fig. 2.1b. One part treats the unconstrained thermal expansion of the film and substrate as if they have the same thermal expansion coefficient, $\alpha_\mathrm{f} = \alpha_\mathrm{s}$. The solution to this problem is

$$\varepsilon^{\mathrm{th}}_{ij} = (1+\nu)\alpha_\mathrm{s}\Delta T\delta_{ij}\,, \quad \sigma^{\mathrm{th}}_{ij} = 0 \quad (i,j = 1,2) \tag{2.3}$$

for both film and substrate (the factor $1+\nu$ is due to the plane strain constraint in the x_3-direction). Since the stresses vanish everywhere, this part of the solution does not interact with the dislocations.

The other part of the solution, which is denoted by $(\,)'$ and pertains to the problem sketched in Fig. 2.1b, describes the stress which builds up in the film due to the thermal mismatch between the film and the substrate, and accounts for the presence of the dislocations. This problem pertains to a film with a thermal expansion coefficient $\alpha = \alpha_f - \alpha_s$ on a substrate that does not undergo thermal expansion. The solution to the full problem is

$$u_i = u_i^{\rm th} + u_i', \quad \varepsilon_{ij} = \varepsilon_{ij}^{\rm th} + \varepsilon_{ij}', \quad \sigma_{ij} = \sigma_{ij}^{\rm th} + \sigma_{ij}'. \tag{2.4}$$

With plasticity arising from the collective motion of discrete dislocations, the $(\,)'$ solution is not independent of x_1. As shown in Fig. 2.1a, a unit cell is introduced in order to reduce the computation to one over a finite region. The film-substrate system is taken to be periodic in the x_1-direction with period w. The boundary conditions on the unit cell consist of the stress-free surface conditions

$$\sigma_{12}'(x_1,h) = \sigma_{22}'(x_1,h) = 0 \tag{2.5}$$

and the periodicity conditions

$$u_i'(0,x_2) = u_i'(w,x_2), \tag{2.6}$$

while traction continuity implies continuity of σ_{12}' and σ_{11}' at the cell boundaries $x_2 = 0$ and $x_2 = w$. The $()'$ fields are governed by (2.1)–(2.2) with the appropriate substitutions for α according to Fig. 2.1b. In the absence of dislocations, the solution is

$$\varepsilon_{ij}' = 0, \quad \sigma_{11}' = -\frac{(\alpha_f - \alpha_s)E\Delta T}{(1-\nu)}, \quad \sigma_{ij}' = 0 \text{ otherwise} \quad (i,j = 1,2) \tag{2.7}$$

for the film and $\varepsilon_{ij}' = \sigma_{11}' = 0$ everywhere in the substrate. The solution (2.7) can be interpreted as resulting from the film freely expanding by $(\varepsilon_{11}^{\rm th})_f = (1+\nu)(\alpha_f - \alpha_s)\Delta T$ and subsequently being compressed by a stress σ_{11}' to remove the expansion so that the film fits on the undeformed substrate.

In the presence of dislocations, the governing equations, subject to (2.5)-(2.6), are solved by decomposing the $(\,)'$ field quantities into two additive parts, as described in [17], so that the stress, strain and displacement fields in the film are given by:

$$u_i' = \tilde{u}_i + \hat{u}_i, \quad \varepsilon_{ij}' = \tilde{\varepsilon}_{ij} + \hat{\varepsilon}_{ij}, \quad \sigma_{ij}' = \tilde{\sigma}_{ij} + \hat{\sigma}_{ij}. \tag{2.8}$$

Here, the $\tilde{(\,)}$-fields are the superpositions of the fields of individual dislocations in infinite space, e.g.

$$\tilde{\sigma}_{ij} = \sum_I \sigma_{ij}^{(I)}$$

(the superscript (I) denotes the Ith dislocation), and are singular at the positions of the dislocations. The $\hat{(\,)}$-fields in (2.8) are image fields that are superimposed on the individual dislocation fields so that the boundary conditions on the unit cell are satisfied. These fields are smooth and their solution is obtained by a finite element method. The infinite space $\tilde{(\,)}$-fields are constructed in such a way that they reflect the periodicity in the problem; i.e. the field corresponding to each dislocation in the cell is the field, with periodicity w, due to this dislocation and all its replicas in the other cells making up the film. The closed-form expressions for these fields are given in [18]. The use of periodic discrete dislocation fields avoids the possibility of artificial dislocation patterning that may be induced when using a cutoff distance [19].

Special attention is needed for dislocations that glide out of the film. They leave the film, but they cannot be removed from the set of dislocations in the calculation because they contribute to a slip displacement and to the resulting step at the free surface. This is accounted for by virtually extending the slip planes above the film and positioning a dislocation at a distance h above the free surface, i.e. at $x_2 = 2h$, once it leaves the film. This virtual dislocation produces stresses $\tilde{\sigma}_{12}$ and $\tilde{\sigma}_{22}$ on the stress-free surface (even though it is outside the film). These stresses are corrected by the $\hat{(\,)}$-fields. The virtual dislocations at $x_2 = 2h$ are sufficiently far away from the surface that the finite element solution can accurately describe the necessary correction.

Initially, the film-substrate system is at a high temperature and stress free. At each step of the simulation a temperature increment $\Delta T = \dot{T}\Delta t$ is prescribed and the boundary value problem is solved for all field quantities in the cell. For each time step, the dislocation structure is updated and then the updated solution for all field quantities is obtained as described above. As suggested by Kubin et al. [20], the following dislocation mechanisms are accounted for through constitutive rules: (i) dislocation glide; (ii) dislocation generation and (iii) annihilation; (iv) pinning at obstacles. All of these are governed by the Peach-Koehler force, which is computed as

$$f^{(I)} = n_i^{(I)} \left(\hat{\sigma}_{ij} + \sum_{J \neq I} \sigma_{ij}^{(J)} \right) b_j^{(I)} ,$$

taking advantage of the fact that $\sigma_{ij}^{\text{th}} = 0$ according to (2.3).

Dislocation glide is taken to be drag controlled so that the velocity of dislocation I is directly proportional to the Peach-Koehler force, $f^{(I)} = Bv^{(I)}$, with B the drag coefficient, which is taken to have the value $B = 10^{-4}$Pa s. Annihilation of two dislocations with opposite Burgers vector occurs when they approach each other within an annihilation distance $L_{\text{e}} = 6b$. Generation of new dislocations is incorporated through a distribution of Frank-Read sources. In two dimensions, these are point sources which generate a dipole when the Peach-Koehler force on the source exceeds a critical value $\tau_{\text{nuc}}b$ during a time span $t_{\text{nuc}} = 10$ ns. The sign of the dipole is determined by the direction of the force. The distance between the two dislocations, L_{nuc}, is set so that they will not immediately collapse and annihilate under an applied shear stress τ_{nuc}, i.e.

$$L_{\text{nuc}} = \frac{\mu}{2\pi(1-\nu)}\frac{b}{\tau_{\text{nuc}}}, \tag{2.9}$$

with $\mu = E/2/(1+\nu)$ the shear modulus. A distribution of point obstacles, which are intended to mimic small precipitates or forest dislocations, is also introduced. Dislocations get pinned at such obstacles and are released once the Peach-Koehler force attains the obstacle strength $b\tau_{\text{obs}}$.

2.2 Results

The objective of the simulations is to gain insight into the thickness-dependent response of thin films. We consider representative values of the material parameters. The Burgers vector of the film material is taken to be $b = 0.25$nm. The linear coefficient of thermal expansion is taken to be representative of silicon for the substrate ($\alpha_{\text{s}} = 4.2 \times 10^{-6}$/K) and of aluminum for the film ($\alpha_{\text{f}} = 23.2 \times 10^{-6}$/K). Results are presented for values of the film thickness, h, ranging from 0.25 to 1μm. In all calculations, the width of the periodic cell is taken to be $w = 2\mu$m. The potentially active slip planes for each slip system are spaced at $d = 100b$, so that there are $n = (w/d)\sin\phi$ slip planes with orientation ϕ inside the cell.

In all the simulations the density of Frank-Read sources randomly distributed on the slip planes is $\rho_{\text{nuc}} = 60/\mu\text{m}^2$. This implies that there are 120 sources per micrometer of film thickness in the cell, which means that not all slip planes are necessarily active. On the other hand, for the thickest films considered, $h = 1\mu$m, there are as many as 4 sources per slip plane. The strength of the sources is

taken randomly from a Gaussian distribution with mean strength $\bar{\tau}_{\text{nuc}} = 25$ MPa and standard deviation of 5 MPa. With the chosen material properties, the mean nucleation distance from (2.9) is $L_{\text{nuc}} = 0.0625\mu$m, which is $1/4$ of the smallest film thickness $h = 0.25\mu$m, and, more importantly, only $1/8$ of the shortest slip plane length $h/\sin 60^\circ$. However, since the strengths are taken from a Gaussian distribution, values of L_{nuc} can deviate significantly from the average. In the distributions used in the calculations here, the smallest value of τ_{nuc} is 10MPa, which corresponds to $L_{\text{nuc}} = 0.156\mu$m. All sources are displaced by at least the distance $L_{\text{nuc}} \sin\phi$ from the top or bottom of the film, in order that both dislocations in a nucleated dipole are contained in the film. Whenever obstacles are considered, their density is taken to be the same as the source density and their strength is specified as $\tau_{\text{obs}} = 150$ MPa.

In order to limit the computational time, the cooling rate is specified as $\dot{T} = 40 \times 10^6 \text{K/s}$ and the total temperature decrease is 200K, which is smaller than usual in experiments. A small time step is required to accurately resolve the dislocation dynamics. Numerical experimentation showed that with the parameters used here, a time step Δt no larger than 0.05ns is needed mainly to capture the formation of dislocation junctions (dipoles) near the intersection of slip planes.

The finite element mesh used to solve for the $\hat{(\,)}$ fields depends on the thickness of the film. In all cases, four-node elements are used which are square in the film and which gradually elongate inside the substrate with increasing depth. For the thinnest films considered, $h = 0.25\mu$m, we have used 10 elements through the film thickness. Numerical tests have shown that this gives sufficient resolution over the top surface to satisfy the stress-free condition with sufficient accuracy.

Each simulation starts with a dislocation-free film, so that when cooling begins, the response is initially elastic. As the temperature decreases, a uniform tensile stress builds up in the film. When the resolved shear stress on a slip system reaches the critical strength of the weakest point source, the source generates a dislocation dipole. One of the dipole dislocations glides in the direction of the free surface and the other glides toward the interface where it gets pinned. It is this movement which provides the mechanism of plastic relaxation of the thermal stress. As cooling proceeds, many other dislocations are nucleated. Because of the stress fields associated with the individual dislocations in the film, the Peach-Koehler force at a source can become large enough to induce a nucleation event, even if the average stress in the film is not high enough to activate the source.

2.2.1 Size effect

We first present results for three cases that differ in the film thickness only: $h = 1\mu$m, 0.5μm and 0.25μm. The film material contains three slip systems, with slip plane orientations: $\phi^{(1)} = 0^\circ$; $\phi^{(2)} = 60^\circ$; $\phi^{(3)} = 120^\circ$. The three slip systems mimic in two dimensions the redundancy of the twelve available slip systems in FCC crystals.

Figure 2.2 shows the distribution of the dislocations and the in-plane stress σ_{11} at the end of the cooling process. The stress is normalized by the elastic stress

$$\sigma_n = -\frac{(\alpha_f - \alpha_s)E\Delta T}{(1-\nu)}, \tag{2.10}$$

which would be present in the film if plastic relaxation had not occurred, see (2.7). With the parameter values here, $\sigma_n = 397$MPa. For each film thickness, a single unit cell of the film as well as the top of the substrate is shown. For the chosen thermal expansion coefficients and with $\Delta T < 0$, the film is in a state of tension, $\sigma_n > 0$. The compressive stress in the substrate is very low on average, because of its large thickness, except in a thin layer directly below the interface which is affected by the dislocations in the film near the interface. Indeed, a relatively large number of dislocations are piled up in the film against the interface because the interface is modeled as being impenetrable. Due to this local high dislocation density, a boundary layer forms with a much higher in-plane stress than in the rest of the film.

A boundary layer is also seen in the dislocation density profiles $\rho(x_2)$ across the film, shown in Fig. 2.3. The dislocation density plotted is the average dislocation density in a strip of height λ, averaged in the x_i-direction. Making use of periodicity, this quantity is computed as

$$\rho(x_2) = \frac{1}{bw\lambda}\sum_I b^{(I)}, \quad \forall I \text{ such that } x_2 - \lambda/2 < x_2^{(I)} < x_2 + \lambda/2. \tag{2.11}$$

Using a strip height of $\lambda = 0.025\mu$m, the profiles in Fig. 2.3 show that there is distinct peak in the bottom strip which is roughly the same for all three thicknesses. The thickness of the highly stressed boundary layer is less than $0.025\mu\text{m} = 100b$. The dislocation density in the rest of the film, where the tensile stress has been relaxed (Fig. 2.2), is at least a factor 4 lower and also appears to be about the same for the three cases.

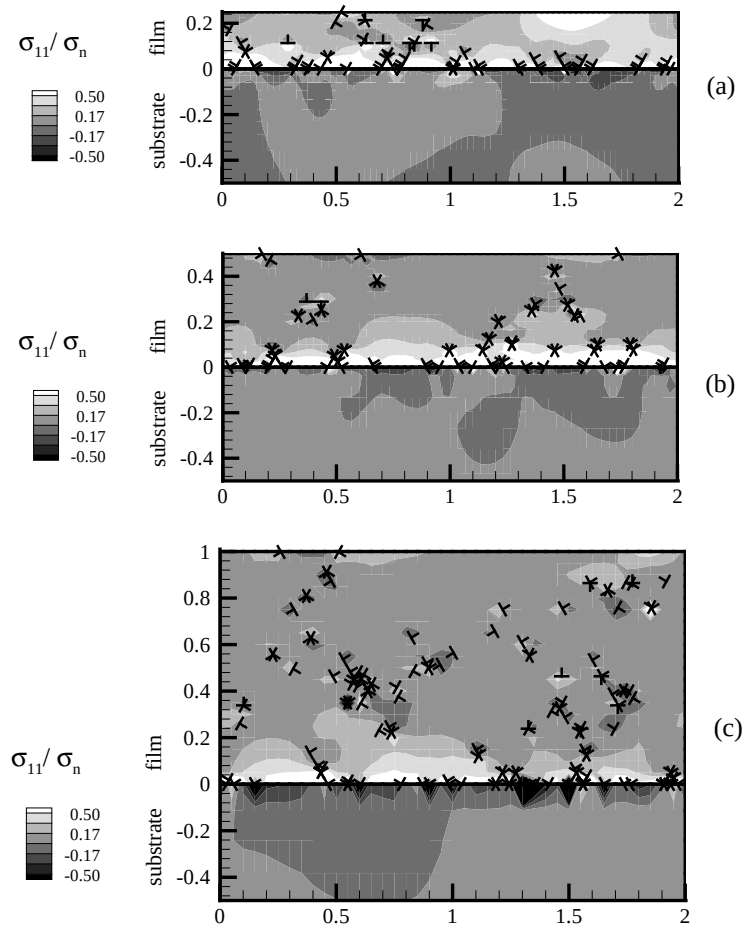

Figure 2.2 Distribution of σ_{11}, normalized by σ_n defined in (2.10), and the dislocation distribution after cooling by 200K for three values of film thickness: (a) $h = 0.25\mu$m, (b) $h = 0.5\mu$m and (c) $h = 1\mu$m. The films have three slip systems with slip plane orientations specified by $\phi^{(1)} = 0^\circ$, $\phi^{(2)} = 60^\circ$, and $\phi^{(3)} = 120^\circ$ (see Fig. 2.1).

Examining the near-interface dislocations shown in Fig. 2.2 reveals that they are either positive dislocations on the $\phi^{(2)} = 60^\circ$ slip planes or negative dislocations on the $\phi^{(3)} = 120^\circ$ slip planes. In both cases the horizontal component of the Burgers vector is in the positive x_1-direction. Neglecting the low density of dislocations in the rest of the film, the classical idealized picture emerges of a film that

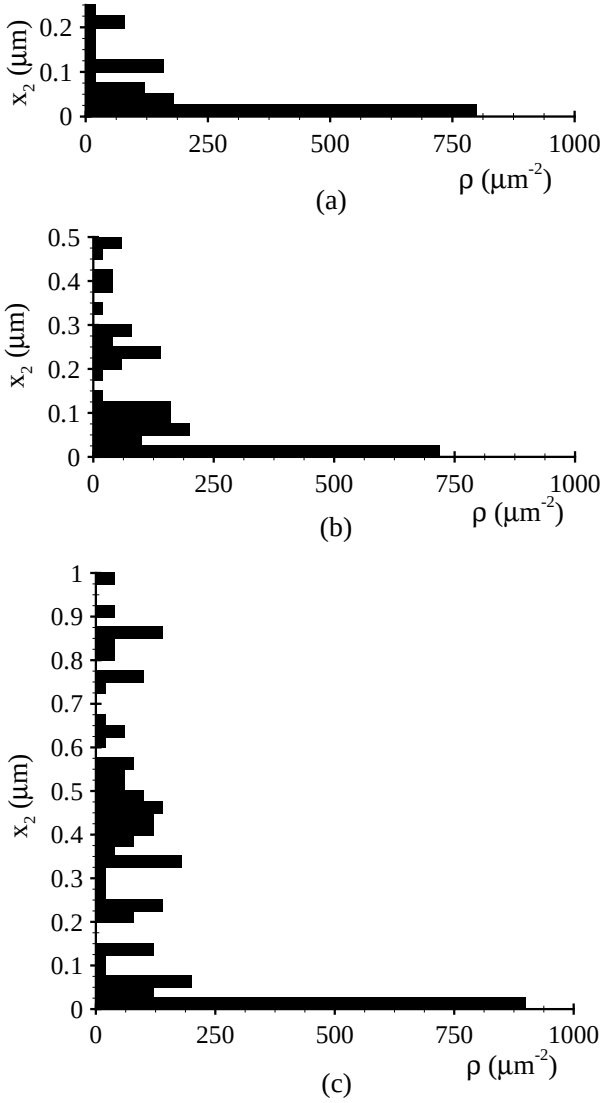

Figure 2.3 Dislocation density profile across the film thickness x_2 for the films in Fig. 2.2. (a) $h = 0.25\mu$m, (b) $h = 0.5\mu$m and (c) $h = 1\mu$m.

is relaxed by a distribution along the interface of misfit dislocations with Burgers vector $b|\cos\phi|$ in the x_1-direction. Full relaxation of the film would require that the thermal strain $(\varepsilon_{11}^{\text{th}})_{\text{f}} = (1+\nu)(\alpha_{\text{f}} - \alpha_{\text{s}})\Delta T$ is entirely accommodated by such

misfit dislocations. The dislocation density in a strip of height λ needed for this is given by

$$\rho = \frac{(1+\nu)(\alpha_f - \alpha_s)\Delta T}{\lambda b \cos\phi}\,. \tag{2.12}$$

For $\lambda = 0.025\mu$m, this expression gives a density $\rho = 1.6\times 10^3 \mu\text{m}^{-2}$. The dislocation density in the bottom strip λ of Fig. 2.3 is around $800\mu\text{m}^{-2}$. This is significantly less than the necessary dislocation density for a completely stress-free film. Thus we expect that there is a significant stress component σ_{11} left in the film.

Figure 2.2 gives insight into the nature of this stress state. An additional perspective is given by the x_1-averaged σ_{11} profiles in Fig. 2.4a for the three film thicknesses considered at $\Delta T = 200$K. The x_1-averaged stresses, $\langle\sigma_{11}\rangle(x_2)$, are computed in a strip-wise fashion as in (2.11), i.e.

$$\langle\sigma_{11}\rangle(x_2) = \frac{1}{w\lambda}\int_{x_2-\lambda/2}^{x_2+\lambda/2}\int_0^w \sigma_{11}(x_1,z_2)dx_1dz_2\,. \tag{2.13}$$

The integral is evaluated using 5×5 trapezoidal quadrature in each strip with height λ of a finite element. A value of $\lambda = 0.0167\mu$m was found to give well-converged results of $\langle\sigma_{11}\rangle(x_2)$. Also shown in Fig. 2.4a are the average stresses in the film: $\langle\sigma_{11}\rangle_f = 50$MPa, 70MPa and 130MPa for $h = 1\mu$m, 0.5μm and 0.25μm, respectively (with $\langle\,\rangle_f$ denoting the film average of a quantity). The profiles clearly show the presence of highly stressed boundary layers and also illustate the variation in boundary layer thickness with film thickness. For the two thickest films, the boundary layer thicknesses are nearly the same, but the boundary layer in the thinnest film is significantly thinner. It is also of importance to note that the stress level in the core of the $h = 0.25\mu$m film is higher than for the other two films. It is primarily this lack of relaxation in the core that causes the $h = 0.25\mu$m film to have the highest average stress.

Average stress, $\langle\sigma_{11}\rangle_f$, versus film thickness h is shown in Fig. 2.4b to illustrate the scaling with film thickness. The thicker two films suggest a Hall-Petch-like $h^{-1/2}$ scaling. The data for the thinnest two films are consistent with the h^{-1} scaling found by Freund [10] and Nix [11] on the basis of energy considerations. Although data from three points is not conclusive, we believe that the dichotomy in scaling is due to a change in hardening mechanism for the thinnest film, as will be discussed in detail in Sec. 2.2.3. We note that the average film stresses are not sensitive to the source distribution; other realizations give results that only differ by a few percent.

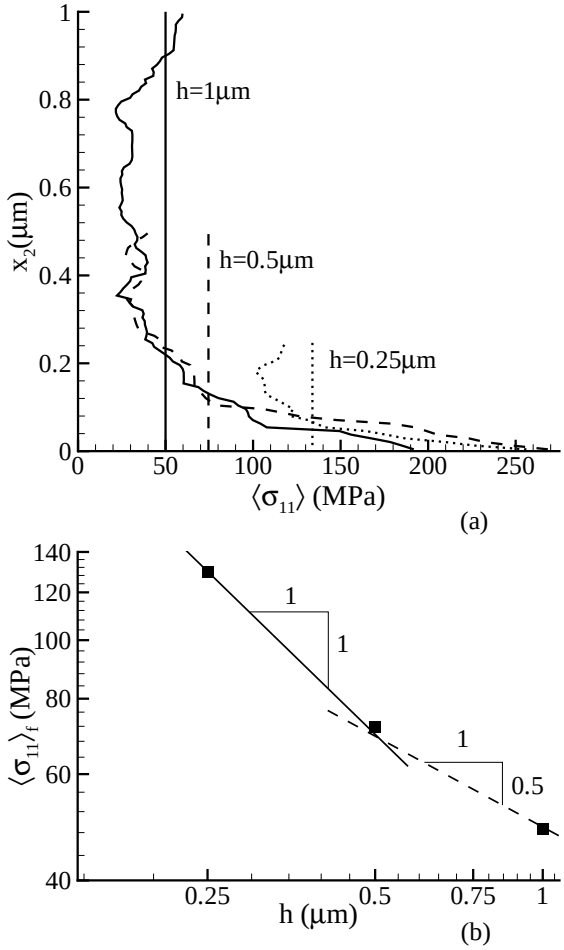

Figure 2.4 (a) Profiles $\langle\sigma_{11}\rangle(x_2)$ of the in-plane stress in the films in Fig. 2.2 averaged in the x_1–direction. The vertical lines show the total film averages, $\langle\sigma_{11}\rangle_{\rm f}$. (b) Average film stress versus film thickness h. The straight lines discribe a power law of the form $\langle\sigma_{11}\rangle_{\rm f} \propto h^{-p}$, giving $p \approx 1$ for the thinnest two films and $p \approx 1/2$ for the thicker ones.

While we have focused until now on the stress states at the end of the cooling process, the full history is shown in Fig. 2.5. Rather than stress, however, Figure 2.5 shows the evolution of $\langle\varepsilon'_{11}\rangle_{\rm f}$ as a function of the temperature reduction. The value of $\langle\varepsilon'_{11}\rangle_{\rm f}$ represents the average lattice strain in the film due to the thermal

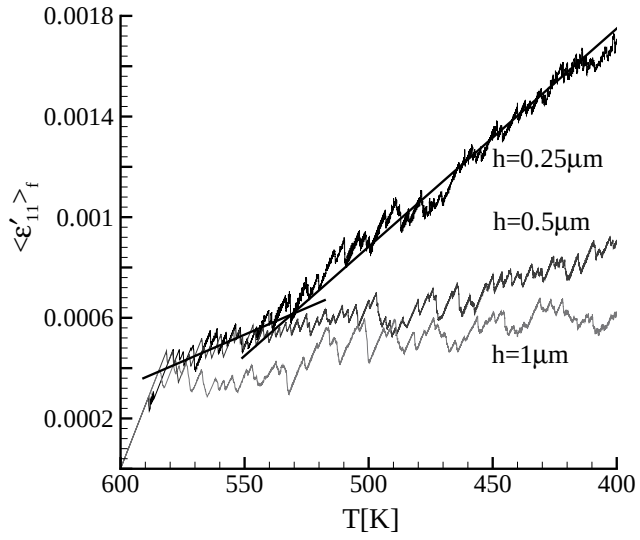

Figure 2.5 Curves of $\langle\varepsilon'_{11}\rangle_{\rm f}$ versus imposed temperature for three values of film thickness: $h = 0.25\mu$m, $h = 0.5\mu$m and $h = 1\mu$m (see Fig. 2.2 and Fig. 2.3).

mismatch with the substrate. Adding $\varepsilon^{\rm th}_{11}$ to it, eq. (2.3), gives the quantity which is usually measured experimentally by X-ray diffraction [3, 21]. From $\langle\varepsilon'_{11}\rangle_{\rm f}$ and the corresponding $\langle\varepsilon'_{22}\rangle_{\rm f}$, the average stress $\langle\sigma'_{11}\rangle_{\rm f}$ can be directly computed from Hooke's law, eq. (2.2), with $\alpha = 0$. Since $\sigma^{\rm th}_{ij} = 0$, eq. (2.3), this immediately gives the total average film stress $\langle\sigma_{11}\rangle_{\rm f}$, cf. (2.4). Thus, plots of the evolution of $\langle\varepsilon'_{11}\rangle_{\rm f}$ give insight into the average stress development in the film.

The curves in Fig. 2.5 exhibit a distinct size effect on the hardening, with thinner films being harder. The yield point, which corresponds to a yield stress of about 30MPa, does not exhibit a size effect, as the initiation of plastic deformation is controlled by the statistical distribution of source strengths. Prior to the first nucleation event, the stress in the film is uniform, so that the first occurrence is determined by the weakest source. Since the source strengths are chosen randomly from a Gaussian distribution around a certain value, and since the specific values of source strength are different for different films, plastic deformation starts first in the film that contains the weakest source. For the cases shown in Fig. 2.5 this happened to be the thinnest film, where the minimum nucleation strength, out of the average of $\bar{\tau}_{\rm nuc} = 25$MPa, is $\tau_{\rm nuc} = 10$MPa.

Hardening, on the other hand, is a collective effect of the nucleation, glide and

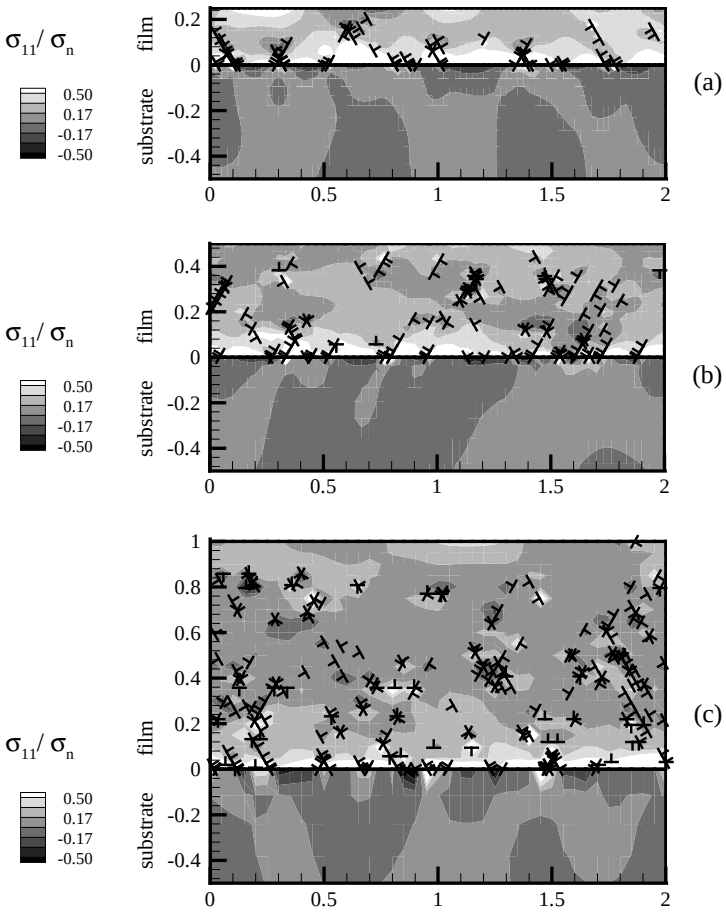

Figure 2.6 Distribution of σ_{11}, normalized by σ_n defined in (2.10), and the dislocation distribution after cooling by 200K for three values of film thickness: (a) $h = 0.25\mu$m, (b) $h = 0.5\mu$m and (c) $h = 1\mu$m with a uniform random distribution of dislocation obstacles. The slip plane orientation is the same as in Fig. 2.2.

annihilation of a large number of dislocations. Statistical effects are therefore smaller. The hardening rate averaged over a temperature drop of $\Delta T = 185$K from the onset of yield, $\Delta\langle\sigma_{11}\rangle_f/\varepsilon_{11}^{th}$ is 18 GPa, 39 GPa and 97 GPa for $h = 1\mu$m, 0.5μm and 0.25μm, respectively. To check the sensitivity of the yield stress and hardening rate to the value of τ_{nuc}, the calculations were repeated with the same source distributions but with the value of τ_{nuc} at each source multiplied by a factor of two. The values of the yield stress for each of the three films doubled, while

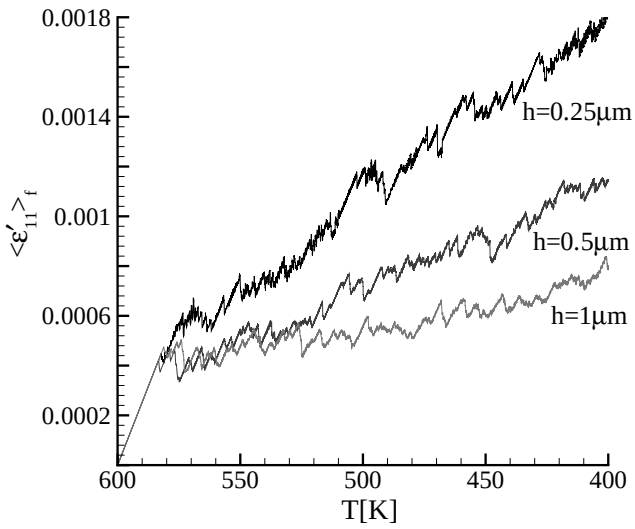

Figure 2.7 Curves of $\langle \varepsilon'_{11} \rangle_f$ versus imposed temperature for three values of film thickness: $h = 0.25\mu$m, $h = 0.5\mu$m and $h = 1\mu$m for the calculation in Fig. 2.6 with a prescribed distribution of dislocation obstacles.

the values of the hardening rate remained essentially unchanged.

Calculations were repeated with all parameters fixed except that a uniform random distribution of point obstacles was added with a density of $60/\mu\text{m}^2$. Figure 2.6 shows that the dislocation density in the core region is higher with obstacles than without obstacles (especially for the thickest film), since the obstacles tend to prevent dislocations from leaving the film at the free surface. In fact, numerous dislocation dipoles form at slip plane intersections, leading to a harder core region than without obstacles which gives rise to the increased hardening rate seen in Fig. 2.7 compared with that in Fig. 2.5.

2.2.2 Effect of slip plane orientation

In order to investigate the influence of slip plane orientation, the simulations presented in the previous section have repeated with the crystal rotated by $\pm 30^\circ$, so that $\phi^{(1)} = 30^\circ$; $\phi^{(2)} = 90^\circ$; $\phi^{(3)} = 150^\circ$ The source density is the same as before, but the source positions and strengths are different; there are no obstacles. Slip systems 2 and 3 are the most active ones, because the resolved shear stress

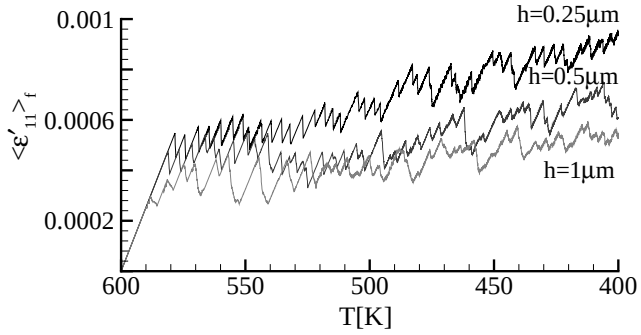

Figure 2.8 Curves of $\langle\varepsilon'_{11}\rangle_f$ versus imposed temperature for three values of film thickness: $h = 0.25\mu$m, h=0.5μm and $h = 1\mu$m. The films contain three slip systems with slip plane orientations $\phi^{(1)} = 30^\circ$, $\phi^{(2)} = 90^\circ$, and $\phi^{(3)} = 150^\circ$.

$\tau = -\sigma_{11}/2\sin 2\phi$, caused by a nominal tensile stress σ_{11}, is largest in absolute value. In fact, the Schmid factor $|\sin 2\phi|$ is the same as for the $\pm 60^\circ$-slip systems in the original orientation. This explains that the onset of yield (Fig. 2.8) is roughly the same as for the original crystal orientation (Fig. 2.5).

The hardening in the film is reduced however, i.e. the stress is more relaxed in the rotated orientation for all film thicknesses, cf. Fig. 2.8 with Fig. 2.5. One explanation for this is that fewer dislocations are needed to relax the film in the rotated orientation: according to (2.12) with $\phi = \phi^{(1)} = 30^\circ$, a dislocation density $\rho = 900\mu\text{m}^{-2}$ is needed in the height $\lambda = 0.025\mu$m for complete relaxation. The dislocation density found near the interface is around $600\mu\text{m}^{-2}$ for all three thicknesses. This is a higher percentage (67%) than for the previous orientation (50%), which is consistent with the film being more relaxed.

The dislocation distribution along with the boundary layer that forms in the thinnest film with orientation $\phi^{(1)} = 30^\circ$ is seen in Fig. 2.9a. Profiles of x_1-averaged stresses for all three thicknesses reveal that the boundary layers have the same thickness, which is slightly smaller than that seen in Fig. 2.4a for the original orientation. A second difference is that the core region of the films is less stressed. The two effects explain the lower hardening in Fig. 2.8.

To investigate the orientation dependence further, simulations were carried out in single slip with slip plane orientations of $\phi = 15^\circ$, 30°, 60° and 75°. In single slip, dislocations do not form junctions, so that the time step can be increased by an order of magnitude without losing accuracy. Figure 2.10 shows that the

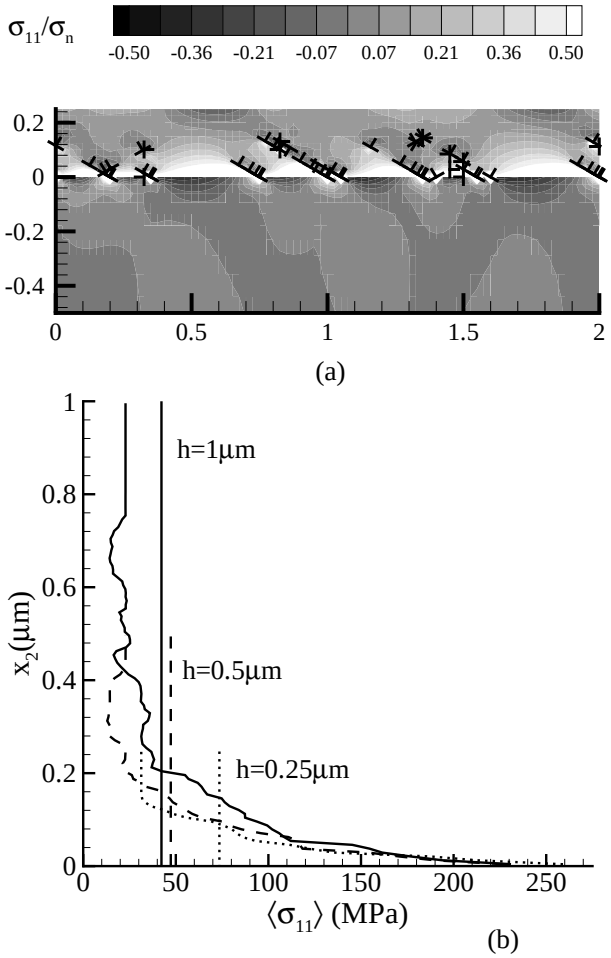

Figure 2.9 Internal stress states for the films in Fig. 2.8 after cooling by 200K. (a) Contours of σ_{11}, normalized by σ_n defined in (2.10), and the dislocation distribution for $h = 0.25\mu$m. (b) Profiles $\langle\sigma_{11}\rangle(x_2)$ of the in-plane stress in all films with this orientation. The vertical lines show the total film averages, $\langle\sigma_{11}\rangle_f$.

hardening rate increases with increasing ϕ. This is mainly due to a combination of the orientation dependence of the Schmid factor and of the slip plane length $h/\sin\phi$. Also, we see that plastic flow occurs earlier for slip plane orientations of 30° and 60° than for those of 15° and 75°, because the resolved shear stress τ is larger for the 30° and 60° orientations.

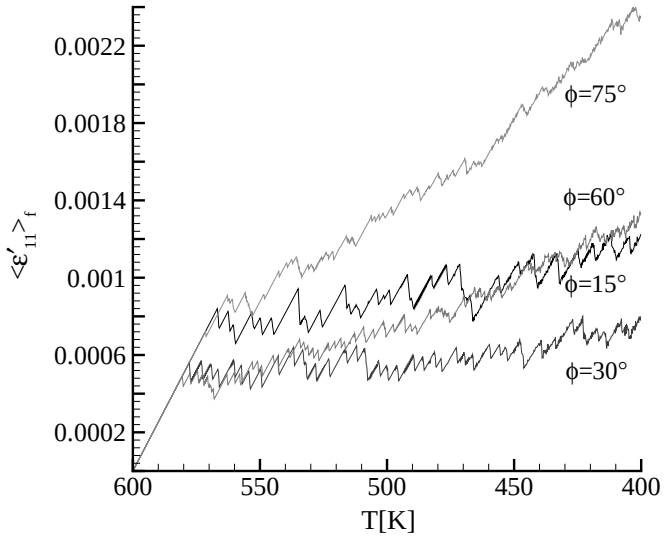

Figure 2.10 Curves of $\langle \varepsilon'_{11} \rangle_{\mathrm{f}}$ versus imposed temperature for films with a single slip system having the slip planes oriented at $\phi^{(1)} = 15^\circ$, $\phi^{(2)} = 30^\circ$. $\phi^{(3)} = 60^\circ$ and $\phi^{(1)} = 75^\circ$. All films have thickness $h = 0.25\mu$m.

2.2.3 Origin of hardening

Examination of the average strain-temperature curves in Figs. 2.5 and 2.8 indicates that there is a more or less pronounced kink in the average slope after the onset of plasticity as exemplified in Fig. 2.5. These kinks reflect a change in the hardening rate in the plastic regime. For the smallest thickness, $h = 0.25$ μm, the kink is most clearly visible; also for the thickest film, $h = 1$ μm, a kink can be observed but occurs at a later stage. Moreover, we observe that the hardening in the second part of the curve increases with the slip plane angle, as seen by comparing Figs. 2.5 and 2.8. A significant increase in hardening has been noted experimentally by Leung et al. [1] in various types of films, and can also be seen in the experimental results in [3]. The strongest effect is always seen, as here, for very thin films. The effect is not found by Leung et al. [1] for passivated films, which has led them to suggest that the effect is due to additional relaxation by surface diffusion at higher temperature. However, the experimental results in [3] also show a two-stage hardening effect for very thin ($h = 0.3\mu$m) passivated films. In our calculations there is no diffusion, and therefore it is interesting to explore

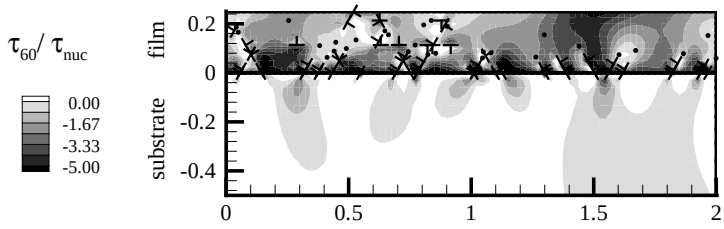

Figure 2.11 Distribution of resolved shear stress on the slip plane $\phi^{(2)} = 60^\circ$, τ_{60} and the dislocation distribution at final temperature for the film in Fig. 2.2a. The point sources on the this slip system are shown as circles.

the origin of the kink in the simulations.

One possible cause is a sudden increase in dislocation density, leading to an increase in the number of dislocation junctions and therefore to an increase in hardening. However, since the kink is present in multiple slip as well as in single slip (no junctions), Fig. 2.10 and Fig. 2.5, this is excluded. Another possible cause is an abrupt reduction of the rate of dislocations nucleated. This is what happens in our calculations, with the reduction in nucleation rate arising from the back stress generated by the dislocations in the boundary layer adjacent to the interface. For each source, nucleation first occurs when the resolved shear stress reaches τ_{nuc}. The stress field of the dipole generated by this source shields the source from further nucleation. The back stress at the source reduces as the dipole spreads, with the least effect occurring when one of the dislocations has left the film through the free surface and the other is blocked near the interface. In very thin films the back stress in this configuration is still high enough to have a significant effect at the source. During the first stage of the cooling process, other sources in the film will be activated before the back stress at previously activated sources has been overcome by the applied stress. This gives rise to the initial hardening rate. At some stage of the deformation history, all sources have been activated and collectively they have produced back stress throughout the film. Subsequently, the only way in which sources can be activated is by overcoming the back stress through further straining of the film. Thus, nucleation is delayed, which gives rise to additional hardening in the $\langle \varepsilon'_{11} \rangle_{\text{f}}$–$\Delta T$ curves.

To support this explanation, Fig. 2.11 shows the distribution of the resolved shear stress τ for the film with $h = 0.25\mu$m on slip system $\phi^{(2)} = 60^\circ$ at the same time as in Fig. 2.2a. Also shown are all sources that are present on these slip

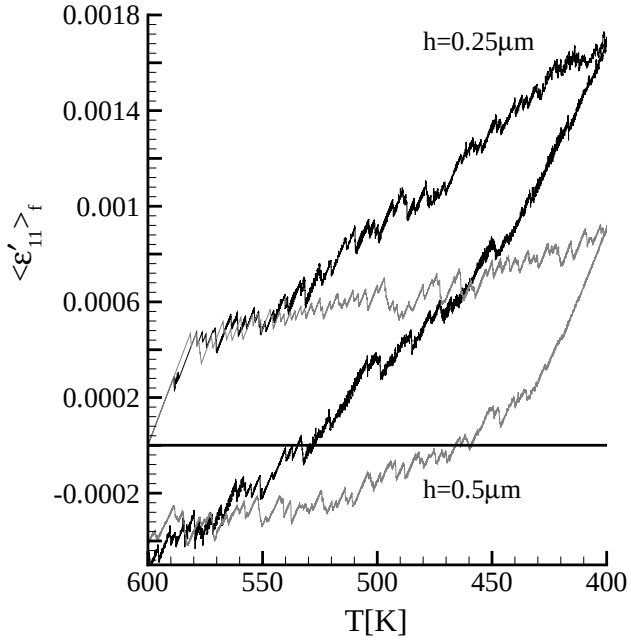

Figure 2.12 Curves of $\langle \varepsilon'_{11} \rangle_{\mathrm{f}}$ versus imposed temperature for a thermal cycle between 600K and 400K for films of thickness $h = 0.25\mu$m and $h = 0.5\mu$m.

planes to demonstrate that they are all in regions with relatively low stress due to the back stresses caused by the dislocations piled up against the interface. As the thickness of the film increases, the back stress at a source caused by the dislocation pile-ups at the film-substrate interface will, on average, be lower because of the larger distance between the pile-up and the source. Hence, for thicker films, the kink in hardening is delayed and is less intense. This is confirmed by the results in Figs. 2.5 and 2.8.

The presence of the back stress is expected to give an important contribution to the response when the temperature change is reversed. This is verified for the thinnest film, by re-heating from the final temperature of $T = 400$K reached previously. As seen in Fig. 2.12, reverse plasticity occurs almost immediately after temperature reversal for $h = 0.25$ μm. Without the presence of the long-range back stresses, elastic unloading would occur over a larger interval.

It should also be noted that the resolved shear stress distribution in Fig. 2.11 does not exhibit the same clear boundary layer as does the distribution of σ_{11} in

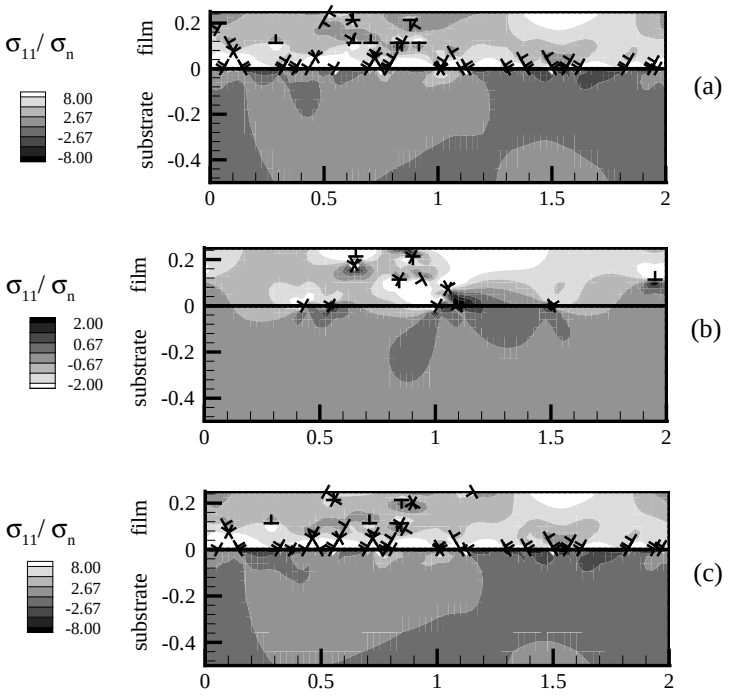

Figure 2.13 Dislocation distribution and in-plane stress, normalised by the elastic stress σ_n, in the film with thickness $h = 0.25\mu$m: (a) at 400K after the first cooling, (b) at 600K after heating and (c) at 400K after the second cooling.

Fig. 2.2a. This suggests a limitation to the classical picture of misfit dislocations with Burgers vector parallel to the interface. The piled-up dislocations on the inclined slip planes do not neatly combine to such misfit dislocations: on average they do, but not point-wise along the interface. In fact, closer examination of the dislocation structure shown in Fig. 2.5a shows the presence of pile-ups of two or three dislocations on the same slip plane. As there are no dislocations on a nearby inclined slip plane to cancel the resulting long-range back stress, the back stress remains effective for blocking nucleation on the same slip plane.

2.3 Thermal cycling

In this section are presented results of simulations in which the two thinnest films are at first cooled down from 600K to 400K, successively heated up to 600K and at last cooled again down to 400K.

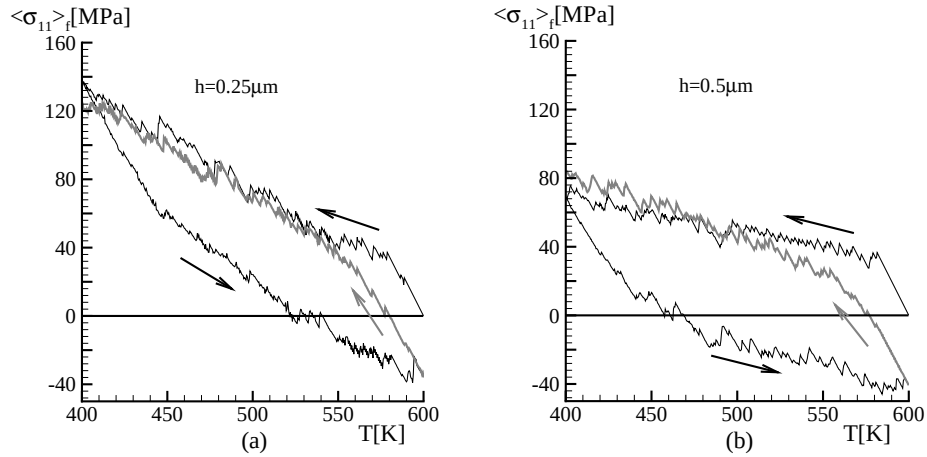

Figure 2.14 Average in-plane stress in the film versus imposed temperature for film thicknesses: (a) $h = 0.25\mu$m and (b) $h = 0.5\mu$m.

The dislocation distribution for the 0.25μm film at the end of the first cooling stage ($T = 400$K) is shown in Fig. 2.13a, together with the distribution of σ_{11}, the normal stress parallel to the interface. If the temperature is kept constant at 400K, no significant evolution of the dislocation structure is observed, indicating that the dislocation structure is close to equilibrium.

During heating, when the film straining changes sign, the direction of dislocation motion is reversed. The high back stress built up during cooling acts to enhance dislocation motion, so that reverse plastic deformation occurs. The dislocations that were forming pile-ups at the interface progressively reach the free surface and leave the film. At the end of the heating process (see Fig. 2.13b) only a few dislocations are left in the film. A few of those dislocations have signs opposite to the signs of the dislocations nucleated during cooling; the opposite-signed dislocations were nucleated during heating when the mean stress state became sufficiently compressive. The average σ_{11} stress (in absolute value) reached after heating is much lower than that after cooling (note that the stress range in Fig. 2.13b is smaller than in Figs. 2.13a and 2.13c) but is not zero as it is prior to the first cooling. Thus, the response is not reversible, as is indeed seen in experiments. After the second cooling (Fig. 2.13c) the stress state in the film is very similar to the one obtained after the first cooling, with small differences in the dislocation structure.

The evolution of the average in-plane stress in the two films during the imposed thermal history is shown in Fig. 2.14. Comparison between Fig. 2.14a and b for

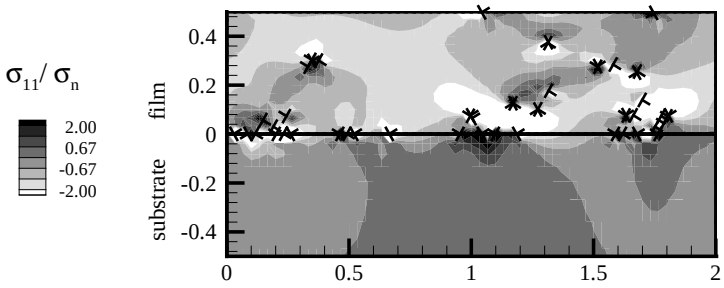

Figure 2.15 Dislocation distribution and in-plane stress normalised by the elastic stress σ_n in the film with thickness $h = 0.5\mu$m after cooling to 400K and re-heating to 600K.

$h = 0.25\mu$m and 0.5μm gives evidence of a quite pronounced size effect. During the first cooling cycle, the 0.25μm film hardens much more than the film with $h = 0.5\mu$m, as discussed in more detail in the previous section. In the 0.25μm film, the high stress level pushes the dislocations in the pile-ups close together. This results in large back stresses which cause reverse plasticity in the early stages of the subsequent heating process.

In the $h = 0.5\mu$m film the back stress associated with the pile-ups is lower. As a consequence, this thicker film unloads elastically almost until the stress changes sign. A compressive stress builds up in the film at around 430K, leading to the dislocation distribution at 600K shown in Fig. 2.15. The dislocation density after unloading is greater in the 0.5μm film than in the 0.25μm film. (Fig. 2.15 versus Fig. 2.13b).

The dislocation structure at 600K strongly influences the material response during the last cooling sequence. The dislocation density in the thin $h = 0.25\mu$m film is very low, Fig. 2.13b, and most of the dislocations have been generated during the first cooling cycle. This situation is very similar to the initial condition, when the film was dislocation free. Therefore the response of the 0.25μm film during first and second cooling differs only in the initial stages (until 550K), see Fig. 2.14a.

During re-cooling of the 0.5μm film, Fig. 2.14b, the dislocations that were nucleated during heating are already available to move and relax the stress, giving rise to a difference in initial plasticity compared to the first cooling. Subsequently, around 500K, relaxation becomes mainly nucleation controlled, and the stress level reaches and overtakes the level in the first cooling.

2.4 Conclusions

Discrete dislocation analyses have been carried out of the stress evolution in single crystal films arising from the thermal mismatch between the film and its substrate. Attention was confined to plane strain, with the substrate remaining elastic and any effect of elastic mismatch between the film and substrate neglected. The film is initially dislocation free and the dislocations in the film, which are all of edge character, nucleate from Frank-Read sources on a specified set of slip planes. At the start of a calculation, the film-substrate system is stress free and the deformation arises from a prescribed temperature history. The results exhibit the follow trends:

- The stress evolution and the hardening show a clear dependence on film thickness for the thicknesses analyzed which range from 0.25 μm to 1 μm.
- The effect of film thickness is mainly due to the formation of a hard boundary layer at the film-substrate interface. The width of the boundary layer, which arises from dislocation pile-ups at the interface, does not scale with the film thickness.
- The boundary layer width depends on the orientation of the slip systems in the film.
- Below a certain film thickness, an additional contribution to hardening arises from a reduction in dislocation nucleation caused by the back stress associated with the dislocation pile-ups at the film-substrate interface. This reduction in the rate of dislocation nucleation can occur abruptly and lead to a two-stage hardening behavior as seen experimentally.
- In very thin films all the available dislocation sources are affected by the back stress early in the stress relaxation process. Further nucleation is suppressed until the back stress at the sources is overcome by additional straining of the film. The absence of dislocations that can eliminate the long-range back stress is related to the limited availability of sources.

Thermal cycling of the two thinnest film between 600K and 400K shows that:

- For both values of the film thickness, the high long-range back stress accumulated inside the films during the first cooling process induces early reversed plasticity during subsequent heating.

- When heating starts, de-stressing is elastic over a range that is almost equal to two times the initial elastic range, with an average yield stress of 40MPa in both films, predicting that hardening in thin films is essentially of kinematic character.
- Plastic relaxation during heating takes place mainly by the movement of dislocations already present in the films. In the 0.5μm film, there is a small contribution to relaxation by nucleation of new dipoles at the end of the cooling process, when the mean stress becomes sufficiently compressive to activate the sources.
- Upon re-cooling, the dislocation density in the 0.25μm film is so low, that the plastic behavior during the first and second cooling cycles are very similar. However, the dislocations nucleated during heating in the thicker $h = 0.5\mu$m film influence the hardening of that film during the second cooling.

References

[1] O.S. Leung, A. Munkholm, S. Brennan, W.D. Nix, J. Appl. Phys. **88** (2000) 1389.

[2] R. Venkatraman and J.C. Bravman, J. Mater. Res. **7** (1992) 2040.

[3] S.P. Baker, A. Kretschmann, E. Arzt, Acta Mater. **49** (2001) 2145.

[4] M. Hommel, O. Kraft, Acta Mater. **49** (2001) 3935.

[5] N.A. Fleck and J.W. Hutchinson, Adv. Appl. Mech. **33** (1997) 295.

[6] N.A. Fleck and J.W. Hutchinson, J. Mech. Phys. Solids **49** (2001) 2245.

[7] M. E. Gurtin, J. Mech. Phys. Solids **50** (2002) 5.

[8] H. Gao, Y. Huang, W.D. Nix and J.W. Hutchinson, J. Mech. Phys. Solids **47** (1999) 1239.

[9] E.C. Aifantis, J. Engin. Mater. Technol. **106** (1984) 326.

[10] L.B. Freund, J. Appl. Mech. **43** (1987) 553.

[11] W.D. Nix, Scripta Mater. **39** (1998) 545.

[12] W.D. Nix and O.S. Leung, Thin Films: Plasticity, Encyclopedia of Materials: Science and Technology (2001) 9262.

[13] P. Chaudhari, Phil. Mag. **A39** (1979) 507.

[14] C.V. Thompson, J. Mater. Res. **8** (1993) 237.

[15] A. Hartmaier, M.C. Fivel, G.R. Canova, and P. Gumbsch, MRS Proceedings **505** (2001) 539.

[16] M.L. Ovecoglu, D.M. Barnett, W.D. Nix, Acta Metall. **7** (1987) 1779.

[17] E. Van der Giessen, A. Needleman, Simul. Mater. Sci. Eng. **3** (1995) 689.

[18] J.Y. Shu, N.A. Fleck, E. Van der Giessen, A. Needleman, J. Mech. Phys. Solids **49** (2001) 1361.

[19] A.N. Gulluoglu, D.J. Srolovitz, R. LeSar, P.S. Lomdahl, Scripta Metall. **23** (1989) 1347.

[20] L.P. Kubin, G. Canova, M. Condat, B. Devincre, V. Pontikis and Y. Bréchet, Solid State Phenomena **455** 1992 23.

[21] A. Saerens, P. Van Houtte, B. Meert and C. Quaeyhaegens, J. Appl. Cryst. **33** 2000 312.

[22] R.J. Asaro, Adv. Appl. Mech. **23** (1983) 1.

Chapter 3

Two hardening mechanisms in single crystal thin films *

Even though it is widely accepted that thin film hardening is thickness dependent (see, e.g., [1]), a universal scaling law to describe the phenomenon has not yet been found. Many authors propose to use a Hall-Petch relation, of the type used for bulk materials, where the grain size d is replaced by the film thickness h. The exponent of h, however, is still unknown. What has been often proposed is that the film strength scales inversely with the film thickness ([2, 3, 4]), but experiments are not decisive. Beside the practical difficulty of performing experiments on very thin films, available experimental results have the drawback that it is hard to distinguish between the contribution of grain size and of film thickness on hardening.

As shown in the previous chapter, discrete dislocation simulations on single crystal thin films are able to capture a size-dependent response in films thinner than roughly one micrometer. There, we have mainly attributed the size effect to the presence of a hard boundary layer of non-scaling thickness at the film-substrate interface, caused by dislocation pile-ups. However, a Hall-Petch like scaling law with a coefficient common to the three films considered was not found, suggesting that a constant boundary layer is not the only cause of the size effect. The high stress found in the thinnest film analyzed in chapter 2, $h = 0.25\mu$m, was explained by a different origin of hardening in such thin films.

In this chapter, attention is focused on films with thickness ranging from 2 to 0.125 μm. In particular we study the difference in hardening of thin versus very thin films as found in dislocation dynamics simulations, through a straightforward analysis of how the dislocation structure is related to the film stress state. Simulations show that there is a material-dependent threshold thickness below which the size effect is completely determined by the capability of Frank-Read sources

*Based on *Two hardening mechanisms in single crystal thin films studied by discrete dislocation plasticity*, L. Nicola, E. Van der Giessen, A. Needleman, Philos. Mag., to appear.

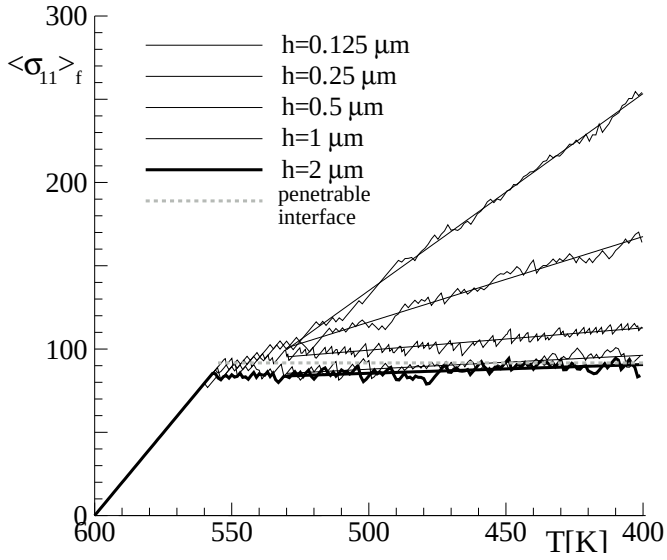

Figure 3.1 Average stress in the film, $\langle\sigma_{11}\rangle_{\mathrm{f}}$, versus temperature T for films of various thickness.

to operate in a constrained geometry. Only above this threshold thickness, is the size effect due to the non-scaling size of the boundary layer.

3.1 Observations from simulations

Results are presented for five films of thickness $h = 2$, 1, 0.5, 0.25 and 0.125μm. Formulation of the problem and method of analysis are the same used in the previous chapter. The simulation parameters are also unchanged, with exception of the average nucleation strength τ_{nuc} and standard deviation τ_{ave}, which are here taken to be 50 and 10MPa, respectively (they were 25 and 5MPa in chap. 2). A larger nucleation strength gives a shorter nucleation length L_{nuc}, which is more appropriate in the study of a film as thin as 0.125μm, since L_{nuc} should be completely contained in the film.

The major part of the discussion will be for a crystal with slip plane orientation $\phi^{(60)} = (0^\circ, 60^\circ, 120^\circ)$ but we will also consider slip planes with orientation $\phi^{(30)} = (30^\circ, 90^\circ, 150^\circ)$.

The curves in Fig. 3.1 show the evolution of the average in-plane stress, $\langle\sigma_{11}\rangle_f$, during cooling in the different films, for which the interface with the substrate is

impenetrable for the dislocations. Plastic relaxation by dislocation motion is quite effective in all films until a temperature of around 530K is reached: there is a size effect, but it is not as pronounced as during the rest of the cooling. For $T < 530$K the thinnest two films harden linearly with a larger slope and the size effect becomes more evident. The change in slope corresponds to the formation of dislocation pile-ups at the film-substrate interface, which influence relaxation through their back stress on the sources, as discussed in some detail in chapter 2. Between $T \approx 530$K and the final temperature, $T = 400$K, the curves have been fitted to straight lines according to a standard least-squares algorithm.

The gray line in Fig. 3.1 fits the average stress-temperature curve for a film with $h = 0.5\mu$m which has a completely absorbing interface with the substrate. In this case, dislocations can pass through the interface where they are absorbed into the substrate, leaving displacement steps accommodated by the substrate. Also in this case, yield occurs when the weakest source in the film nucleates, but after yield, plastic flow continues at the yield stress. After nucleation, dislocation pairs glide the slip planes until one dislocation leaves the film from the free surface and the other enters the absorbing interface. Dislocations do not accumulate in the film as in the case of films with impenetrable interface, and therefore there is no back stress, no hardening and no size effect.

Figure 3.2 shows how the stress σ_{11} averaged along the x_1 direction varies over the film height. $\langle\sigma_{11}\rangle$ is uniform in the film with a perfectly absorbing interface with the substrate. All other films exhibit a hard layer in proximity of the film-substrate interface and an almost homogeneous stress state in the rest of the film. The hard layer is characterized by a high stress gradient towards the interface.

The line indicating the stress profile in the film with an absorbing interface intersects the curves for the three thicker films. We take this intersection as the separation point between the hard boundary layer and the zone of homogeneous stress in these films. In the following we will refer to the zone of homogeneous stress between boundary layer and free surface as bulk. For the two thinner films, we define the bulk as the zone at constant stress close to the free surface, the boundary layer the zone close to the interface were there is a stress gradient. While the three thicker films have approximately the same value of stress in the bulk ($\langle\sigma_{11}\rangle_b \simeq 80$MPa), the bulk of the two thinner films is much harder ($\langle\sigma_{11}\rangle_b = 145$MPa for the film with $h = 0.25\mu$m and $\langle\sigma_{11}\rangle_b = 245$MPa for the film with $h = 0.125\mu$m). The size of the boundary layer is approximately the same in the two thicker films ($h_l = 0.25\mu$m), but is smaller in the two thinner ones (approximately

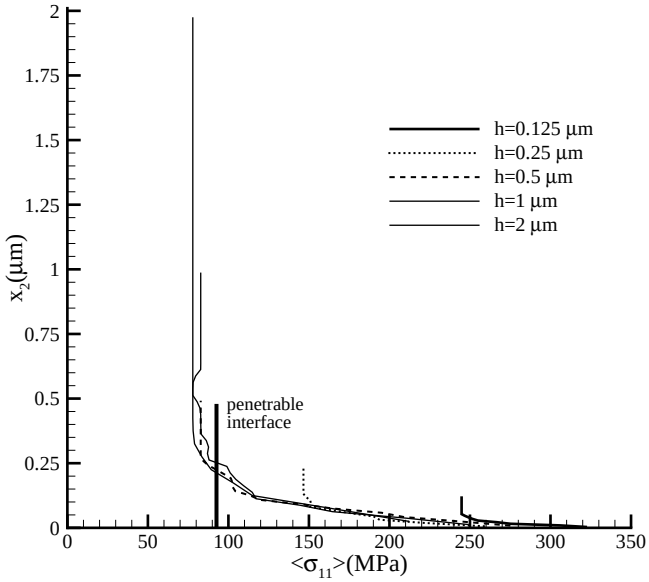

Figure 3.2 Distribution of the average in-plane stress $\langle\sigma_{11}\rangle$ over the film height x_2 in films with an impenetrable interface. The result for a $h = 0.5\mu$m film with an absorbing interface is shown for comparison.

$h_l = 0.1\mu$m for $h = 0.25\mu$m and $h_l = 0.05\mu$m when $h = 0.125\mu$m). The thinnest film considered is actually thinner than the boundary layer in the thicker films.

Figure 3.3 shows the stress state reached at final temperature and the corresponding dislocation distribution for the films with $h = 0.5$ and $h = 0.125\mu$m. Black dots indicate the positions of Frank-Read sources (recall that their density is independent of h). The stress is normalized by the elastic stress

$$\sigma_n = E/(1-\nu^2)\varepsilon_{th} = -\Delta\alpha E\Delta T/(1-\nu)$$

which for $\Delta T = -200K$ is $\sigma_n = 397$MPa. For a given range of contour levels, a comparison can be made between the stress state in the two films. Two differently stressed regions can be recognized in the thicker film. But, a measure of the size and intensity of the boundary layer cannot be obtained from these contour plots since the size of the white region in the thicker film depends on the contour levels and range.

The analysis of the dislocation structure at final temperature can give a better understanding of the stress profiles in Fig. 3.2. What is common to the two films

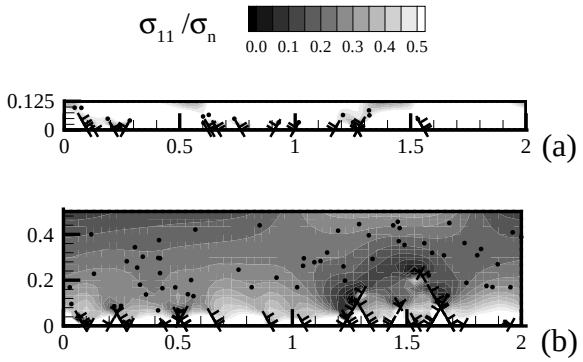

Figure 3.3 Distribution of dislocations ($\perp$) and sources ($\bullet$) in films of thickness (a) $h = 0.125\mu$m and (b) $h = 0.5\mu$m at final temperature, superimposed on contours of constant σ_{11}.

in fig 3.3 is that dislocations have piled up against the film-substrate interface and that only the slip planes at 60° and 120° have been active. The main differences between the dislocation structures of the two films are the dislocation density, the density of dislocation pile-ups and their length. These quantities are listed for the five films considered in Table 3.1, together with the average stress in the films and the stress computed in the film bulk. One notes first that the density of dislocations for the film with $h = 1\mu$m is two times larger than in the film with $h = 2\mu$m; the same holds for the films with $h = 0.5$ and 1μm but for the two thinner films the dislocation density does not scale any more with the film thickness. This means that in the thinner films a smaller number of dislocation pairs has been available to relax the stress during thermal history, explaining the higher average stress in these films (see also [5]). A reduced nucleation activity in very thin films is caused by the proximity of sources to the film-substrate interface: the length of dislocation pile-ups is then limited by the distance between the point source and the interface. The longest pile-up in the film of thickness $h = 1\mu$m is 0.25μm long. Such a long pile-up can surely not form in a film with $h = 0.125\mu$m. In addition to that, sources that are very close to the interface and thus to the dislocation pile-ups, are affected by the back stress associated to the pile-ups, which delays the nucleation events [5]. The back stress affecting a source close to the interface is mainly caused by the pile-up generated by the nucleation source itself. In the subsequent sections we will analyze more in detail how the dislocation structure at final temperature is related to the stress state in the film.

$h(\mu\text{m})$	0.125	0.25	0.5	1	2
average stress $\langle\sigma_{11}\rangle$ (MPa)	253	167	113	96	90
bulk stress $\langle\sigma_{11}\rangle_b$ (MPa)	245	147	82	82	78
dislocation density (μm^{-2})	124	102	64	33	16.5
pile-up density (μm^{-2})	56	40	18	8	4.5
max pile-up length (μm)	0.045	0.115	0.221	0.250	0.312
boundary layer thickness (μm)	0.05	0.13	0.250	0.245	0.245
σ_b (MPa) from (3.4)	246	150	86	87	77
σ_{int} (MPa) from(3.6)	330	300	310	319	310

Table 3.1 Characteristics in films with slip planes at $(0^\circ, 60^\circ, 120^\circ)$ at various values of the film thickness.

3.2 Characterization of stress state

3.2.1 Stress state in the film bulk

As shown in Fig. 3.2, the stress at final temperature in the bulk of all films is homogeneous and lower than the elastic stress, $\sigma_n = 397$MPa. The stress in the bulk has been relaxed by dislocation pairs that have glided during thermal history. One dislocation out of each pair has left the film through the free surface but the other is still in the film, piled up against the interface. The density of dislocations that have contributed to the relaxation of the film is therefore known from the final dislocation density.

Stress relaxation is mainly given by dislocation glide on the slip planes with $\phi = 60^\circ$ and $\phi = 120^\circ$. Dislocation activity on the slip planes parallel to the interface is very limited, since their Schmid factor is zero. Figure 3.4(a) gives a schematic representation of the relaxation process: opposite signed dislocations move on the slip planes, one towards the free surface, the other towards the interface with the substrate. The dislocations in Fig. 3.4(a) can be approximated by two parallel arrays of dislocations, each having Burgers vector of length $b\cos\phi$ but pointing in x_1 or $-x_1$ direction, respectively.

The stress field of a single array of dislocations in infinite space (see Fig. 3.5)

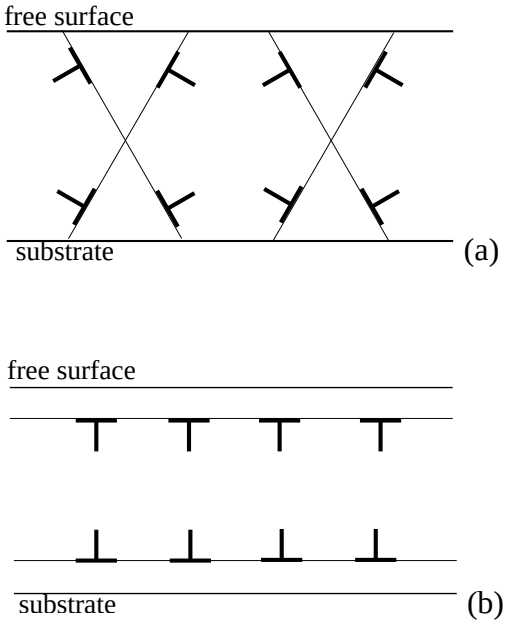

Figure 3.4 (a) Schematic representation of dislocations gliding on slip planes $\phi = 60^\circ$ and $\phi = 120^\circ$. (b) Dislocation structure equivalent to the one in figure (a), obtained by composing the dislocation Burgers vectors. The Burgers vector of each dislocation in the array is $b\cos\phi$.

can be calculated analytically (see for the complete derivation [6]):

$$\sigma_{11} = \frac{Eb}{4d(1-\nu^2)} \frac{1}{\cosh 2\pi\eta - \cos 2\pi\xi} \left[2\sinh 2\pi\eta + 2\pi\eta \frac{1-\cos 2\pi\xi \cosh 2\pi\eta}{\cosh 2\pi\eta - \cos 2\pi\xi} \right], \tag{3.1}$$

where d is the spacing between dislocations, and $\xi = X/d$ and $\eta = Y/d$ are local coordinates of the point were σ_{11} is calculated (see Fig. 3.5). This stress, averaged over ξ for any value of $\eta > 0$, is

$$\langle \sigma_{11} \rangle_\xi (\eta) = -\frac{Eb\cos\phi}{2d(1-\nu^2)}. \tag{3.2}$$

The effect of the array near the free surface is the same, so that the average stress between the two arrays of dislocations in Fig. 3.4b is given by

$$\sigma_d = -\frac{Eb\cos\phi}{d(1-\nu^2)}. \tag{3.3}$$

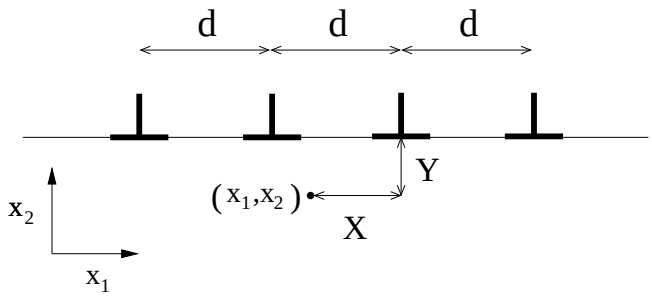

Figure 3.5 Infinite array of edge dislocations spaced by d.

On average, the effects of the two arrays outside the band cancel. If the dislocation arrays are moving in a film, the stress state in the part of the film already glided is $\sigma_n + \sigma_d$, in the rest of the film it is just the elastic stress. The relaxation process is complete when one of the arrays reaches the interface and the other one the free surface. The average stress state then is $\sigma_n + \sigma_d$ everywhere in the film, i.e.

$$\sigma_b = \sigma_n - \frac{E b \cos\phi}{d(1-\nu^2)} = \sigma_n - \frac{\rho h E b \cos\phi}{(1-\nu^2)} \tag{3.4}$$

where ρ is the density of dislocations in the film.

The same result can be obtained by considering each dislocation at the interface as an inserted atomic half plane of Burgers vector $b\cos\phi$. The plastic strain caused by an array of such half planes at a spacing d is $\varepsilon_p = b\cos\phi/d$. This strain partly accommodates the applied thermal strain ε_{th}. From this argument the bulk stress can be expressed as

$$\sigma_b = \frac{E}{(1-\nu^2)}\left[\varepsilon_{th} - \varepsilon_p\right] = \frac{E}{(1-\nu^2)}\left[(1+\nu)\Delta\alpha\Delta T - \frac{b\cos\phi}{d}\right] \tag{3.5}$$

which is identical to eq. (3.4).

Comparison between the values of σ_b obtained from eq. (3.4) and $\langle\sigma_{11}\rangle_b$ computed during the simulation shows very good agreement. We conclude that the density of dislocations in the quantity ρh together with the orientation of the Burgers vectors is sufficient to determine the average stress state in the film bulk. It is to be noticed that the value of ρh is $32\mu\text{m}^{-1}$ for the thicker films and only $26\mu\text{m}^{-1}$ and $16\mu\text{m}^{-1}$ for the two thinnest ones in Table 3.1. As mentioned before, dislocations nucleated in the thinner films are not sufficient to relax the film bulk as much as in the thicker films.

3.2.2 Stress state in the boundary layer

As previously mentioned we call boundary layer the part of the film close to the interface, were the stress is larger than the stress in the bulk. By comparing Fig. 3.2 and Fig. 3.3 one can see that the size of this boundary layer is determined by the length of dislocation pile-ups, see also Table 3.1. The $\langle\sigma_{11}\rangle(x_2)$ stress is maximum at the interface, where the first dislocations of the pile-ups are located. At the interface, only the effect of those dislocations is present. The dislocation array formed by the first dislocations of all pile-ups produces a stress state which can again be described by equation (3.3). The stress at the interface can be calculated as:

$$\sigma_{int} = \sigma_n - \frac{\rho_p h E b \cos\phi}{(1-\nu^2)} \tag{3.6}$$

where ρ_p is the density of leading pile-up dislocations at the interface, independently of pile-up length (when present, also single dislocations at the interface).

The values calculated using equation (3.6) (listed in Table 3.1) are somewhat larger than the values one can read from the plot in Fig. 3.2. This is due to the fact that measure in the plot is not very accurate, the stress is not calculated exactly at the interface, but through integration points close to the interface. In this way part of the effect of the second dislocations in the pile-ups is also taken into account. The stress rapidly decreases with the distance from the interface until it reaches the bulk stress. The stress gradient is not constant in the boundary layer, but becomes smaller in proximity to the bulk, were only the last dislocations of a few long pile ups contribute to it. The pile-ups are shorter in the thinner films than in the thicker ones, therefore the boundary layer in very thin films is thinner.

3.2.3 Validity of the Hall–Petch relation

Let us first consider the thicker films, $h \geq 0.5\mu$m. If we assume a hardening law of the type

$$\sigma = \sigma_0 + k h^{-n}, \tag{3.7}$$

we can take $\sigma_0 = \sigma_b \cong 80$ MPa, since the thicker films have a similar stress state in the bulk. We first obtain the coefficient k by substituting in (3.7) the values of $\langle\sigma\rangle$ and $\langle\sigma\rangle_b$ for the film with $h = 1\mu$m at final temperature. For this film thickness, knowledge of n is not needed and we find $k = 16\text{MPa}\mu\text{m}^n$. With this value of k, substitution of the values of $\langle\sigma_{11}\rangle$ for σ and $\langle\sigma_{11}\rangle_b$ for σ_b for the film with $h = 0.5\mu$m, yields that the exponent of h must be $n = 1$. As a check we can use

the film of thickness $h = 2\mu$m: substitution of the obtained values into (3.7) leads to $\sigma = 88$MPa which is very close to the value of $\langle\sigma_{11}\rangle = 90$MPa obtained from the simulation, see Table 3.1.

The average stress in the film can be more specifically seen as the weighted sum of the stress in the film bulk and the average stress in the boundary layer, i.e.

$$\sigma = \sigma_b \frac{1-h_l}{h} + \sigma_l \frac{h_l}{h}, \tag{3.8}$$

where σ_l and h_l indicate the boundary layer average stress and thickness, respectively. Equation (3.8) can be rewritten to have the form of equation (3.7) as

$$\sigma = \sigma_b + (\sigma_l - \sigma_b)h_l/h, \tag{3.9}$$

so that $k = (\sigma_l - \sigma_b)h_l$ and $n = 1$.

The equation (3.9) holds for films of any thickness. For the three thicker films, k and $\langle\sigma\rangle_b$ can be considered material parameters, since these films have a similar bulk stress and a similar boundary layer stress and thickness. For the thinner films, however, k and $\langle\sigma\rangle_b$ depend on the film thickness: stress in the bulk and in the boundary layer increase with increasing film thickness, while the size of the boundary layer decreases. In effect it means that the Hall-Petch is no longer relevant.

It is not possible to find a precise film thickness, above which the films will behave according to equation (3.7) with a constant k and σ_b. All parameters which affect the dislocation density in the films, such as the density or strength of nucleation sources or the presence of obstacles, determine at which film thickness k and σ_b will start being dependent on h.

3.3 Crystal orientation

The response of the single crystal depends on its orientation. Figure 3.6 shows the stress profiles for the simulations of four films of thickness ranging from 0.125 to 1μm and slip plane orientation $\phi^{(30)} = (30^\circ, 90^\circ, 150^\circ)$. Table 3.2 summarizes characteristics of the results, similar to Table 3.1.

Comparison of Tables 3.1 and 3.2 shows that the average and bulk stress in the single crystals with $\phi^{(30)}$ is for all film thicknesses lower than in the crystals with $\phi^{(60)}$. Nevertheless, the dislocation densities for the $\phi^{(30)}$ films are lower than in the films with $\phi^{(60)}$. This means that for $\phi = 30^\circ$ a lower dislocation density is

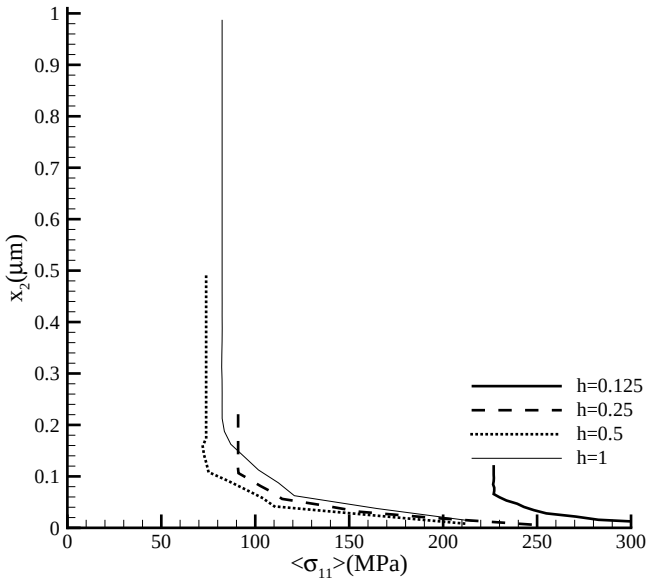

Figure 3.6 Distribution of the average in-plane stress $\langle\sigma_{11}\rangle$ over the film height in films of various thickness with crystal orientation $\phi^{(30)}$.

needed to give the same relaxation. This can be rationalized with equation (3.4): $\cos\phi$ is larger for $\phi = 30^\circ$ than for $\phi = 60^\circ$. Due to the different inclination of the slip planes, the same length of dislocation pile-ups gives a thinner boundary layer for $\phi^{(30)}$ than for $\phi^{(60)}$.

Particularly interesting is the behavior of the film of thickness 0.25μm. In the previous section we have seen that the film stress for $\phi^{(60)}$ does not follow the Hall-Petch relation (3.7) because of insufficient dislocation nucleation. In the $\phi^{(30)}$ orientation, however, fewer dislocations are required for relaxation of the film, so that for this orientation the film does not deviate from the behavior described by (3.7). It should be noticed that for this orientation the stress state in the bulk of the thicker films is approximately the same as in the previous orientation ($\langle\sigma\rangle_b \simeq$ 80MPa), even though there is some more scatter in the results. The coefficient k can be seen as a Taylor coefficient, and has therefore a different value in this orientation. Taking $k = 10$ and $n = 0.5$ in equation (3.8) we find $\sigma = 90$, 94 and 100 MPa for the films with $h = 1$, 0.5 and 0.25μm, respectively, with $\sigma_0 = 80$MPa. If we use for each film $\sigma_0 = \sigma_b$ then $\sigma = 92$, 88 and 111 MPa.

$h(\mu\text{m})$	0.125	0.25	0.5	1
average stress $\langle\sigma_{11}\rangle$ (MPa)	248	114	85	91
bulk stress $\langle\sigma_{11}\rangle_b$ (MPa)	227	91	74	82
dislocation density (μm^{-2})	80	72	40	19
pile-up density (μm^{-2})	24	22	12	4.5
max pile-up length (μm)	0.046	0.094	0.159	0.169

Table 3.2 Characteristics in films with slip planes at $\phi^{(30)}$ at various values of the film thickness.

3.4 Conclusions

Stress relaxation of single-crystal thin films of various thicknesses on a semi-infinite substrate has been simulated using discrete dislocation plasticity. Simulations show that:

- if the film-substrate interface is taken to be perfectly absoring for the dislocations, the stress that the substrate imposes on the film relaxes to a level that depends only on the strength of the weakest nucleation source, independently of the film thickness;
- if the film-substrate interface is impenetrable, stress relaxation is not as efficient as in films with absorbing interface, because dislocations cannot glide into the interface, but pile-up against it, forming a boundary layer characterized by a high stress gradient. The boundary layer is a transition zone between the high stress state at the film-substrate interface and the more relaxed stress state typical of the free surface.
- There is a thickness above which films have a boundary layer with thickness-independent size and average stress. The stress in the rest of the film is very low. Dislocation activity is as intense as in films with a perfectly penetrable interface with the substrate, so that relaxation of the stress in the film bulk is quite good and independent of the film thickness. The size effect in these films is caused by the fact that the size of the boundary layer does not scale with the film thickness.
- In films thinner than a threshold thickness, which depends on the material and on crystal orientation, nucleation is hindered by geometrical con-

straints, i.e. the vicinity of sources to the interface. The thinner the film, the lower is the dislocation activity. Both the average stress in the boundary layer and the stress in the rest of the film increase with decreasing dislocation density. The size of the boundary layer depends on the length of the pile-ups and scales with the film thickness. So, with decreasing film thickness the boundary layer becomes thinner but the stresses in boundary layer and bulk of the film increase. The size effect in these very thin films is nucleation-controlled and is more pronounced than in the thicker films.

References

[1] E. Arzt **46** (1998) 5611.

[2] W.D. Nix, Scripta Mater. **39** (1998) 545.

[3] R. Venkatraman and J.C. Bravman, J. Mater. Res. **7** (1992) 2040.

[4] L.B. Freund, J. Appl. Mech. **43** (1987) 553.

[5] L. Nicola, E. Van der Giessen, A. Needleman, J. Appl. Phys. **93** (2003) 5920.

[6] E. Van der Giessen, A. Needleman, Simul. Mater. Sci. Eng. **3** (1995) 689.

Chapter 4

Relaxation of thermal stress in passivated metal interconnects*

The reliability of many integrated circuits depends on the failure resistance of metallic interconnects. Typical damage processes that can induce failure in interconnects are void formation and electromigration. These processes are strongly influenced by the stress in the lines that develops as a consequence of the thermal mismatch between the metallic lines and their surroundings. The aluminum and copper alloys used for metallization have coefficients of thermal expansion that differ significantly from that of the silicon substrate to which they are usually bonded. Since the interconnects undergo large temperature excursions during processing, and often during service, their thermo-mechanical response is of interest.

Residual stresses in interconnects have been experimentally determined by X-ray diffraction [1, 2] and by curvature measurements [3, 4, 5]. Experiments have shown that the presence of a passivation layer results in a triaxial stress state in the line [2, 3], a stress state that favors void formation, and that the mechanical behavior of passivated lines strongly depends on their aspect ratio [1, 3]. A disadvantage of most experimental techniques is that they do not measure stress accurately in small geometries. Moreover, they only measure the average stress in the lines and do not capture stress gradients, which can be large in small confined geometries. However, energy-filtered electron diffraction methods [6] and glancing angle X-ray diffraction [7] may offer significant improvement in this regard. Numerical analyses based on conventional continuum constitutive characterizations have been used to predict stress evolution in the lines, with the interconnect mainly treated as an elastic [8, 9, 10] or an elastic-perfectly plastic material [1, 11]. A key

*Based on *Relaxation of thermal stress by dislocation motion in passivated metal interconnects*, L. Nicola, E. Van der Giessen, A. Needleman, J. Mater. Res. **19** (2004) 1216 and on *Simulations of dislocation dynamics in aluminum interconnects*, L. Nicola, E. Van der Giessen, A. Needleman, Mat. Res. Soc. Symp. Proc. **731** (2002).

limitation of such approaches is that they cannot account for the size dependence of plastic response in small confined volumes.

In our analyses, plastic deformation in the line is treated as resulting from the collective motion of discrete dislocations which allows stress concentrations and gradients associated with dislocations and dislocation patterns to be captured. Upon cooling from a stress free state, the interconnect is strained by its substrate and by the passivation layer. During thermal loading, the evolution of the stress in the line cross-section and the evolution of the dislocation structure are predicted. Lines with various aspect ratio are analyzed and the results show rather good qualitative agreement with experiments [1, 3] for lines with a small aspect ratio: the larger the aspect ratio, the more elastic the line behavior. The possibility of a size effect is investigated: when the line height or width is sufficiently small (less than 0.5μm) lines with the same aspect ratio but of different size can exhibit a different response. The influence of slip plane orientation, pitch length and passivation layer thickness on stress evolution are also investigated.

4.1 Problem formulation

We consider an infinitely long array of single-crystal lines, perfectly bonded to a semi-infinite substrate and covered by a planar passivation layer (see Fig. 4.1). In the two-dimensional model illustrated in Fig. 4.1 the evolution of the stress field and of the dislocation structure in the cross-section of the lines is studied, assuming plane-strain conditions in the direction along the lines. This configuration is particularly relevant for aluminum lines on a silicon substrate, capped with a silicon-nitride passivation layer. In this type of system, the relatively stiff substrate and passivation layer provide significant constraint on plastic flow in the line in directions perpendicular to the line axis.

In most calculations, a planar crystal is analyzed that is an idealization of an FCC single crystal orientation with the plane of deformation to be the (110) plane, as illustrated in Fig. 4.2. In this orientation, dislocation loops can form that are extended in the line direction. In the limit of an infinitely long line (which is the plane strain limit), these dislocations are straight and of edge character, [12]. Equal slip along the two face diagonals of the $(\bar{1}11)$ and $(1\bar{1}1)$ slip planes is consistent with the $[110]$ direction being perpendicular to the plane of deformation. Thus, slip on the $(\bar{1}11)$ plane effectively occurs in the $[1\bar{1}2]$ direction, while similarly on the $(1\bar{1}1)$ plane slip effectively occurs in the $[\bar{1}12]$ direction. Another

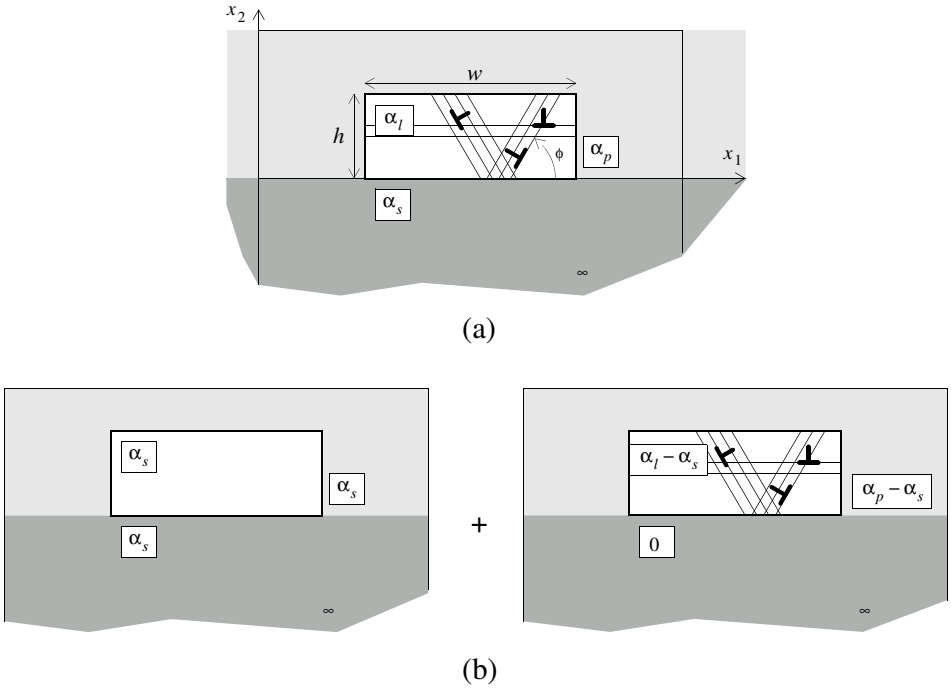

Figure 4.1 (a) Geometry of the line model. (b) Decomposition of the unit-cell problem into a thermo-elastic problem and a plastic relaxation problem.

deformation possibility is slip in the $[110]$ direction on the (111) slip plane. This does not correspond to a dislocation in the (110) plane (which therefore is dashed in Fig. 4.2), but since symmetry demands equal slip on the $(\overline{1}11)$ plane, the composition of these is equivalent to slip on the (001) plane. On the (110) plane the slip directions are therefore inclined at $\pm 54.7^\circ$ and $0^\circ$with the $[\overline{1}10]$ direction, which we identify with the x_1 axis.

In our plane strain analyses, we take the angles between slip directions to be near this FCC orientation and use three slip systems with the slip plane orientations: $\phi^{(1)} = 0^\circ$; $\phi^{(2)} = \phi^{(1)} + 60^\circ$; $\phi^{(3)} = \phi^{(2)} + 60^\circ$. This corresponds to $\phi = 60^\circ$ in Fig. 4.1 and we refer to this as the FCC-like orientation.

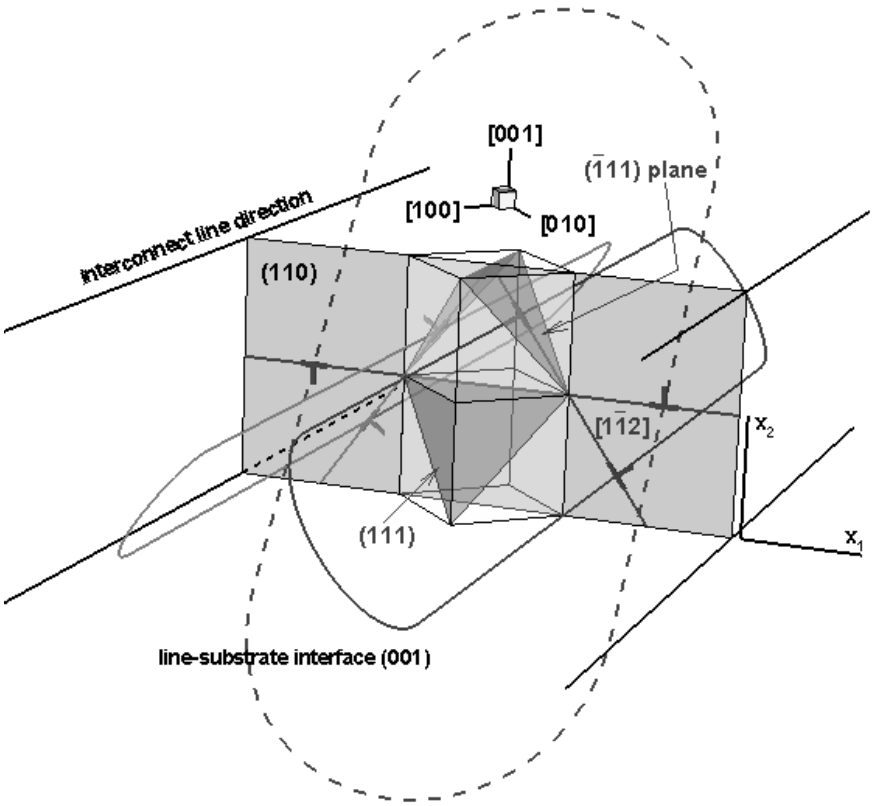

Figure 4.2 Schematic of dislocation motion on FCC slip planes when the crystal is oriented with $[110]$ parallel to the line direction. Because of symmetry and when the line is very long, the slip mode is such that the dislocations can be idealized as three pairs of straight edge dislocations as shown by the $\perp$ symbols.

4.1.1 Boundary value problem

The analyses are carried out on a single cell of width $w+2p$, where w is the width of each line and $2p$ is the spacing (pitch) between lines, Fig. 4.1. In discrete dislocation plasticity, the fields in the line are obtained by coupling the solution of a boundary value problem for the single cell and the analytical solution for the dislocations, treated as line singularities in an infinite elastic medium (for more details see [13]).

The boundary value problem is defined by conditions of equilibrium and com-

patibility and by the constitutive equations:

$$\sigma_{ij,j} = 0\,; \tag{4.1}$$

$$\varepsilon_{ij} = \frac{1}{2}(u_{i,j} + u_{j,i})\,; \tag{4.2}$$

$$\varepsilon_{ij} = \frac{1+\nu}{E}\left(\sigma_{ij} - \frac{\nu}{1+\nu}\delta_{ij}\sigma_{kk}\right) + \alpha\Delta T\delta_{ij}\,, \tag{4.3}$$

where σ_{ij} denotes the stresses, ε_{ij} the strains, u_i the displacements, ΔT is the temperature difference from the initial stress-free state, E is Young's modulus and ν is Poisson's ratio. The linear coefficient of thermal expansion of the line, the substrate and the passivation layer are denoted by α_l, α_s and α_p, respectively. Plane strain implies $\varepsilon_{i3} = 0, i = 1\ldots3$.

The problem is decomposed into two parts: an unconstrained thermo-elastic part, denoted by $(\,)^{\mathrm{th}}$ and a part that is driven by the thermal expansion mismatch, denoted by $(\,)'$ as shown in Fig. 4.1b. Their superposition provides the solution to the problem:

$$u_i = u_i^{\mathrm{th}} + u_i'\,, \quad \varepsilon_{ij} = \varepsilon_{ij}^{\mathrm{th}} + \varepsilon_{ij}'\,, \quad \sigma_{ij} = \sigma_{ij}^{\mathrm{th}} + \sigma_{ij}'\,. \tag{4.4}$$

The $(\,)^{\mathrm{th}}$ part treats the unconstrained thermal expansion of the system line-substrate-passivation layer, under the assumption that all components have the same coefficient of thermal expansion α_s. The solution is trivial. Since $\sigma_{ij}^{\mathrm{th}} = 0$ everywhere, dislocations are not involved in the solution of the $(\,)^{\mathrm{th}}$ part.

In the $(\,)'$ part of the problem, the thermal expansion coefficients of the substrate and passivation layers are taken to be α_s=α_p=0 and that of the line is $\alpha = \alpha_\mathrm{l} - \alpha_\mathrm{s}$. The $(\,)'$ part is subject to the following boundary conditions on the cell:

- stress-free surface

$$\sigma_{12}'(x_1, h_\mathrm{p}) = \sigma_{22}'(x_1, h_\mathrm{p}) = 0\,; \tag{4.5}$$

- periodicity conditions

$$u_i'(0, x_2) = u_i'(w + 2p, x_2)\,. \tag{4.6}$$

When dislocations are present, the solution to the $(\,)'$ part is obtained by decomposing the fields as

$$u_i' = \hat{u}_i + \tilde{u}_i\,, \quad \varepsilon_{ij}' = \hat{\varepsilon}_{ij} + \tilde{\varepsilon}_{ij}\,, \quad \sigma_{ij}' = \hat{\sigma}_{ij} + \tilde{\sigma}_{ij}\,, \tag{4.7}$$

where the $\tilde{(\,)}$-fields are the fields associated to the dislocations treated as individual dislocations in an infinite medium. The $\tilde{(\,)}$-fields are given by the sum of the long-range fields of each dislocation in the cell (including their replicas in the periodic cells),

$$\tilde{u}_i = \sum_I u_i^{(I)}\,, \quad \tilde{\varepsilon}_{ij} = \sum_I \varepsilon_{ij}^{(I)}\,, \quad \tilde{\sigma}_{ij} = \sum_I \sigma_{ij}^{(I)}\,, \tag{4.8}$$

where the superscript (I) denotes the Ith dislocation. The $\tilde{(\,)}$-fields are singular at the positions of the dislocations, and satisfy the standard equations of linear elasticity outside the dislocation core region. The $\hat{(\,)}$-fields in (4.7) are the image fields which correct the $\tilde{(\,)}$-fields in order to satisfy the boundary conditions (4.5) and (4.6) on the unit cell, cf. [13].

4.1.2 Rules for dislocation motion

The calculations make use of the same three rules used in the previous study on thin films presented in chapter 2:

- nucleation of a dipole from a point source occurs when the Peach-Koehler force on the source is larger than the nucleation strength $\tau_{\text{nuc}} b$ during a time span $t_{\text{nuc}} = 10$ ns. Such a point source is a two-dimensional representation of a Frank-Read source;
- dislocation glide is drag controlled: the velocity of a dislocation is proportional to the Peach-Koehler force acting on it through the drag coefficient $B = 10^{-4}$MPa, $v^{(I)} = B^{-1} f^{(I)}$;
- annihilation of a dipole occurs when the dislocations approach each other within the annihilation distance $L_{\text{e}} = 6b$.

The Peach-Koehler force on dislocation I is given by

$$f^{(I)} = m_i^{(I)} \left(\hat{\sigma}_{ij} + \sum_{J \neq I} \sigma_{ij}^{(J)} \right) b_j^{(I)}\,,$$

with $m_i^{(I)}$ the slip plane normal and $b_i^{(I)}$ the Burgers vector of dislocation I.

To accurately resolve dislocation-dislocation interactions, a small time step $\Delta t = 0.05$ns is needed. Therefore, to limit the computing time, the cooling rate is taken to be $\dot{T} = 40 \times 10^6$K/s which is much faster than experimental cooling rates.

4.2 Results and Discussion

We analyze the evolution of thermal stress in the line section while the temperature is decreased by 200K from a stress free and dislocation free state. The stress in the line arises from the thermal mismatch between the line, the substrate and the passivation layer. We take the thermal expansion coefficient of the line to be representative of aluminum, $\alpha_{\rm l} = 23.2 \times 10^{-6}$/K, and use a value representative of silicon, $\alpha_{\rm s} = 4.2 \times 10^{-6}$/K, for the substrate. In practice, aluminum lines on silicon substrates are usually passivated by silicon-nitride, which has a coefficient of thermal expansion that is very close to that of silicon; hence, in our calculations we take $\alpha_{\rm p} = 4.2 \times 10^{-6}$/K. Moreover, for the lines, the elastic properties for aluminum are specified by $E = 70$GPa and $\nu = 0.3$. As in our previous analysis [15] of thin films, differences in elastic properties are neglected, so that the same elastic constants are used for the substrate and passivation layers.

As in our thin film study [15], Frank-Read sources are placed at random positions on the slip planes. The source density in all simulations is $\rho_{\rm nuc} = 60/\mu$m^2. Hence, only some of the slip planes in the line are potentially active. The source strength is taken to be $\tau_{\rm nuc} = 25$ MPa. The interfaces with substrate and passivation layer are modeled as impenetrable. Sources are not placed closer to these interfaces than the nucleation distance $L_{\rm nuc}$: when a dipole is generated, both dislocations must be contained in the line. This implies that there is a zone of thickness $L_{\rm nuc} \sin\phi$ around the line edges that is source free, independent of the line size.

The finite element mesh used to solve for the $\hat{(\,)}$ fields is based on bilinear displacement four-node rectangular elements. A refined mesh is used inside the line, specially around the line corners. The mesh is gradually coarsened in the substrate with the mesh spacing increasing with distance from the line. The number of elements and degrees of freedom depend on the line size, with the meshes used consisting of from 48 to 252 elements inside the line.

4.2.1 Shape effects

All simulations start from a stress and dislocation-free state. As the temperature is decreased, an inhomogeneous stress state develops in the line, with the stress distribution and magnitude depending on the geometry of the line and of the passivation layer. The characteristics of the elastic stress field are key for the relaxation behavior. Therefore, we first present elastic simulations for four lines with various aspect ratios h/w. We take the line height to be constant, $h = 0.5\mu$m, and the line width to vary between $w = 0.25$ and $w = 2\mu$m, so that the aspect ratio ranges from $h/w = 0.25$ to $h/w = 2$ (see Fig. 4.1). In order to keep the line area fraction the same for the four lines, the ratio of passivation layer thickness to line height and the ratio of pitch $2p$ to line width w are fixed at $h_p/h = 2$ and $2p/w = 1$, respectively.

Figure 4.3 shows the distribution of σ_{11}, the stress parallel to the line-substrate interface, in the four lines after cooling by 200K.

The line with $h/w = 0.25$ (Fig. 4.3a) is in a high, rather homogeneous tensile state with edge effects near the interfaces with the passivation layer. As h/w increases, Figs. 4.3b–d, the stress state changes such that σ_{11} in the core of the line is lower. High concentrations of stress are found close to the interface with the substrate and close to the top interface with the passivation layer. The compressive stress in the substrate is very small due to the large size of the substrate. The passivation layer, on average, is in tension between lines, especially for the taller lines. Above the line, the passivation layer is on average in compression.

The effect of dislocation glide on stress evolution is investigated for the same line geometries. The initial response of the line is elastic. The σ_{11} field has the distribution shown in Fig. 4.3 which then, along with the slip plane orientation, determines which source is subjected to the highest resolved shear stress. When the Peach-Koehler force on one of the sources attains the nucleation strength during a period t_{nuc}, the first dipole is nucleated. After nucleation, dislocations move apart on their slip plane, and relax the stress in the line. If they do not meet other dislocations on their path, they glide until they reach the impenetrable interfaces. More dislocations are nucleated and as the dislocation density increases, junctions between crossing dislocations form. These junctions may act as obstacles for other dislocations, but may also trigger dislocation nucleation from nearby sources. The stress field in the lines evolves due to continued cooling and to the nucleation and motion of dislocations.

Figure 4.4 shows the stress field σ_{11} in the lines at final temperature (400K),

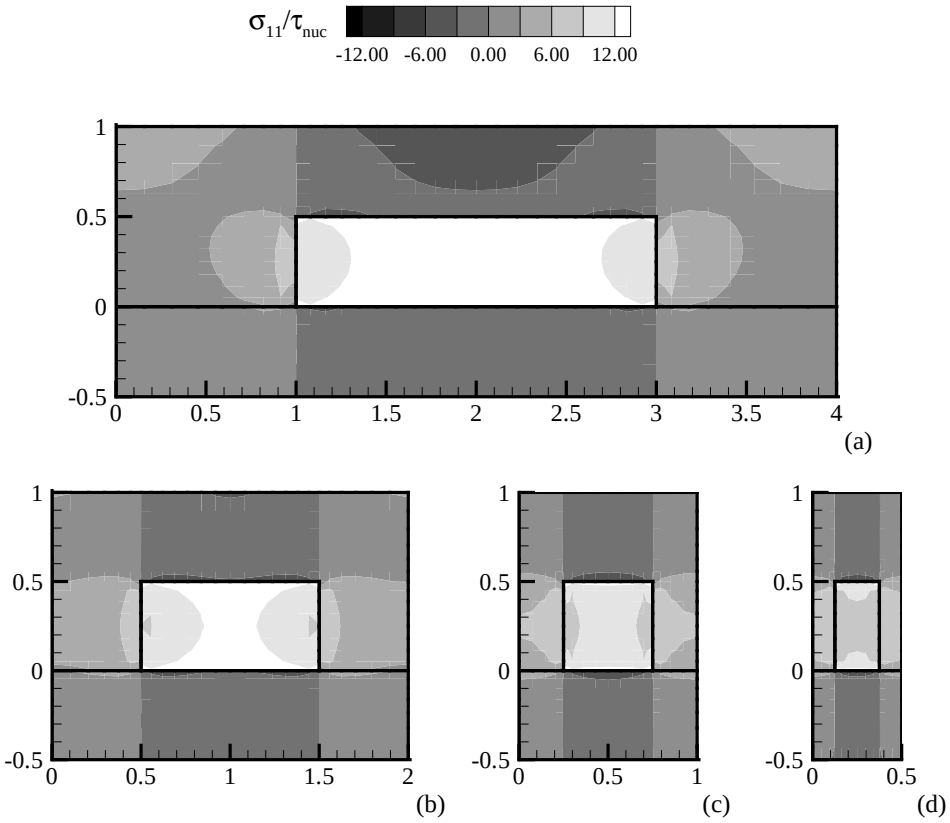

Figure 4.3 The elastic stress state. Contours of σ_{11}, normalized by the nucleation strength τ_{nuc} for four lines of height $h = 0.5\mu$m with various aspect ratios: (a) $h/w = 0.25$, (b) $h/w = 0.5$, (c) $h/w = 1$ and (d) $h/w = 2$.

with the corresponding dislocation distribution superimposed. Many dislocations have nucleated in the lines with aspect ratio $h/w < 1$ (see Figs. 4.4a and 4.4b) and have piled up at the top and at the bottom of the lines. Some dislocations have met other dislocations crossing their slip planes and have formed junctions in the cores of the lines. The dislocation activity in the lines with $h/w = 1$ and $h/w = 2$ is rather limited (see Fig. 4.4c and 4.4d). In the narrow line with aspect ratio $h/w = 2$ (Fig. 4.4d) only two dipoles have nucleated; the motion of these two dipoles does not significantly affect the stress field inside the line, as can be seen by comparing Fig. 4.4d with Fig. 4.3d.

Figure 4.5 shows the evolution of the average stress in the line, $\langle\sigma_{11}\rangle$, during

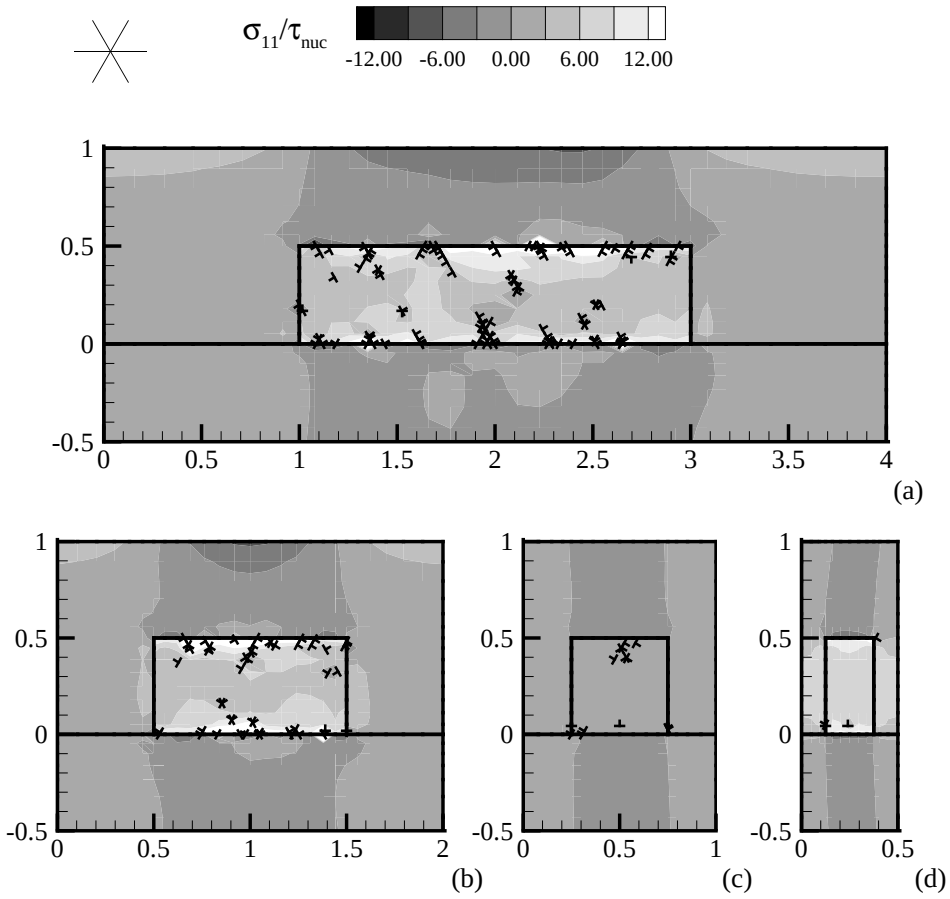

Figure 4.4 Relaxed state at final temperature. Contours of σ_{11}, normalized by the nucleation strength τ_{nuc}, and dislocation distribution for four lines of height $h = 0.5\mu$m with various aspect ratios: (a) $h/w = 0.25$, (b) $h/w = 0.5$, (c) $h/w = 1$ and (d) $h/w = 2$.

cooling. The stress-temperature curves for the four lines considered differ mainly in the elastic slope and in the onset of plasticity (dislocation activity starts earlier in lines with smaller aspect ratios). In lines with $h/w < 1$ the stress at yield is $\sigma_{11}^{\text{y}} \simeq 50$MPa for the parameters used in the calculations. The first dislocation nucleation is immediately followed by many other nucleation events, so that relaxation is very effective until $T \simeq 540$K, especially in the line with $h/w = 0.25$. Then, when the back stress associated with dislocation pile-ups formed at the

interfaces becomes significant, the nucleation rate decreases and the material response becomes harder. This is similar to the findings in [15] for thin films, but even more pronounced due to the four-sided constraints on dislocation motion (note that the formation of long pile-ups is a consequence of the interfaces of the line with the passivation layer and with the substrate being modeled as impenetrable). In lines with $h/w \geq 1$ the yield strength is relatively high (in comparison with the nucleation strength $\tau_{\text{nuc}} = 25\text{MPa}$); for $h/w < 1$: $\sigma_{11}^{\text{y}} \simeq 100\text{MPa}$ with $h/w = 1$ and $\sigma_{11}^{\text{y}} \simeq 150\text{MPa}$ with $h/w = 2$. The trend in these calculations is that stress relaxation by dislocation motion is more effective for smaller aspect ratio lines. Results presented in the following subsection show that this does not hold in general.

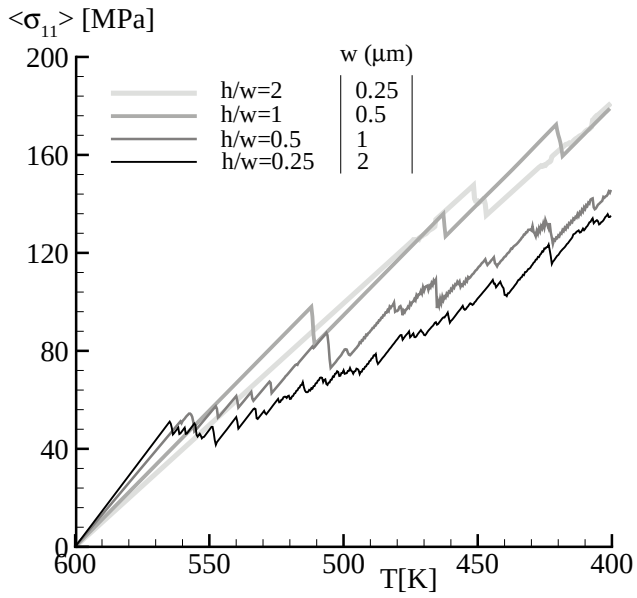

Figure 4.5 Average σ_{11} in the line versus imposed temperature for the four lines with aspect ratios shown in Fig. 4.4.

In order to understand why stress relaxation by dislocation motion is more effective for lines with $h/w < 1$, Fig. 4.6 shows the resolved shear stress at 60° in the four elastic lines normalized by the nucleation strength τ_{nuc}. In the line with $h/w = 2$ (Fig. 4.6d) there are only two very small regions near the line corners where the resolved shear stress $\tau^{(2)}$ on the slip planes at $\phi^{(2)} = 60^\circ$ exceeds the

nucleation strength. Only sources in these regions can nucleate dislocations. In flat lines, $h/w < 1$, the resolved shear stress magnitude is greater and distributed more homogeneously in the line, so that almost all sources available can be activated. It is also important to note that the small aspect ratio lines, $h/w < 1$, have more dislocation sources than the lines with $h/w \geq 1$; since h is fixed, lines with $h/w < 1$ have a larger cross-sectional area but the same source density as lines with $h/w > 1$.

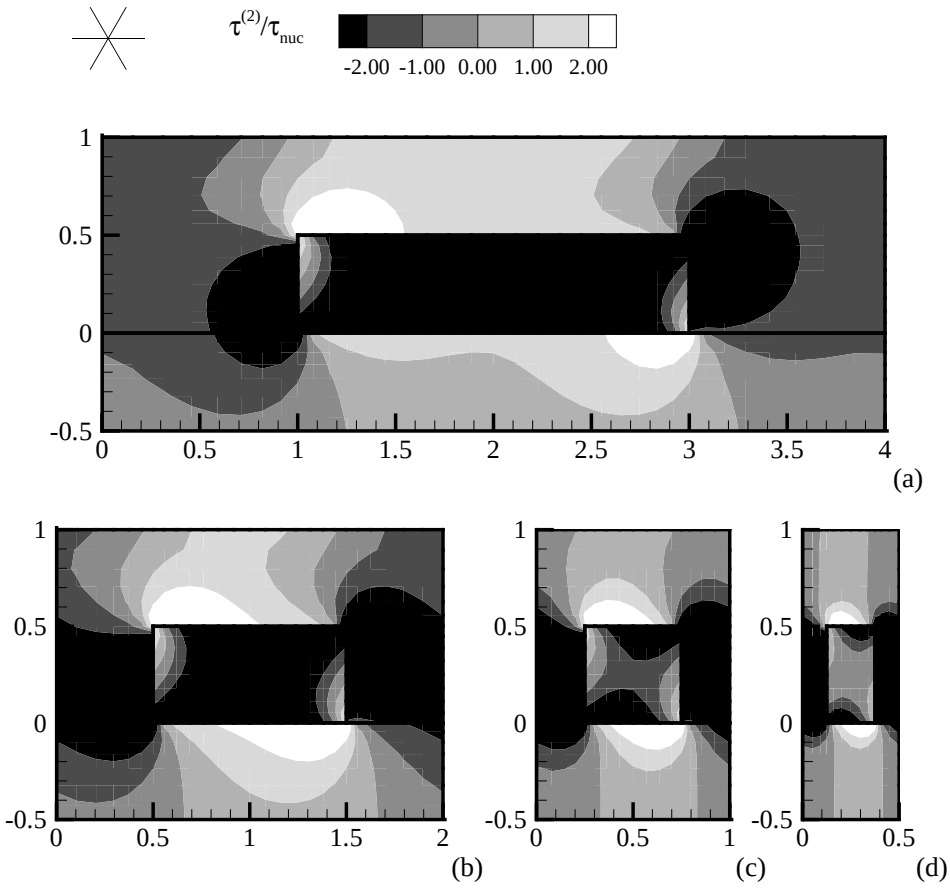

Figure 4.6 Distribution of the shear stress resolved on the slip planes at 60°, normalized by the nucleation strength τ_{nuc} for four lines of height $h = 0.5\mu$m with various aspect ratios: (a) $h/w = 0.25$, (b) $h/w = 0.5$, (c) $h/w = 1$ and (d) $h/w = 2$.

4.2.2 Size effects

To investigate the role of source availability on stress relaxation in the lines, we analyze a set of lines with varying aspect ratio but with the width fixed. The line width is now fixed at $w = 1\mu$m while the line height h ranges between 0.25μm and 1.5μm, so that the aspect ratio range remains between $h/w = 0.25$ and 1.5 for comparison with the previous results. The line area fraction is the same as in Fig. 4.3 and the elastic response of the lines is size independent. The use of a fixed width ensures that the ratio between the passivation layer thickness and the line height remains $h_p/h = 2$ and the ratio between pitch and line width is still $2p/w = 1$. The σ_{11} stress and dislocation distributions at 400K are shown in Fig. 4.7. The line shown in Fig. 4.7a has the same aspect ratio ($h/w = 0.25$) as the line in Fig. 4.4a, but the cross-sectional area (0.25 μm^2) and the number of Frank-Read sources is the same as for the line in Fig. 4.4c. Despite the reduced number of sources (15 for the line in Fig. 4.7a versus 60 for the line in Fig. 4.4a), there is considerable dislocation activity and the stress in the line core has relaxed significantly. The availability of sources is greater in the present lines with $h/w \geq 1$, Figs. 4.7c and d, and the number of dislocations nucleated during the simulation is larger by a factor between 2 and 10 than for the lines in Figs. 4.4c, d. This is mainly due to the higher probability of a source being located in the zones with a high resolved shear stress. Nevertheless, despite the higher nucleation activity, stress relaxation in the lines has not been effective. This is seen in Fig. 4.8, where the average stress in the line, $\langle\sigma_{11}\rangle$, is plotted as a function of temperature. The response of lines with $h/w \geq 1$ is still almost elastic as in Fig. 4.5.

The inefficiency of relaxation for $h/w \geq 1$ is because the stress state in these lines is very close to being hydrostatic, as is shown in Fig. 4.9a, plotting $\langle\sigma_{11}\rangle$, $\langle\sigma_{22}\rangle$ and the average hydrostatic stress,

$$\langle\sigma_h\rangle = \frac{1}{3}[\langle\sigma_{11}\rangle + \langle\sigma_{22}\rangle + \langle\sigma_{33}\rangle], \tag{4.9}$$

in a line with $w = h = 1\mu$m. Figure 4.9b shows similar plots for a line with $h/w = 0.25$, $w = 2\mu$m and $h = 0.5\mu$m. The elastic stress in this flatter line is less hydrostatic, and $\langle\sigma_{11}\rangle$ is reduced, even though $\langle\sigma_{22}\rangle$ is not affected by dislocation glide. From Fig. 4.9a it seems that when dislocations nucleate, $\langle\sigma_{11}\rangle$ reduces but the transverse stress $\langle\sigma_{22}\rangle$ increases somewhat, thus maintaining the same hydrostatic stress state.

Taking a closer look at the dislocations in Figs. 4.4 and 4.7 one can see that lines with $h/w < 1$ are characterized by many dislocation pile-ups at the top and

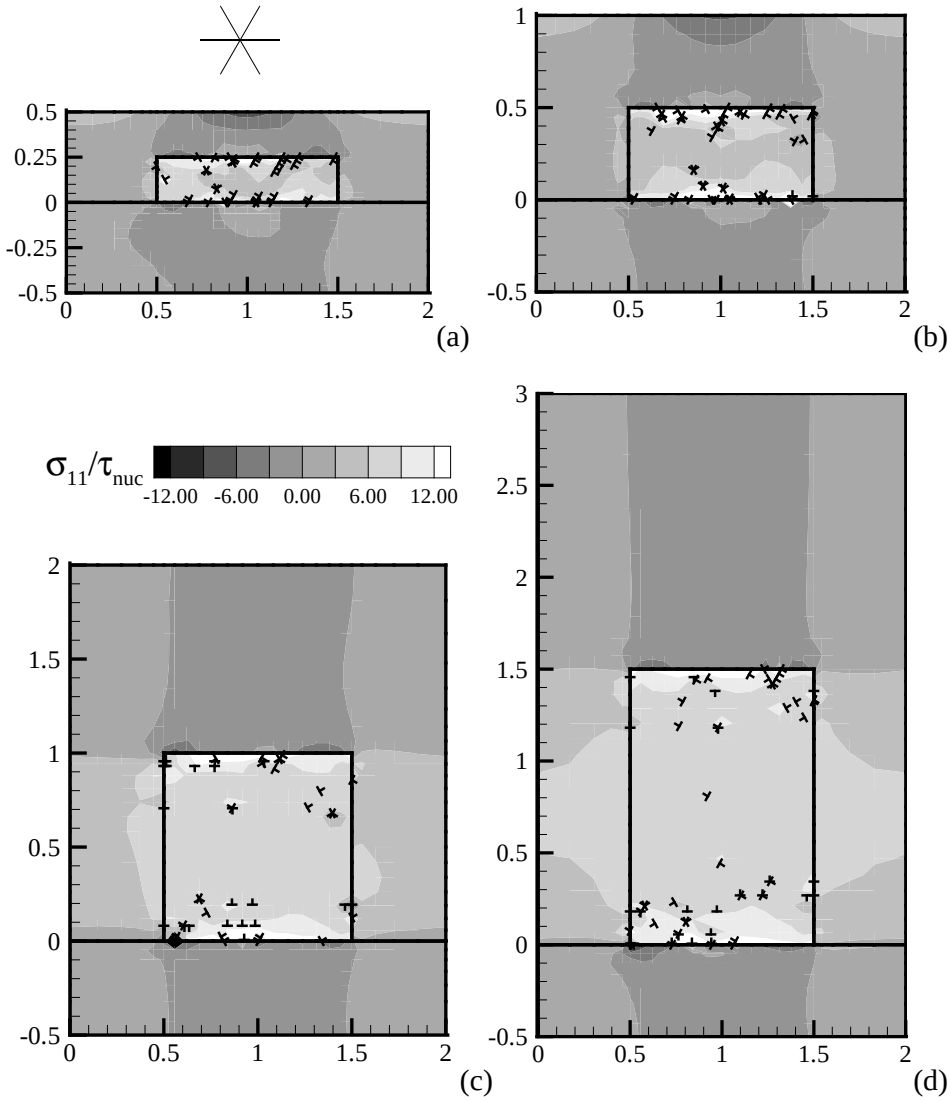

Figure 4.7 Contours of σ_{11}, normalized by the nucleation strength τ_{nuc} and dislocation distribution at final temperature for four lines of width $w = 1\mu$m with various aspect ratios: (a) $h/w = 0.25$, (b) $h/w = 0.5$), (c) $h/w = 1$ and (d) $h/w = 1.5$.

at the bottom of the lines. The magnitude of the net Burgers vector at the top of the line corresponds approximately to a super-dislocation with Burgers vector in the $-x_1$ direction. The dislocations at the bottom are equivalent to a super-

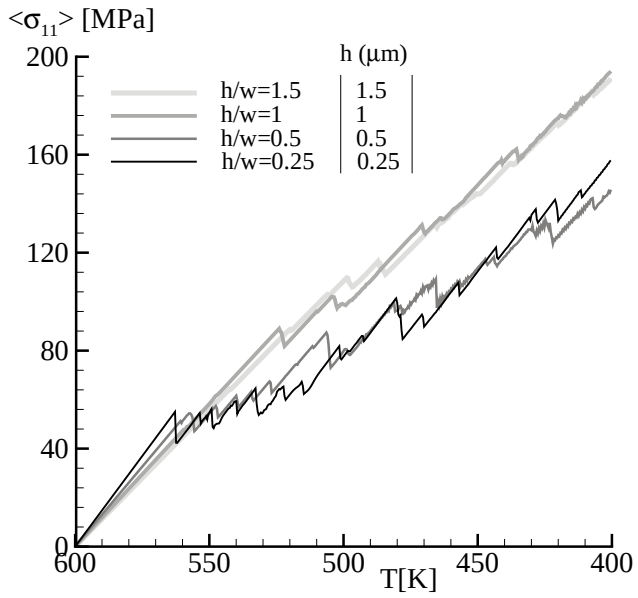

Figure 4.8 Average σ_{11} in the line versus imposed temperature for the four lines with width $w = 1\mu$m and aspect ratios: (a) $h/w = 0.25$, (b) $h/w = 0.5$, (c) $h/w = 1$ and (d) $h/w = 1.5$ of Fig. 4.7.

dislocation with the opposite-signed Burgers vector. This dislocation structure is efficient in the relaxation of $\langle\sigma_{11}\rangle$, since it corresponds to the idealized picture of misfit dislocations at the top and at the bottom of the line. According to the same idealized picture, relaxation of $\langle\sigma_{22}\rangle$ would require misfit dislocations at the line edges with their Burgers vector pointing in the x_2 direction on the left-hand edge and in the $-x_2$ direction on the other side. However, during the simulations, opposite net Burgers vectors develop on these sides. This observation emphasizes that a high dislocation density is not always effective in relaxing the stresses; what matters is the plastic straining, which depends on the distance that dislocations travel on the slip planes, and on the slip plane orientation. Dislocations on slip planes parallel to the line-substrate interface are not effective in relaxing $\langle\sigma_{11}\rangle$.

Comparison of Fig. 4.8 with Fig. 4.5 shows that the lines with $h/w = 0.25$ but of different size exhibit different hardening behaviors; the stress increase in the small line in Fig. 4.7a, after 560K, is higher than in the two times larger one in Fig. 4.4a. In fact, the $h/w = 0.25$ line in Fig. 4.8 hardens at least as fast the one with $h/w = 0.5$. One possible explanation is that the pile-ups which form in the line with

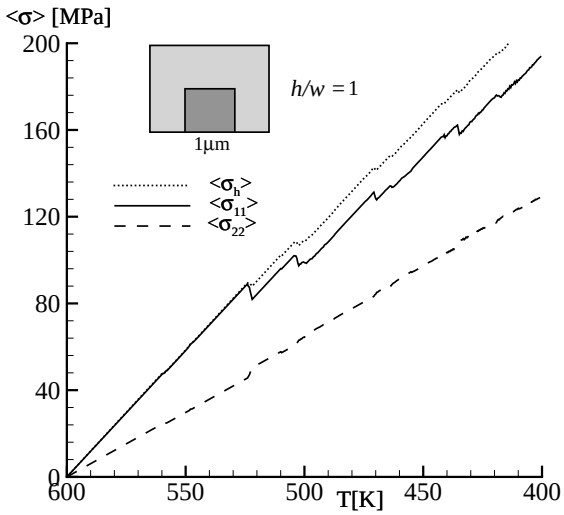

(a)

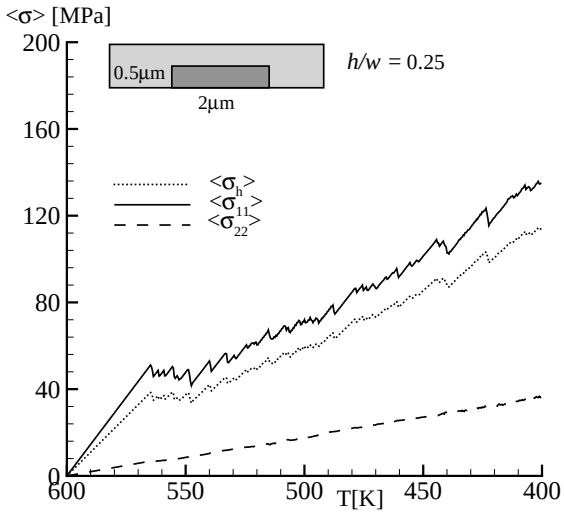

(b)

Figure 4.9 Average stress versus imposed temperature in lines with the same line area but with different aspect ratios: (a) $h/w = 1$; (b) $h/w = 0.25$.

$h = 0.25\mu$m are on average closer to the dislocation sources, so that their back stress inhibits nucleation. The back stress works against the formation and glide of new dislocations, which would make the pile-ups longer, and therefore hinders stress relaxation. This is similar to the size-dependent hardening mechanism seen in thin single-crystal films in [15]. Effective relaxation of $\langle\sigma_{11}\rangle$ for smaller aspect ratio lines, i.e. lines with $h/w < 1$, only occurs if the height of the line is large compared to the length of dislocation pile-ups. The width is not a limitation, because stress relaxation by glide is an effective mechanism only when $w > h$. In all the simulations with $w > h$ the average distance of dislocation sources from the top and the bottom of the lines is smaller than from the sides. Moreover, dislocation pile-ups rarely form at the lateral edges of the line.

4.2.3 Optimization

Since the hydrostatic stress plays a key role in void formation, it is of interest to reduce it as much as possible. We now consider only lines with $h/w < 1$, because relaxation of the $\langle\sigma_{11}\rangle$ stress is effective and because $\langle\sigma_{22}\rangle$ in these lines is smaller than $\langle\sigma_{11}\rangle$ (Fig. 4.9). The average hydrostatic stress in such lines at 400K is significantly lower than in lines with $h/w > 1$ but still around 120MPa.

Effect of slip plane orientation

More effective relaxation of $\langle\sigma_{11}\rangle$ is achieved by changing the slip plane orientation. In this Section, lines with slip planes oriented at $\phi^{(\alpha)} = (30^\circ, 90^\circ, 150^\circ)$ are considered which corresponds to a 30° rotation of the FCC-like orientation in the previous calculations. This can also be considered as corresponding to a BCC-type orientation [12].

The calculation for the line with $h = 0.5\mu$m and $w = 2\mu$m is repeated in the rotated orientation. A comparison is given in Fig. 4.10 of the evolution of the average normal stresses $\langle\sigma_{11}\rangle$, $\langle\sigma_{22}\rangle$ and the hydrostatic stress $\langle\sigma_h\rangle$ for the two orientations. The line with the rotated orientation more effectively relaxes $\langle\sigma_{11}\rangle$: at 400K $\langle\sigma_{11}\rangle \simeq 90$MPa for the BCC-type orientation while $\langle\sigma_{11}\rangle \simeq 140$MPa for the FCC-type orientation. The number of dislocations piled-up at the top and at the bottom of the line in the BCC-type orientation is approximately the same as in the line with the FCC-type orientation, but, due to the orientation of their Burgers vector they are equivalent to $\sqrt{3}$ times more misfit dislocations than in the FCC-type crystal. The dislocation structure in the BCC-type crystal is more effective

in relieving the $\langle\sigma_{11}\rangle$ stress. The BCC-type orientation is also slightly favorable for decreasing $\langle\sigma_{22}\rangle$ and the hydrostatic stress.

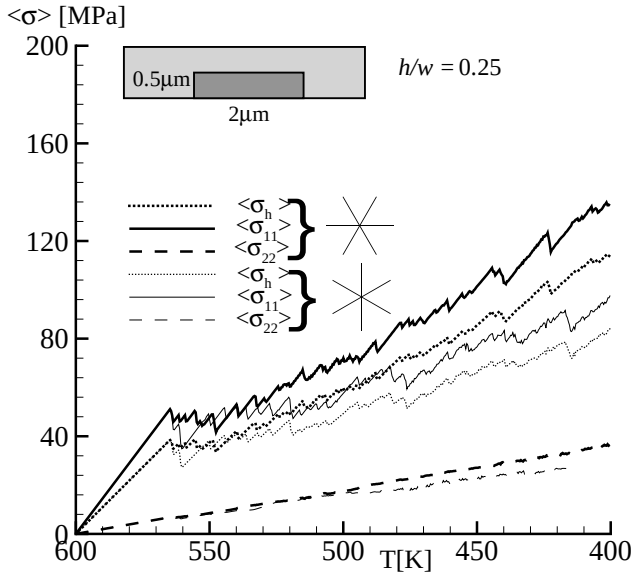

Figure 4.10 Average stresses versus imposed temperature in a line with aspect ratio $h/w = 0.25$ for FCC-type, $\phi^{(\alpha)} = (0^\circ, 60^\circ, 120^\circ)$, and BCC-type, $\phi^{(\alpha)} = (30^\circ, 90^\circ, 150^\circ)$, orientations.

Effect of a shorter pitch

In the calculation for the line with $h/w = 0.5$ ($h = 0.5\mu$m and $w = 1\mu$m), the pitch was $2p = 1\mu$m. We repeat this simulation keeping all the parameters fixed but changing the pitch to $2p = 0.5\mu$m. Neither the geometry of the line nor the number and position of sources are changed. Figure 4.11 shows a comparison of the average in-plane stress evolution in the two lines. When the lines are more closely spaced ($p = 0.25\mu$m) the hydrostatic stress is reduced in the elastic range. At the end of the simulation, at 400K, the average hydrostatic stress in the line with $p = 0.25\mu$m is a little lower than in the line with $p = 0.5\mu$m. This is due to a reduced overall elastic stiffness against $\langle\sigma_{22}\rangle$ for the passivation layer which is a consequence of the change in geometry; as p decreases, the passivation layer between lines is narrower and this reduces the overall stiffness even though the

elastic properties remain the same.

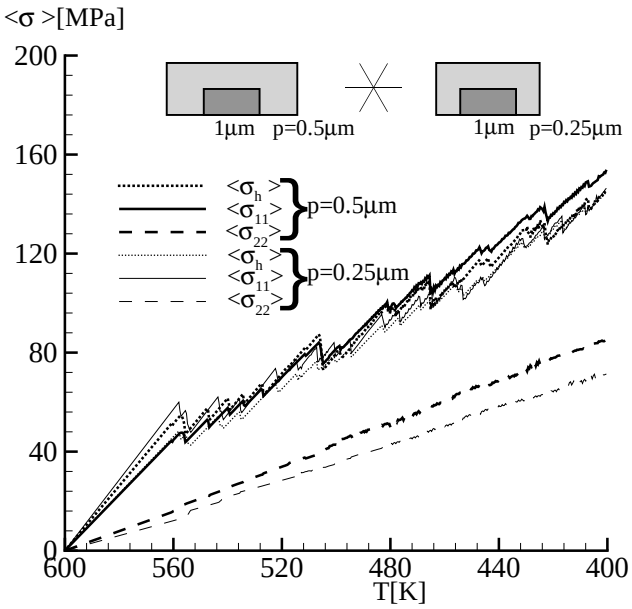

Figure 4.11 Average stresses versus imposed temperature in two lines with $w = 1\mu$m and $h = 0.5\mu$m which differ in the half-pitch: $p = 0.25\mu$m or $p = 0.5\mu$m.

Effect of a thinner passivation layer

The simulation for the line with aspect ratio $h/w = 0.5$ ($h = 0.5\mu$m and $w = 1\mu$m) is repeated with all parameters unchanged except for the height of the passivation layer, which is now $h_{\mathrm{p}} = 0.75\mu$m as compared with the previous value of $h_{\mathrm{p}} = 1\mu$m. Figure 4.12 shows that the stress state that develops in the line with the thinner passivation layer is slightly less hydrostatic than in the line with the thicker layer. The value of $\langle\sigma_{11}\rangle$ in the elastic range is the same in the two simulations, but because the hydrostatic component of the stress is reduced in the line with $h_{\mathrm{p}} = 0.75\mu$m, the resolved shear stress on the slip planes is increased and stress relaxation is slightly more efficient. In the elastic regime, the value of $\langle\sigma_{22}\rangle$ develops more slowly in the line with the thinner passivation layer. Thus, the average hydrostatic stress in the line is smaller if a thinner passivation layer is used.

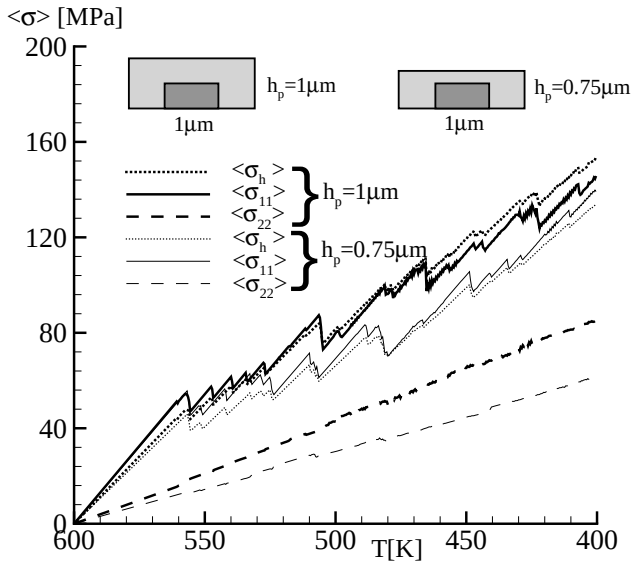

Figure 4.12 Average stresses versus imposed temperature in two lines with $w = 1\mu$m and $h = 0.5\mu$m for various heights of the passivation layer: $h_{\mathrm{p}} = 1\mu$m and $h_{\mathrm{p}} = 0.75\mu$m.

4.3 Lines with non-planar passivation

The planar passivation layer is mainly used in Cu lines obtained by Demascene process. The traditional deposition process for Al-Cu lines involves the use of a non planar capping layer.

In this section stress relaxation in lines with non-planar passivation layer is analyzed. The model is still based on an infinitely long array of single-crystalline lines, each having thickness h and width w, perfectly bonded to an infinitely large substrate and now capped by a non-planar passivation layer (Fig. 4.13).

Results are here presented of three simulations for lines with aspect ratios of $w/h = 1.25, 2.5, 5$. The height of the line is fixed at $h = 0.4\mu$m, while the width ranges from 0.5 to 2μm. The thickness of the passivation layer is the same in all simulations.

The evolution of the average value of σ_{11} in the line, $\langle\sigma_{11}\rangle$, is plotted as a function of the temperature reduction in Fig 4.14. The curves show that the elastic response depends on the line aspect ratio. With $w/h = 5$, the average stress in the

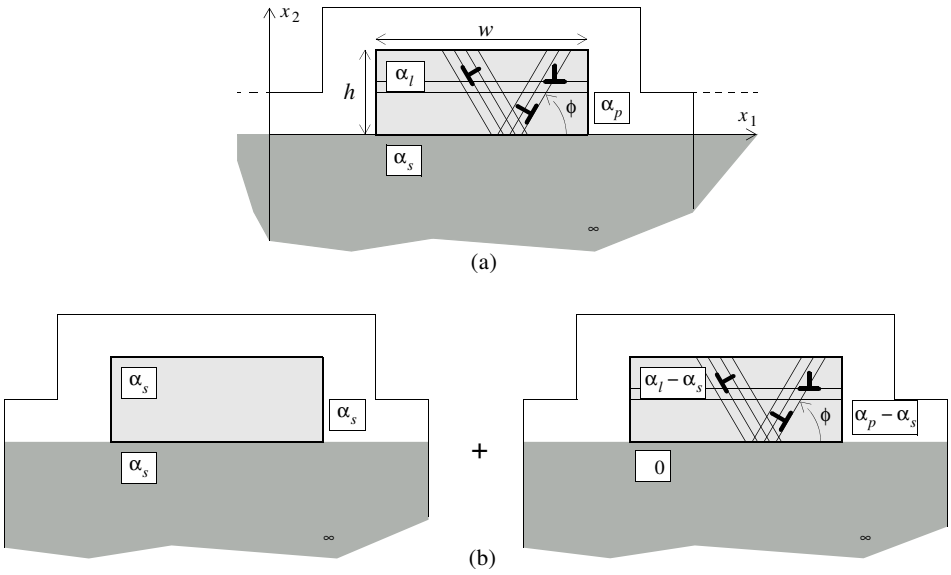

Figure 4.13 Decomposition used to solve the fields in a dislocated line on a substrate with non planar passivation layer.

elastic regime builds up faster than in the lines with smaller aspect ratios. As a consequence, plastic deformation starts earlier and is more effective for larger width-to-height ratios.

Figure 4.15 shows the distribution of the dislocations and the transverse stress σ_{11} in the cell at the end of the cooling process. The stress is normalized by the nucleation strength. The compressive stress in the substrate (only its upper part is seen in the figure) is very low on average, because of the large thickness of the substrate. Only near the interface with the line do the stresses in the substrate reach high values, caused by the fields of the dislocations piled up there. The pile-ups formed at the top and bottom of the line lead to the development of two highly stressed boundary layers. The hard boundary layers are more distinct in the line with the largest aspect ratio $w/h = 5$ (Fig. 2c), where plastic relaxation has been more effective. Stresses in the core of the line are very low in this case in comparison with the line with aspect ratio $w/h = 1.25$ (Fig 4.15). With $w/h = 1.25$, there has been very little dislocation activity so that the final stress distribution is very similar to the elastic solution.

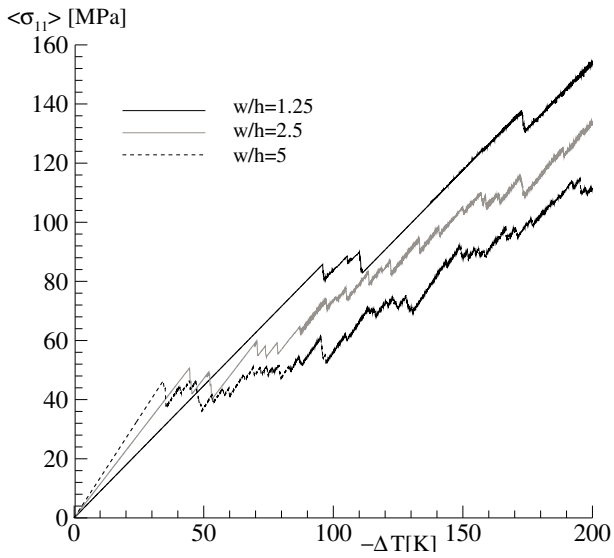

Figure 4.14 Average in-plane stress as a function of ΔT for lines with various aspect ratios.

4.4 Conclusions

Discrete dislocation results have been presented on the evolution of thermal stresses in metal interconnects. A comparison of the mechanical response of lines characterized by the same cross-sectional area shows that:

- the stress that develops in lines with a height-to-width ratio near to or greater than one is nearly hydrostatic. As a consequence, plastic relaxation by dislocation motion is not effective in minimizing the internal stress in these lines;
- lines with a height-to-width ratio that is significantly less then one develop a stress state that has a large deviatoric part so that substantial relaxation by dislocation motion occurs. The dislocations form pile-ups at the substrate and passivation layer interfaces, which give rise to hard boundary layers;
- even if the height-to-width ratio is significantly less than one, plastic relaxation is inhibited if the height of the line is comparable to the dislocation nucleation length (the diameter of a stable loop nucleated from a Frank-Read source). In this case, the average distance of the sources to the line

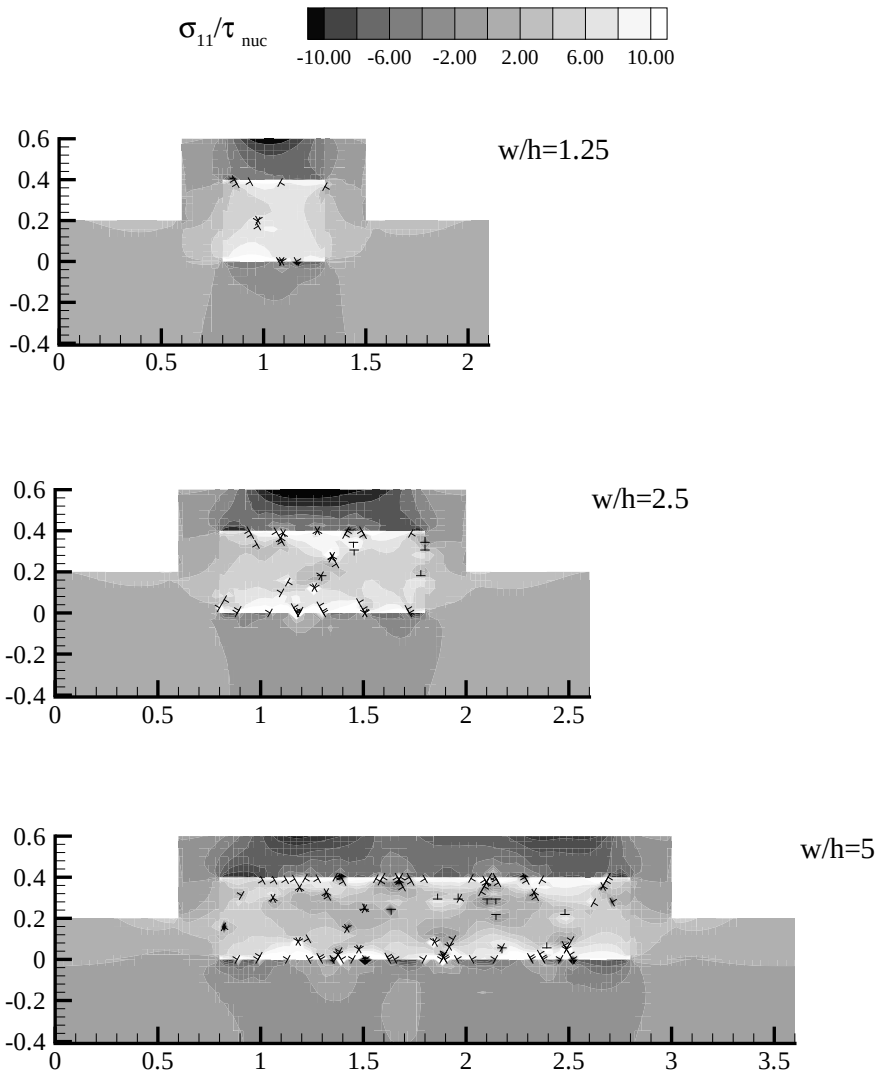

Figure 4.15 In-plane stress and dislocation distribution after cooling by 200K.

boundaries is small enough for the back stress associated with the boundary dislocation pile-ups to retard nucleation throughout the line;

- the effectiveness of plastic relaxation is orientation dependent. In the cal-

culations here, plastic relaxation is more effective for crystals with $\phi^{(\alpha)} = (30^\circ, 90^\circ, 150^\circ)$ (BCC-type) than for crystals with $\phi^{(\alpha)} = (0^\circ, 60^\circ, 120^\circ)$ (FCC-type);

- a shorter pitch tends to reduce the hydrostatic stress in the line, because of a reduction in the stress parallel to the line-substrate interface;
- the difference between the thermal expansion coefficients of the substrate and the passivation layer, as well as the elastic mismatch between the line, the passivation layer and the substrate have been neglected in the calculations here. Accounting for these differences will alter the hydrostatic part of the elastic stress state and thereby the subsequent stress relaxation.

References

[1] A. Saerens, P. Van Houtte, A. Witrouw, Mater. Sci. Forum **347** (2000) 556.

[2] P.A. Flinn, C. Chiang, J. Appl. Phys. **67** (1990) 2927.

[3] I.-S. Yeo, S.G.H. Anderson and P.S. Ho, J. Appl. Phys. **78** (1995) 953.

[4] A. Wikström, P. Gudmundson, Acta Mater. **48** (2000) 2429.

[5] M.A. Moske, P.S. Ho, D.J. Mikalsen, J.J. Cuomo, R. Rosenberg J. Appl. Phys. **74** (1993) 1716.

[6] S. Krämer, J. Mayer, C. Witt, A. Weickenmeier and M. Rühle, Ultramicroscopy **81** (2000) 245.

[7] B.A. van Brussel and J.Th. De Hosson, Appl. Phys. Lett. **64** (1994) 1585.

[8] Y.-L. Shen, J. Appl. Phys. **82** (1997) 1578.

[9] T.-S. Park, S. Suresh, Acta Mater. **48** (2000) 3169.

[10] P. Gudmundson, A. Wikström, Microelectron. Eng. **60** (2002) 17.

[11] A. Gouldstone, Y.-L. Shen, S. Suresh and C.V. Thompson, J. Mater. Res. **13** (1998), 1956.

[12] J.R. Rice, Mech. Mater. **6** (1987) 317.

[13] E. Van der Giessen, A. Needleman, Modelling Simul. Mater. Sci. Eng. **3** (1995) 689.

[14] L.P. Kubin, G. Canova, M. Condat, B. Devincre, V. Pontikis and Y. Bréchet, Solid State Phenomena **23**–**24** (1992) 455.

[15] L. Nicola, E. Van der Giessen, A. Needleman, J. Appl. Phys. **93** (2003) 5920.

Chapter 5

Size effects in polycrystalline thin films*

In the previous chapters we focused on single crystal films, but thin films are usually polycrystals. Although the only relevant geometric length is still the film thickness, the grain size provides another significant length scale. With the usual deposition techniques, the film thickness and grain size cannot be varied independently; the grains have a columnar structure with an average size approximately equal to the film thickness [1]. Therefore, it is generally difficult experimentally to ascertain the relative roles of grain size and film thickness. Experiments to measure stress evolution at constant grain size have been carried out by Venkatraman and Bravman [2] and more recently by Xiang et al. [3] on free-standing thin films. The simulations presented in this paper are motivated by these experiments. Thermal stress evolution in thin films is analyzed using a two-dimensional model in which film thickness and grain size can be varied independently.

5.1 Problem formulation and method of analysis

The polycrystalline film is modeled as an infinitely long planar array of rectangular grains perfectly bonded to a semi-infinite elastic substrate (Fig. 5.1). Plane strain conditions are assumed and elastic anisotropy of the grains and of the substrate is neglected. Plasticity in the film originates from the motion of the straight edge part of threading dislocations in the $x_1 - x_2$ plane. The film is periodic in x_1 direction with a cell of width w which is taken to contain eight grains. Each grain, of height h and width d, contains three sets of slip planes on which edge dislocations, with Burgers vector b, can nucleate and glide. The angle between the three slip planes in each grain is 60°, and the orientation of grain γ is identified

*Based on *Size effects in polycrystalline thin films analyzed by discrete dislocation plasticity*, L. Nicola, E. Van der Giessen, A. Needleman, Thin Solid Films, to appear and on *Plasticity in polycrystalline thin films: a 2D dislocation dynamics approach*, L. Nicola, E. Van der Giessen and A. Needleman, Mat. Res. Soc. Symp. Proc. **779** (2003).

by the angle ϕ^γ with the film-substrate interface, Fig. 5.1. The grain boundaries as well as the film-substrate interface are modeled as flat and impenetrable to dislocations. The film and substrate are taken to have the same elastic constants, but different coefficients of thermal expansion α_f and α_s, for the film and substrate respectively. Since $\alpha_f > \alpha_s$, cooling of the film-substrate system leads to a tensile stress in the film.

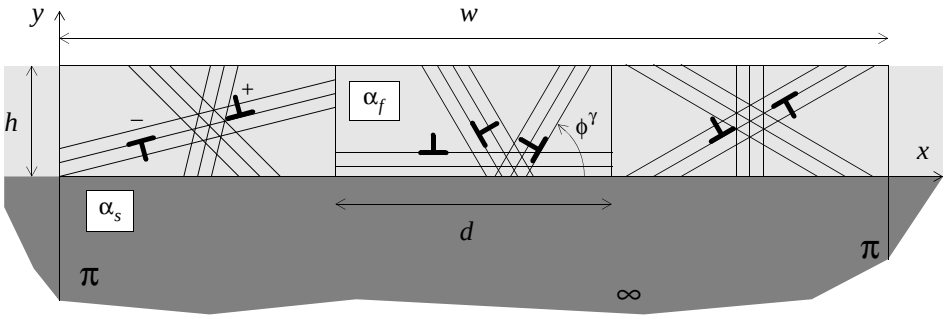

Figure 5.1 Model of the polycrystalline film on an infinite rigid substrate. Only three grains are shown in the schematic drawing, while the simulations use eight grains per unit cell.

As long as the response remains elastic, the boundary value problem for the unit cell in Fig. 5.1 is governed by the equilibrium conditions for the stress σ_{ij}, the relation between strain ε_{ij} and displacement u_i, and the thermoelastic constitutive law

$$\varepsilon_{ij} = \frac{1+\nu}{E}\left(\sigma_{ij} - \frac{\nu}{1+\nu}\delta_{ij}\sigma_{kk}\right) + (\alpha_f - \alpha_s)(T - T_i)\delta_{ij} \tag{5.1}$$

in which T is the temperature, T_i is the temperature in the initial stress-free state, E is Young's modulus and ν is Poisson's ratio. Plastic deformation when it occurs is described by the motion of discrete dislocations, represented as line singularities in the thermo-elastic film material. When dislocations are present, the set of governing equations is extended with a set of constitutive rules for dislocation motion.

Since we focus on stress development in the thin film, the unconstrained contraction that the film-substrate system undergoes with decreasing the temperature is neglected; this strain can be added to the strain fields calculated here to give the total strain (as discussed for the single crystal film analysis in [4]). The bottom of

the substrate is fully clamped, i.e. $u_1 = u_2 = 0$ there. In the finite element calculations, the substrate is taken to be 100 times larger than the thickest film analyzed, which is large enough to mimic a semi-infinite substrate. Periodic boundary conditions are imposed on the unit cell,

$$u_i(0, x_2) = u_i(w, x_2)\,, \tag{5.2}$$

while traction-free conditions characterize the film free-surface,

$$\sigma_{12}(x_1, h) = \sigma_{22}(x_1, h) = 0. \tag{5.3}$$

Because the elastic properties and thermal expansion coefficient are taken to be identical in each grain, the only non-vanishing stress component in the film, prior to dislocation nucleation, is $\sigma_{11} = \sigma_{\mathrm{n}}$ which is given by

$$\sigma_{\mathrm{n}} = -\frac{(\alpha_{\mathrm{f}} - \alpha_{\mathrm{s}})E(T - T_i)}{(1-\nu)}. \tag{5.4}$$

Once dislocations nucleate, the stress in the film is computed using superposition [5]: the singular $\tilde{\sigma}_{ij}^{(I)}$ fields ($I = 1, \ldots, N$) associated with the N dislocations in the unit cell and their replicas in the film are calculated analytically from the isotropic linear elastic, infinite medium fields. The complete solution is obtained by adding an image field $\hat{\sigma}_{ij}$ that ensures that the boundary conditions (5.2) and (5.3) on the unit cell are satisfied. Thus, the stress at each point is given by

$$\sigma_{ij} = \hat{\sigma}_{ij} + \sum_{I=1}^{N} \tilde{\sigma}_{ij}^{(I)}.$$

The image fields are obtained by solving a linear elastic boundary value problem for the unit cell with boundary conditions changing as the dislocation structure evolves. The loading is imposed by a prescribed temperature T that decreases linearly with time.

5.2 Dislocation dynamics

At the beginning of the calculation the film is stress-free and dislocation-free. Dislocation sources are randomly distributed on the slip planes in the film, with a density $\rho_{\mathrm{nuc}} = 60/\mu\mathrm{m}^2$. These point sources mimic Frank-Read sources in the film

and do not evolve during the simulation. Each source is randomly assigned a nucleation strength τ_{nuc} from a Gaussian distribution with average 25MPa and standard deviation 5MPa. As the temperature of the film-substrate system decreases, an increasing homogeneous tensile stress develops in the film until dislocation nucleation occurs at the weakest Frank-Read source when the Peach-Koehler force at this source exceeds the nucleation strength $\tau_{\text{nuc}}b$ during the nucleation time $t_{\text{nuc}} = 10$ns. The Frank-Read source generates a dislocation dipole. The sign of the dipole is determined by the sign of the resolved shear stress. The distance between the two dislocations, L_{nuc}, is taken such that the attractive stress field that the dislocations exert on each other is equilibrated by a shear stress of magnitude τ_{nuc} at nucleation:

$$L_{\text{nuc}} = \frac{\mu}{2\pi(1-\nu)}\frac{b}{\tau_{\text{nuc}}}\,. \tag{5.5}$$

After nucleation, the dislocations glide apart, driven by the Peach-Koehler force acting on them. The Peach-Koehler force on dislocation I is calculated as

$$f^{(I)} = n_i^{(I)}\left(\hat{\sigma}_{ij} + \sum_{J\neq I}\sigma_{ij}^{(J)}\right)b_j^{(I)}\,. \tag{5.6}$$

Dislocation glide is taken to be drag controlled, with zero Peierls stress, so that the velocity of dislocation I is computed directly from the Peach-Koehler force as $v^{(I)} = f^{(I)}/B$, with B being the drag coefficient, taken to have the value $B = 10^{-4}$Pa s.

As loading proceeds, other dislocation sources are activated. Dislocation nucleation at the Frank-Read sources and dislocation glide depend on both the applied thermal loading and the stress fields of the other dislocations. When two dislocation of opposite sign come closer to each other than the specified annihilation distance of $6b$ they are removed from the simulation.

5.3 Results

Simulations have been performed for polycrystalline films of thickness $h = 0.25$, 0.5 and 1μm for a grain size of $d = 0.25$, 0.5 and 1μm. The width of the unit cell is taken to scale with the grain size d and each cell consists of eight grains. Calculations were carried out for five realizations of each polycrystal. Each realization is characterized by the set of grain orientations ϕ^{γ} and the distribution of source locations and strengths. The temperature is decreased linearly with

time from $T_i = 600$K to 400K at a cooling rate of $\dot{T} = 40 \times 10^6$K/s (to limit the computing time). Representative values for silicon and aluminum are taken for the linear thermal expansion coefficients of the substrate and film, respectively: $\alpha_s = 4.2 \times 10^{-6}$/K and $\alpha_f = 23.2 \times 10^{-6}$/K. The Burgers vector has a value representative of copper, $b = 0.25$nm.

The value of σ_{11}, the normal stress parallel to the interface, averaged over the film and then averaged over all realizations of each polycrystal is denoted by $\langle\sigma_{11}\rangle_f$. Curves of $\langle\sigma_{11}\rangle_f$ versus temperature T are calculated and then averaged over the realizations for each polycrystal. These curves are shown in Fig. 5.2. At the beginning of the cooling process $\langle\sigma_{11}\rangle_f$ increases linearly until, after approximately $T - T_i = -15$K, plastic deformation starts at $\approx \langle\sigma_{11}\rangle_f = 38$MPa. This value depends on the choice of the nucleation strength τ_{nuc}. Subsequent hardening in the films depends on both the film thickness h and the grain size d. For each grain size, the hardening rate increases with decreasing film thickness and for a given film thickness, the hardening rate increases with decreasing grain size. Since these two effects reinforce each other, the small grain-thin film, $h = d = 0.25\mu$m, reaches the highest value $\langle\sigma_{11}\rangle_f = 155$MPa; the film with $h = d = 1\mu$m is has the lowest value, $\langle\sigma_{11}\rangle_f = 50$MPa.

For the two extreme cases, $h = d = 0.25\mu$m and $h = d = 1\mu$m, the vertical lines in Fig. 5.2 show the spread in the stress level at 400K for the five realizations. The spread is large, $\simeq 50$MPa, for the film with $h = d = 0.25\mu$m and only $\simeq 10$ MPa for the film with $h = d = 1\mu$m. For the other films, the larger the grain size, the less the spread among the various realizations. This is a statistical effect since the source density is constant ($\rho_{nuc} = 60\text{sources}/\mu\text{m}^2$) for all films, while the size of the unit cell scales with grain size and film thickness.

For each film a characteristic realization is chosen (i.e. the realization for which the stress-temperature curve is closest to the average) to show the stress distribution and the dislocation structure at 400K (Figs. 5.3, 5.4 and 5.5). In these figures the film region is shown together with a small part of the substrate near its interface with the film; the stress in the substrate is very low on average, because of its large size. The stress is normalized by the elastic stress σ_n, eq. (5.4), that would develop in the absence of dislocations. Grain boundaries are indicated by vertical lines, positive dislocations by a $+$, and negative dislocations by a $-$ (see Fig. 5.1). Common to all films is that, due to dislocation glide, the average stress is lower than the elastic stress σ_n (consistent with Fig. 5.2).

In each case, a high-stress region is found at the interface between the film and

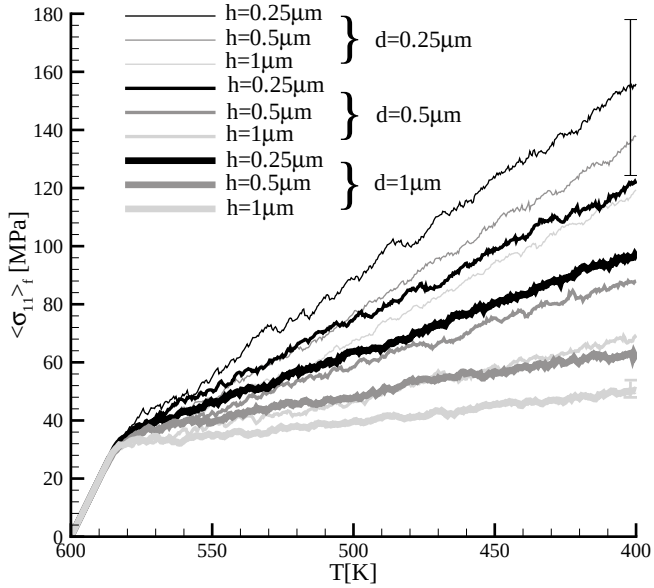

Figure 5.2 Average stress in the film, $\langle\sigma_{11}\rangle_{\mathrm{f}}$, versus temperature T for films of various thickness and grain size. Each curve is an average over five realizations for a given film thickness h and grain size d but with different grain orientations and source distributions. The vertical bars indicate the spread of the results for the two extreme cases: for $h = d = 0.25\mu$m the spread is maximum and for $h = d = 1\mu$m the spread is minimum.

the substrate. The dislocations that are in the films in Figs. 5.3–5.5 are not all the dislocations that have been nucleated during the deformation history: many dislocations have left the film through the free surface. For each nucleated dipole, one dislocation glides toward the film-substrate interface and the other toward the free surface. If both dislocations do not encounter an obstacle along their path, one stops against the impenetrable interface, while the other exits the film, leaving a displacement step in the free surface. However, in many cases, dislocations do find obstacles, which could be a dislocation pile-up on the same slip plane or dislocations on crossing slip planes, or a grain boundary, before reaching the free surface or the interface with the substrate. The total dislocation density in the film

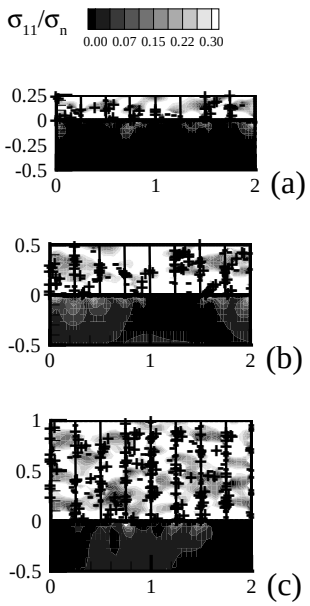

Figure 5.3 Dislocation distribution and contours of σ_{11} at 400K for films with grain size $d = 0.25\mu$m and various values of film thickness: (a) $h = 0.25\mu$m; (b) $h = 0.5\mu$m; and (c) $h = 1\mu$m.

does not provide a direct indication of the stress relaxation. Stress relaxation is a consequence of dislocation glide, while a high density of dislocations can also occur when dislocations have been stopped by an obstacle before much glide has occurred. What is more indicative of the stress relaxation is the number of dislocations that have arrived at the interface with the substrate. The glide of these dislocations has contributed to stress relaxation in the film. At the same time, however, the dislocations that pile-up at the film-substrate interface are also responsible for the high stress region there. Comparison of the dislocation structure obtained at $T = 400K$ in films of various thickness (Figs. 5.3, 5.4 and 5.5) shows that long pile-ups form only in thicker films. This is more evident in the films with large grains.

5.3.1 Thickness-dependent response

As seen in Fig. 5.2, for a given grain size the films exhibit a thickness-dependent response. In order to understand the origin of the thickness dependence, it is

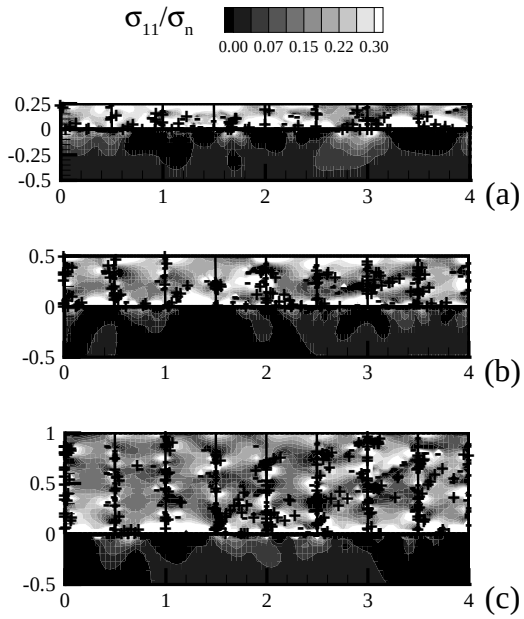

Figure 5.4 Dislocation distribution and contours of σ_{11} at 400K for films with grain size $d = 0.5\mu$m and various values of film thickness (a) $h = 0.25\mu$m; (b) $h = 0.5\mu$m; and (c) $h = 1\mu$m.

useful to examine the stress state in the films at the final temperature, 400K. For various values of x_2 (where x_2 is the coordinate perpendicular to the interface, Fig. 5.1), the average value of σ_{11} along x_1 is calculated over the cell. This cell-average value is then averaged over all realizations for a given polycrystal (i.e. given values of h and d) and is denoted by $\langle\sigma_{11}\rangle$ (the average of this over x_2 is equal to the film average $\langle\sigma_{11}\rangle_{\rm f}$ plotted in Fig. 5.2). Figure 5.6 shows curves of $\langle\sigma_{11}\rangle$ versus x_2. Each plot in Fig. 5.6 pertains to a fixed grain size.

Figure 5.6a, for the films with smallest grain size, indicates that three regions can be identified in the films: (i) a region close to the free surface; (ii) a region close to the interface; and (iii) a central region. Regions (i) and (ii) are characterized by a high stress gradient and by a higher than average stress level. Region (iii) is characterized by an almost uniform value of $\langle\sigma_{11}\rangle$ which is lower than the average film stress. While the thickness of regions (i) and (ii) is approximately independent of the film thickness, the extent of region (iii) decreases with decreasing film thickness. What causes the thickness effect is that the size and average stress

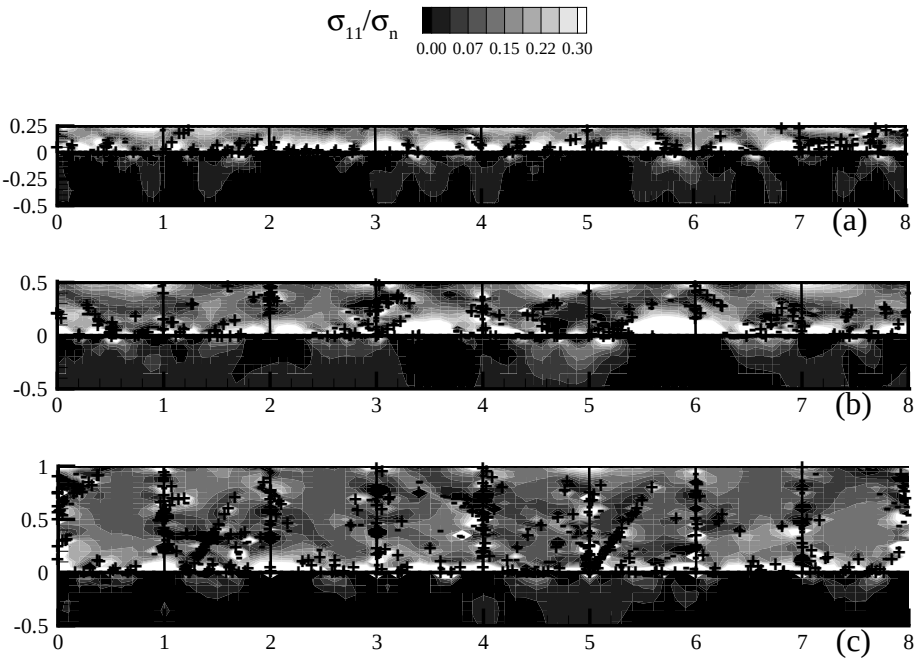

Figure 5.5 Dislocation distribution and σ_{11} at $T = 400$K for films with grain size $d = 1\mu$m and various film thicknesses: (a) $h = 0.25\mu$m, (b) $h = 0.5\mu$m; and (c) $h = 1\mu$m.

in the two boundary layers do not scale with the film thickness. Subsequently, region (i) will be referred to as the interface boundary layer, region (ii) as the surface boundary layer, and region (iii) as the bulk. They are also seen in the thicker films, Figs. 5.6b and c. In the calculations here, the interface and surface boundary layers have a thickness of about 0.15μm. In the thickest films, the surface and interface boundary layers are separated by a distinct bulk region, but the size of this region reduces with film thickness. The bulk region is essentially absent in the $h = 0.25\mu$m films, for all grain sizes considered.

The average stress in the interface boundary layer is considerably higher than in the rest of the film for any thickness and grain size, see Fig. 5.6. The highest value of $\langle\sigma_{11}\rangle$ is found in all films at the film-substrate interface. The value of $\langle\sigma_{11}\rangle$ decreases steeply away from the interface to the stress level in the bulk. The magnitude of the stress at the free surface, $\langle\sigma_{11}\rangle(h)$, and the average value in the surface boundary layer increase with decreasing grain size. For the films

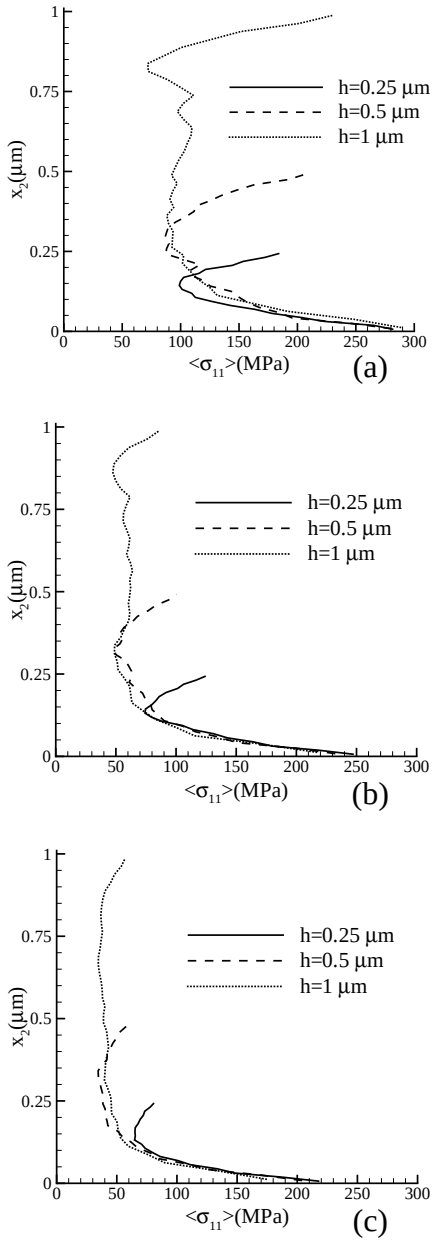

Figure 5.6 Variation of average stress, $\langle\sigma_{11}\rangle$, across the film thickness for films of varying thickness and grain size: (a) $d = 0.25\mu$m, corresponding to Fig. 5.3; (b) $d = 0.5\mu$m, corresponding to Fig. 5.4; and (c) $d = 1\mu$m, corresponding to Fig. 5.5.

with $d = 0.25\mu$m, Fig. 5.6a, the average stress in the surface boundary layer is comparable to that in the interface boundary layer, while in the films with $d = 1\mu$m the stress at the free surface is only slightly larger than in the bulk, Fig. 5.6c. Moreover, for a given grain size, the magnitude of $\langle\sigma_{11}\rangle$ in the two boundary layers is almost independent of film thickness.

The development of the surface boundary layer is a consequence of the films being polycrystalline. Figure 5.6c shows the distribution of $\langle\sigma_{11}\rangle$ for films with $d = 1\mu$m, which are the closest to a single crystal film: the stress gradient in the surface boundary layer is small. In the results for single crystal thin films of varying thickness presented in [4] and [6], a surface boundary layer is not present. On the other hand, an interface boundary layer is present for all single-crystal films in [4] and [6].

5.3.2 Grain size dependent response

Stress-temperature curves with the same color in Fig. 5.2 are for films of the same thickness, but with the grain size varying. For a fixed film thickness, the smaller the grain size, the higher the hardening rate. The data set in Fig. 5.7 is the same data as in Fig. 5.6 but with each plot showing the variation of $\langle\sigma_{11}\rangle$ as the grain size varies. The stress in all three regions increases with decreasing grain size. As can be seen by comparing Fig. 5.7 with the distribution of dislocation density shown in Figs. 5.8, 5.9 and 5.10 for films with $h = 0.25$, $h = 0.5$ and $h = 1\mu$m respectively, there is a correlation between the density and distribution of dislocations in a film and its stress state. However, the correlation is not simple. The dislocation density close to the film-substrate interface is high in all films and this is where the value of $\langle\sigma_{11}\rangle$ is highest. Yet, the stress magnitude is still lower than the stress that would be present without dislocation activity. Figures 5.8, 5.9 and 5.10 show that the dislocation density close to the interface decreases with decreasing grain size and is roughly independent of the film thickness. In films with narrow grains, dislocations have a higher probability of being stopped by a grain boundary on their way to the interface. Fewer dislocations reach the interface and the region close to it, and therefore the stress in the interface boundary layer is higher in films with narrower grains. Consequently, the density of dislocations in the center of films with narrower grains is considerably higher than in films with wider grains, as seen most clearly in Fig. 5.10 for 1μm-thick films. That many dislocations are stopped by the grain boundaries implies that relatively few dislocations exit the free surface. The highly stressed surface boundary layer

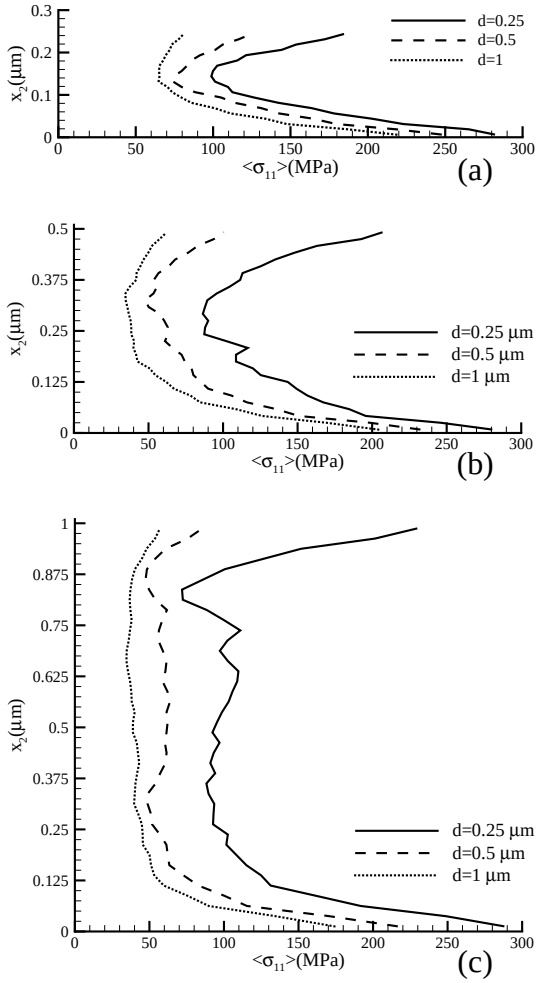

Figure 5.7 Variation of average stress, $\langle\sigma_{11}\rangle$, across the film thickness for films of varying grain size and thickness: (a) $h = 0.25\mu$m; (b) $h = 0.5\mu$m; and (c) $h = 1\mu$m. Same data as in Fig. 5.6 but ordered by grain size.

appearing in films with a small grain size is a result of this. Stress relaxation depends on the ability of dislocations to glide relatively long distances. Grain boundaries reduce the effective glide distance. Furthermore, the dislocations that glide toward the free surface and that, in a single crystal, would exit at the free surface can be blocked near the free surface by the grain boundaries. This gives rise to the free surface boundary layer in a polycrystal with more dislocations be-

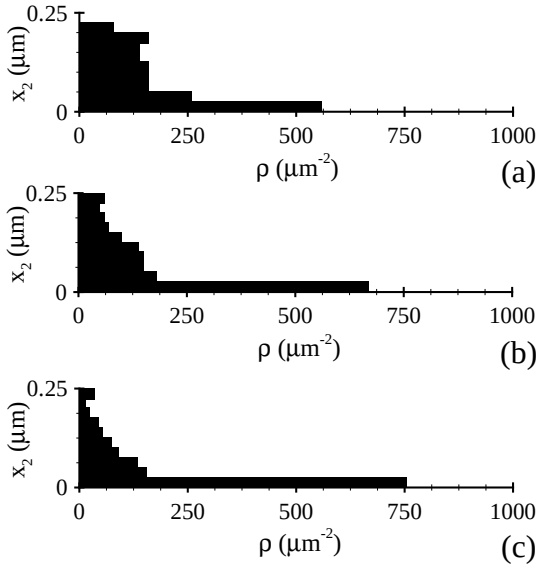

Figure 5.8 Dislocation density across the film thickness for films with thickness $h = 0.25\mu$m and with various grain sizes: (a) $d = 0.25\mu$m; (b) $d = 0.5\mu$m; and (c) or $d = 1\mu$m.

ing blocked in polycrystalline films with small grain size. However, since some of the dislocations do exit at the free surface, the stress level in that boundary layer is less than in the interface boundary layer. The preponderance of slip occurs in the bulk which acts to reduce the elastic (lattice) strains there and thus lower stress levels in the bulk.

5.4 Discussion

The results presented in the previous section reveal that polycrystalline films harden with a hardening rate that is dependent on the film thickness as well as on the grain size. Figure 5.11 plots the h and d dependence in a manner similar to that in experimental studies, e.g. [2, 7, 8]. Our results do not obey a simple scaling of power-law type. In Fig. 5.11a, the results for $d = 0.5\mu$m would fit $\langle\sigma_{11}\rangle_{\mathrm{f}} = \sigma_0 + kh^{-1}$ rather well but for thicker films the scaling approaches Hall-Petch type behavior with an exponent between $-1/2$ and -1. For narrower grains, however, the scaling exponent tends to be smaller than -1. Actual values for p are

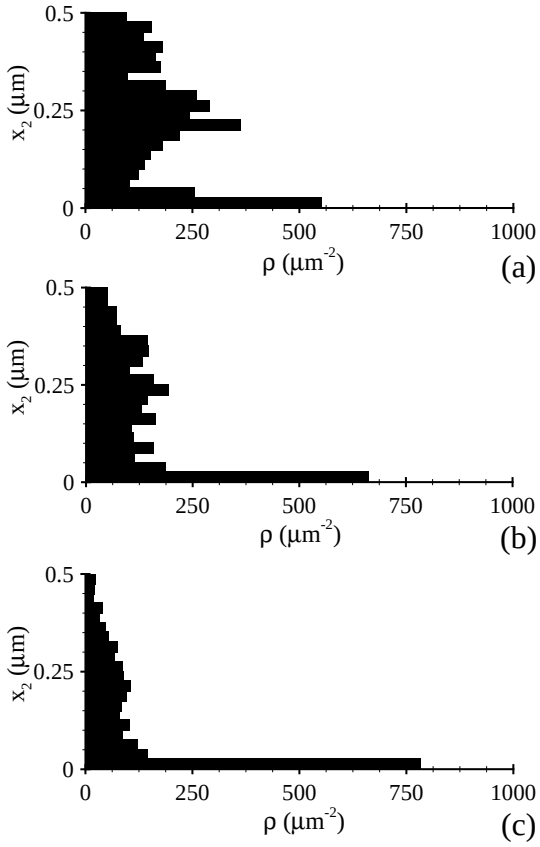

Figure 5.9 Dislocation density across the film thickness for films with thickness $h = 0.5\mu$m and with various grain sizes: (a) $d = 0.25\mu$m; (b) $d = 0.5\mu$m; and (c) $d = 1\mu$m.

listed in Table 5.1. The experimental results presented by Venkatraman at al. [2] for Al films on Si as well as the results obtained by Dehm et al. [7] on epitaxial Al films on Al_2O_3 predict an inverse relation between stress and film thickness. The study of Baker et al. [9] on textured passivated Cu films shows a similar linear trend for films with $\langle 100 \rangle$ texture, while films with $\langle 111 \rangle$ texture tend to have a Hall-Petch exponent < -1.

Table 5.1 also gives values of the exponent q in a grain-size scaling law of the type $\langle \sigma_{11} \rangle_f = \sigma_0 + k_d d^{-q}$, obtained from the data in Fig. 5.11b. The values for the two thicker films are consistent with experimental results of [2], where Hall-Petch

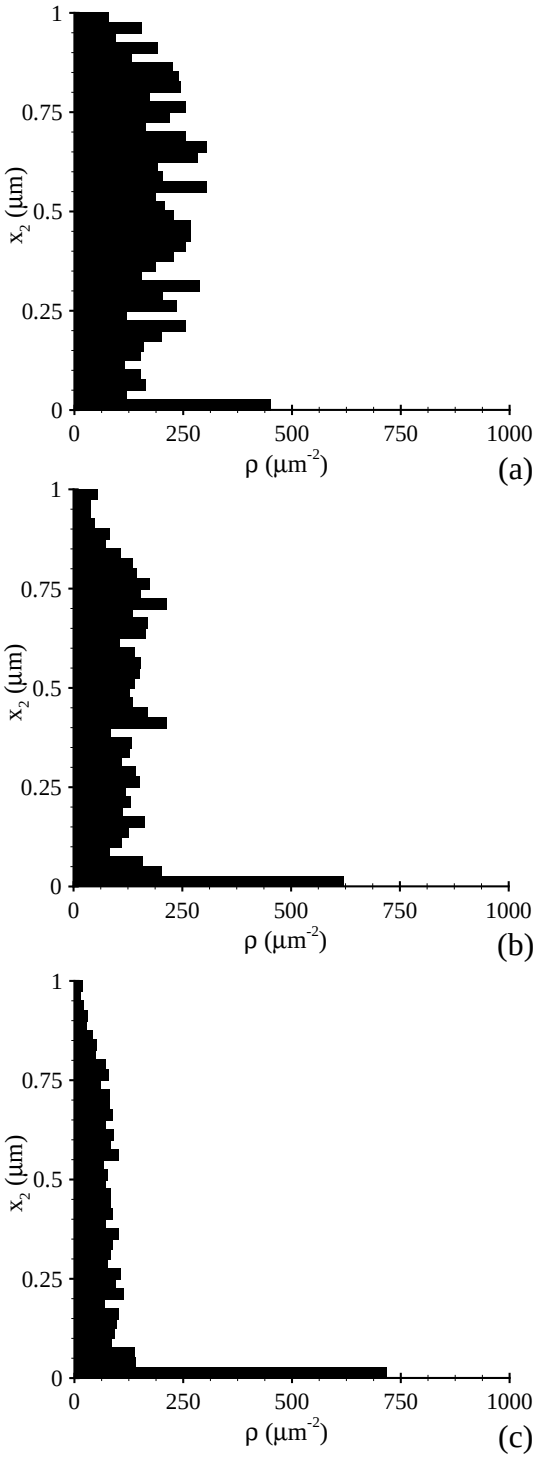

Figure 5.10 Dislocation density across the film thickness for films with thickness $h = 1\mu$m and grain sizes: (a) $d = 0.25\mu$m; (b) $d = 0.5\mu$m; and (c) $d = 1\mu$m.

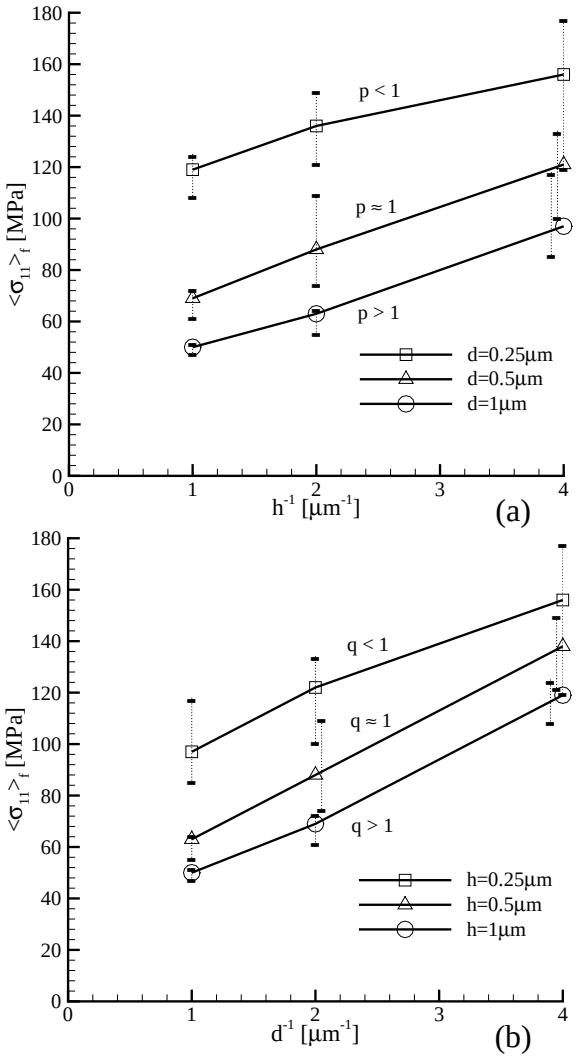

Figure 5.11 Average film stress at $T = 400$K versus film thickness (a) and versus grain size (b); p is the exponent in scaling laws of the type $\langle\sigma_{11}\rangle_{\mathrm{f}} = \sigma_0 + k_{\mathrm{h}} h^{-p}$, which may be used as a fit to the numerical results in (a). Similarly, q in (b) is the exponent in $\langle\sigma_{11}\rangle_{\mathrm{f}} = \sigma_0 + k_{\mathrm{d}} d^{-q}$. Values of all coefficients are given in Table 5.1.

exponents for grain-size strengthening were found which range from -1 to $-1/2$.

The coupling between the grain-size and film-thickness size dependence is complex. A scaling law of the type

$h(\mu\text{m})$	σ_0 (MPa)	p	k_h (MPa μm^{-p})
0.25	42	1.4	8
0.5	50	1	19
1	69	0.4	50
$d(\mu\text{m})$	σ_0 (MPa)	q	k_d (MPa μm^{-q})
0.25	38	1.4	12
0.5	38	1	25
1	45	0.55	52

Table 5.1 Values of the coefficients in $\langle\sigma_{11}\rangle_\text{f} = \sigma_0 + k_\text{h} h^{-p}$ and $\langle\sigma_{11}\rangle_\text{f} = \sigma_0 + k_\text{d} d^{-q}$ fitted from Figs. 5.11a and b, respectively.

$$\langle\sigma_{11}\rangle_\text{f} = \sigma_0 + k_\text{d} d^{-q} + k_\text{h} h^{-p}, \tag{5.7}$$

as proposed by Venkatraman et al. [2] does not provide a good fit to our results; neither does a product expression of the form $\sigma_0(1+k_\text{d} d^{-q})(1+k_\text{h} h^{-p})$.

5.5 Conclusions

We have presented two-dimensional discrete dislocation plasticity simulations of stress evolution in polycrystalline films due to a mismatch in thermal expansion coefficient between the film and its substrate. The grains are columnar and have three slip systems with random orientations. Stress relaxation occurs by the nucleation and subsequent glide of edge dislocations. The grain boundaries and the interface with the stiff substrate are treated as impenetrable for the dislocations.

The stress that builds up in films after a given temperature change is found to depend on grain size and on film thickness, both in the range of 0.25 to 1μm. These size effects are intimately tied to the development of three characteristic regions during deformation:

- an interface boundary layer, independent of film thickness, $\approx 0.15\mu$m thick for the parameters used in the calculations, where the average stress is much higher than the bulk average stress. The average stress in this boundary layer and the stress at the interface increase with decreasing grain size;

- a surface boundary layer, also approximately 0.15μm thick, which is a consequence of the films being polycrystalline and which is characterized by an average stress that increases with decreasing grain size;
- a bulk region between the two boundary layers, where the average stress is lower than the average stress in the film.

While the size of the two boundary layers is essentially independent of film thickness and grain size, their average stress depends on grain size. Thus, the size effect in polycrystalline thin films is a combination of two effects: a thickness-dependent hardening resulting from boundary layers that do not scale with the film thickness; and a grain-size dependent hardening resulting from an increasing stress level throughout the film with decreasing grain size. The origin of the grain-size dependent hardening, i.e. the Hall-Petch effect, is found in the hindering of dislocation motion by grain boundaries coupled with the difficulty of dislocation nucleation in a constrained geometry.

References

[1] W.W. Mullins, Acta Metall. **6** (1958) 414.

[2] R. Venkatraman, J. C. Bravman, J. Mater. Res. **7** (1992) 2040.

[3] Y. Xiang, J.J. Vlassak and M.T. Perez-Prado, Mat. Res. Soc. Symp. Proc. **795** (2004).

[4] L. Nicola, E. Van der Giessen, A. Needleman, J. Appl. Phys. **93** (2003) 5920.

[5] E. Van der Giessen, A. Needleman, Simul. Mater. Sci. Eng. **3** (1995) 689.

[6] L. Nicola, E. van der Giessen, A. Needleman, Philos. Mag., to appear.

[7] G. Dehm, T.Wagner, T.J. Balk, E. Arzt and B.J. Inkson, J. Mater. Sci. Technol. **18** (2002) 113.

[8] O.S.Leung, A. Munkholm, S. Brennan, W.D. Nix, J. Appl. Phys. **88** (2000) 1389.

[9] S.P. Baker, A. Kretschmann and E. Arzt, Acta Mater. **49** (2001) 2145.

Chapter 6

Effect of defect energy on strain gradient predictions of confined plasticity*

In the previous chapters it is shown that the discrete dislocation plasticity framework is suitable of capturing size effects in thin films under tension. In work, for example, by Cleveringa et al. [1] a size dependent response is found for other small structures, including composite materials with specific particle shapes [2]. A limitation of discrete dislocation simulations is that they are applicable only for structures at the micrometer scale, since for larger systems they are computationally too expensive to be practical while they cannot resolve systems which are smaller than approximately a hundredth of a micrometer. For smaller scales, plasticity can be modeled by molecular dynamics simulations. Even though all these models are very helpful in understanding mechanics at a small scale, their validity as predictive tools is extremely limited.

Hence, there is the need for a comprehensive continuum plasticity theory which includes a material length scale. In the last twenty years many strain gradient plasticity theories have been formulated (see for reviews on the subject [3, 4]). Most of the non–local theories proposed [5]–[10] are based on a yield function that depends on gradients of the plastic strain. The mathematical formulation is quite different in the various models and discussion is still open about the order of the differential equations that should be involved in such a theory and the boundary conditions which should be applied. A common drawback of these non local theories is that the length scale(s) they incorporate are unknown material parameters, which need to be fitted to experimental results or to other independent models.

In this chapter the strain gradient theory proposed by Gurtin [11, 12, 13] for single crystals is discussed. The model is of particular interest in the content of this thesis since it focuses on the gradient effect caused by the net Burgers vector

*Based on *Effect of defect energy on strain gradient predictions of confined plasticity*, L. Nicola, E. van der Giessen, M. Gurtin, in preparation.

of dislocations. This single crystal plasticity theory is suitable for comparison with the results presented in chapter 1. The discrete dislocation results will be treated as numerical experimental data to fit the length scale appearing in Gurtin's theory. Different expressions for the defect energy in Gurtin's theory are proposed and discussed in this chapter. The aim is to see which ingredients are capable of capturing the size-dependent response of single crystalline films for different crystal orientations. The findings are aimed at assisting the further development of the theory.

6.1 Basic equations of Gurtin's theory

This theory [12] is meant to characterize single crystals undergoing plastic flow resulting from slip on specified slip systems. Attention is here confined to this theory for circumstances in which the material response is rate independent and geometry changes are negligible.

The theory is based on the standard crystalline decomposition

$$\boldsymbol{\nabla u} = \boldsymbol{H}^{\mathrm{e}} + \boldsymbol{H}^{\mathrm{p}}, \qquad \boldsymbol{H}^{\mathrm{p}} = \sum_{\beta} \gamma^{(\beta)} \mathbb{S}^{(\beta)} \tag{6.1}$$

of the dispacement gradient $\boldsymbol{\nabla u}$ into elastic and plastic parts, $\boldsymbol{H}^{\mathrm{e}}$ and $\boldsymbol{H}^{\mathrm{p}}$, where $\gamma^{(\beta)}$ represents the slip on slip system β. Here $\mathbb{S}^{(\beta)}$, the Schmid tensor for β, has the form

$$\mathbb{S}^{(\beta)} = \boldsymbol{s}^{(\beta)} \otimes \boldsymbol{m}^{(\beta)}, \qquad |\boldsymbol{s}^{(\beta)}| = |\boldsymbol{m}^{(\beta)}| = 1, \qquad \boldsymbol{s}^{(\beta)} \perp \boldsymbol{m}^{(\beta)}, \tag{6.2}$$

with $\boldsymbol{s}^{(\beta)}$ the slip direction and $\boldsymbol{m}^{(\beta)}$ the slip-plane normal.

The governing equations — derived from a formulation of the principle of virtual work that allows for microforce fields $\boldsymbol{\xi}^{(\beta)}$ and $\pi^{(\beta)}$ work-conjugate to slips $\boldsymbol{\gamma}^{(\beta)}$ and slip gradients $\boldsymbol{\nabla\gamma}^{(\beta)}$ — consist of the classical equilibrium condition

$$\operatorname{div} \boldsymbol{\sigma} = 0 \tag{6.3}$$

supplemented by the microforce balance

$$\operatorname{div}\boldsymbol{\xi}^{(\beta)} - \pi^{(\beta)} + \tau^{(\beta)} = 0, \qquad \tau^{(\beta)} = \mathbb{S}^{(\beta)} : \boldsymbol{\sigma}. \tag{6.4}$$

The requirement that the increase in free energy must be not greater than the rate of work leads to the free-energy inequality

$$\dot{\psi} - \boldsymbol{\sigma} : \dot{\boldsymbol{\varepsilon}}^{\mathrm{e}} - \sum_{\beta} (\boldsymbol{\xi}^{(\beta)} \cdot \boldsymbol{\nabla}\dot{\gamma}^{(\beta)} + \pi^{(\beta)} \dot{\gamma}^{(\beta)}) \leq 0, \tag{6.5}$$

where ψ is the free energy (per unit volume) and $\boldsymbol{\varepsilon}^{\mathrm{e}}$ is the elastic strain, the symmetric part of $\boldsymbol{H}^{\mathrm{e}}$. Here, in contrast to the classical crystalline theory, ψ is taken to have the additive form

$$\psi = \tfrac{1}{2}\boldsymbol{\varepsilon}^{\mathrm{e}} \cdot \boldsymbol{\mathcal{C}}\boldsymbol{\varepsilon}^{\mathrm{e}} + \Psi_{\mathrm{D}} \tag{6.6}$$

with strain-energy augmented by a defect energy Ψ_{D}, which we assume to be quadratic in the slip-gradients $\boldsymbol{\nabla}\gamma^{(\beta)}$. Here $\boldsymbol{\mathcal{C}}$ is the standard fourth-order tensor of elastic moduli, which, assuming isotropy, we express in terms of Young's modulus E and Poisson's ratio ν.

Guided by the classical theory and by the free-energy inequality (6.5), $\boldsymbol{\sigma}$, $\boldsymbol{\xi}^{(\beta)}$, and $\pi^{(\beta)}$ are presumed given by the constitutive equations

$$\boldsymbol{\sigma} = \boldsymbol{\mathcal{C}}\boldsymbol{\varepsilon}^{\mathrm{e}}\,, \qquad \boldsymbol{\xi}^{(\beta)} = \frac{\partial \Psi_{\mathrm{D}}}{\partial \boldsymbol{\nabla}\gamma^{(\beta)}}\,, \qquad \pi^{(\beta)} = \varphi^{(\beta)}\mathrm{sgn}\dot{\gamma}^{(\beta)}\,, \tag{6.7}$$

in which slip-system hardening, as described by the internal variables $\varphi^{(\beta)}$, is here taken to be local and isotropic:

$$\dot{\varphi}^{(\beta)} = \sum_{\kappa} H_0 |\dot{\gamma}^{(\kappa)}|\,, \qquad \varphi^{(\beta)}\Big|_{t=0} = \pi_0, \tag{6.8}$$

with π_0 the initial yield strength.

6.2 Macroscopic defect measures in plane strain

With a view toward comparison with two-dimensional discrete dislocation simulations, we henceforth restrict attention to plane strain, with deformation occurring in the (x_1, x_2) plane, so that $\boldsymbol{e}_3$ is the out-of-plane direction.

6.2.1 Burgers vector

The macroscopic Burgers vector is characterized by the Burgers tensor

$$\boldsymbol{G} = \mathrm{curl}\boldsymbol{H}^{\mathrm{p}} = \sum_{\beta} (\boldsymbol{\nabla}\gamma^{(\beta)} \times \boldsymbol{m}^{(\beta)}) \otimes \boldsymbol{s}^{(\beta)}, \tag{6.9}$$

but since we here restrict attention to plane strain, $\boldsymbol{G}$ has the simple form:

$$\boldsymbol{G} = \boldsymbol{e}_3 \otimes \boldsymbol{g}; \qquad \boldsymbol{g} = \sum_{\beta} \partial^{(\beta)}\gamma^{(\beta)}\boldsymbol{s}^{(\beta)}, \tag{6.10}$$

where for each slip system β, $\partial^{(\beta)}\Phi$ is the derivative in the direction of slip:

$$\partial^{(\beta)}\Phi = \boldsymbol{s}^{(\beta)} \cdot \boldsymbol{\nabla}\Phi. \tag{6.11}$$

Thus $\boldsymbol{G}$ may be viewed as representing an edge dislocation with Burgers vector $\boldsymbol{g}$ in the (x_1, x_2) plane and line direction $\boldsymbol{e}_3$. The Burgers vector resolved on slip system β has the form

$$\boldsymbol{g} \cdot \boldsymbol{s}^{(\beta)} = \sum_{\kappa} S^{(\beta\kappa)} \partial^{(\kappa)} \gamma^{(\kappa)}, \tag{6.12}$$

where $S^{(\beta\kappa)}$ are the slip-interaction coefficients

$$S^{(\beta\kappa)} = \boldsymbol{s}^{(\beta)} \cdot \boldsymbol{s}^{(\kappa)}. \tag{6.13}$$

6.2.2 Pile-up fields

We view $\partial^{(\beta)}\gamma^{(\beta)}$, the gradient of $\gamma^{(\beta)}$ in the direction of slip on β, as a macroscopic measure of the pile-up of dislocations on β.

For *double-slip* there is a one-to-one correspondence between the pile-up fields $\partial^{(\beta)}\gamma^{(\beta)}$ and the Burgers vector, since, by eq. (6.10),

$$\boldsymbol{g} \cdot \boldsymbol{m}^{(1)} = (\boldsymbol{m}^{(1)} \cdot \boldsymbol{s}^{(2)}) \partial^{(2)} \gamma^{(2)}, \qquad \boldsymbol{g} \cdot \boldsymbol{m}^{(2)} = (\boldsymbol{m}^{(2)} \cdot \boldsymbol{s}^{(1)}) \partial^{(1)} \gamma^{(1)}. \tag{6.14}$$

Because of this correspondence, the pile-ups can be expressed in terms of the slip-resolutions of the Burgers vector $\boldsymbol{g} \cdot \boldsymbol{s}^{(\beta)}$; in fact,

$$\left.\begin{aligned} \zeta^2 \partial^{(1)} \gamma^{(1)} &= \boldsymbol{g} \cdot \boldsymbol{s}^{(1)} - \mu \boldsymbol{g} \cdot \boldsymbol{s}^{(2)}, \\ \zeta^2 \partial^{(2)} \gamma^{(2)} &= \mu \boldsymbol{g} \cdot \boldsymbol{s}^{(1)} - \boldsymbol{g} \cdot \boldsymbol{s}^{(2)} \end{aligned}\right\} \tag{6.15}$$

with

$$\zeta = \boldsymbol{s}^{(1)} \cdot \boldsymbol{m}^{(2)}, \qquad \mu = \boldsymbol{m}^{(1)} \cdot \boldsymbol{m}^{(2)}.$$

When there are more than two slip systems there is no such correspondence: while the pile-ups determine the Burgers vector via (6.10), the Burgers vector cannot uniquely determine the pile-ups. In fact, it is possible that a set of pile-ups, not all zero, correspond to a null Burgers vector.

6.3 Defect energies

We now discuss various specific choices for the defect energy. Throughout this discussion the constant $\ell > 0$ represents a constitutive length scale.

6.3.1 Burgers-vector energies

We consider the following specific defect energies, here listed together with their associated microstresses:

(i) isotropic energy (cf. [12])

$$\Psi_{\mathrm{I}} = \tfrac{1}{2}\ell^2\pi_0|\boldsymbol{g}|^2, \qquad \boldsymbol{\xi}^{(\beta)} = \ell^2\pi_0\sum_{\kappa} S^{(\beta\kappa)}\partial^{(\kappa)}\gamma^{(\kappa)}\boldsymbol{s}^{(\beta)}; \tag{6.16}$$

(ii) energy dependent on the resolved values of the Burgers vector:

$$\begin{aligned}\Psi_{\mathrm{S}} &= \tfrac{1}{2}\ell^2\pi_0\sum_{\beta,\kappa} k^{(\beta\kappa)}(\boldsymbol{g}\cdot\boldsymbol{s}^{(\beta)})(\boldsymbol{g}\cdot\boldsymbol{s}^{(\kappa)}),\\ \boldsymbol{\xi}^{(\beta)} &= \ell^2\pi_0\textstyle\sum_{\phi,\kappa,\rho} S^{(\beta\phi)}k^{(\phi\kappa)}S^{(\kappa\rho)}\partial^{(\rho)}\gamma^{(\rho)}\boldsymbol{s}^{(\beta)},\end{aligned} \tag{6.17}$$

where

$$k^{(\beta\beta)} = 1 \quad \text{for all} \quad \beta, \qquad k^{(\beta\kappa)} = k, \quad \beta \neq \kappa, \tag{6.18}$$

with k a constant constitutive modulus. We also consider the special case in which $k = 0$, so that:

$$\Psi_{\mathrm{S0}} = \tfrac{1}{2}\ell^2\pi_0\sum_{\beta}(\boldsymbol{g}\cdot\boldsymbol{s}^{(\beta)})^2, \qquad \boldsymbol{\xi}^{(\beta)} = \ell^2\pi_0\sum_{\rho} S^{(\beta\phi)}S^{(\phi\rho)}\partial^{(\rho)}\gamma^{(\rho)}\boldsymbol{s}^{(\beta)}. \tag{6.19}$$

6.3.2 Pile-up energy

The pile-up energy and associated microstress have the form

$$\Psi_{\mathrm{P}} = \tfrac{1}{2}\ell^2\pi_0\sum_{\beta}(\partial^{(\beta)}\gamma^{(\beta)})^2, \qquad \boldsymbol{\xi}^{(\beta)} = \ell^2\pi_0\partial^{(\beta)}\gamma^{(\beta)}\boldsymbol{s}^{(\beta)}. \tag{6.20}$$

Unlike energies dependent on the Burgers vector, the microstress for the pile-up energy does not couple the individual slip systems.

For *double-slip*, we may use (6.15) to conclude that

$$\frac{\zeta^4}{1+\mu^2}\left[(\partial^{(1)}\gamma^{(1)})^2 + (\partial^{(2)}\gamma^{(2)})^2\right] = (\boldsymbol{g}\cdot\boldsymbol{s}^{(1)})^2 + (\boldsymbol{g}\cdot\boldsymbol{s}^{(2)})^2 - \frac{4\mu}{1+\mu^2}(\boldsymbol{g}\cdot\boldsymbol{s}^{(1)})(\boldsymbol{g}\cdot\boldsymbol{s}^{(2)}), \tag{6.21}$$

and hence that the pile-up energy is a special case of (6.17), albeit with a different π_0.

6.4 Summary of DD results for single crystal thin films on a substrate

The problem of a thin film on a semi-infinite substrate subjected to thermal loading as illustrated in Fig 6.1 has been studied using discrete dislocation (DD) simulations in [14] and [15].

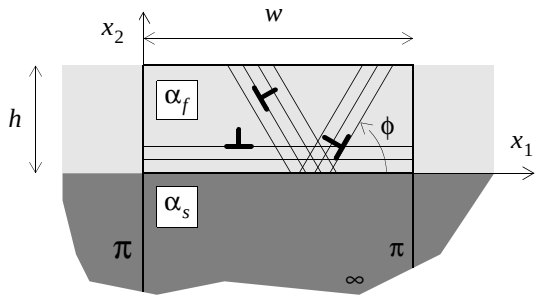

Figure 6.1 Geometry of the film-substrate problem studied in chapter 2. A unit cell of width *w* is analyzed and the height of the substrate is taken large enough to represent a half space.

A quasi-static monotonic thermal loading is imposed by cooling the film–substrate system from an initial temperature T_0, at which film and substrate are stress–free and dislocation–free. The substrate undergoes unconstrained contraction but, due to the mismatch between the thermal expansion coefficient of film (α_f) and substrate (α_s), stress develops in the film; tensile for $\alpha_f > \alpha_s$. After an initial elastic response, dislocations nucleate in the film and partially relax the stress in the film by gliding on three sets of parallel slip planes. We focus on two crystal orientations: $\phi_{60} = (0^\circ, 60^\circ, 120^\circ)$ and $\phi_{30} = (30^\circ, 90^\circ, 150^\circ)$.

Results obtained for three different film thicknesses —$h = 1\mu$m, $h = 0.5\mu$m and $h = 0.25\mu$m— show that the average in-plane stress in the films is dependent on the film thickness. Results also show that hardening depends on crystal orientation: relaxation in films with orientation ϕ_{30} is higher than in films with slip planes oriented ϕ_{60}. Moreover, the size effect is more evident for the ϕ_{60} orientation.

In both crystal orientations, the size dependence originates from the large stress gradient at the film-substrate interface, caused by dislocation pile ups. Instead of a uniform stress distribution across the film height, as in the elastic state or accord-

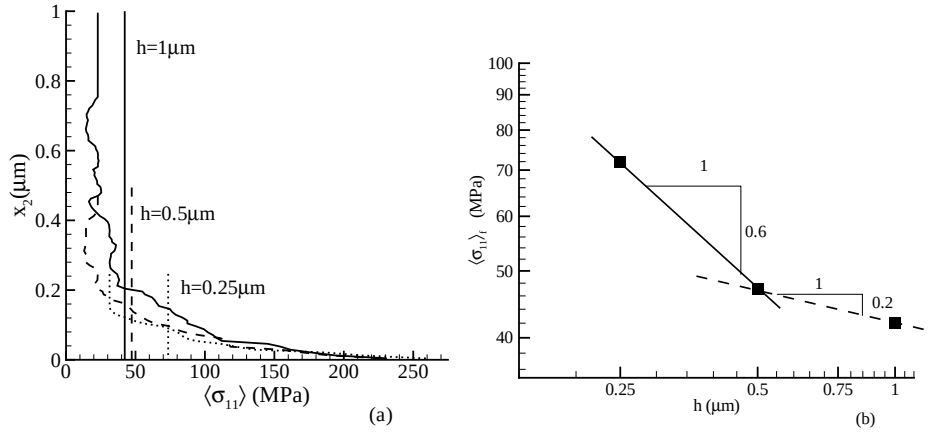

Figure 6.2 DD results [14] after cooling by 200K for the crystal orientation ϕ_{30}. (a) Profiles across the film thickness of the in-plane stress in the films averaged along x_1. (b) Average film stress versus film thickness: data points are fitted to a power law of the form $\langle\sigma_{11}\rangle_{\mathrm{f}} \propto h^{-p}$.

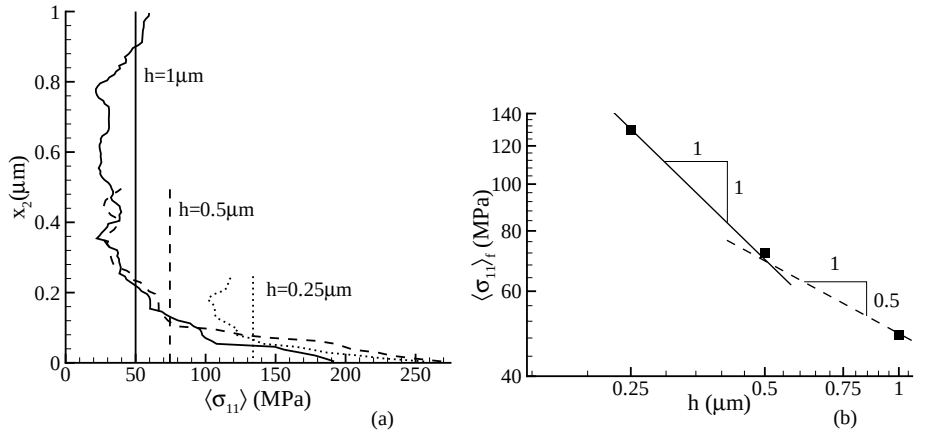

Figure 6.3 DD results [14] for ϕ_{60}. (a) Profiles across the film thickness of the in-plane stress in the films averaged along x_1. (b) Average film stress versus film thickness with data points being fitted to a power law of the form $\langle\sigma_{11}\rangle_{\mathrm{f}} \propto h^{-p}$.

ing to classical local plasticity, the stress increases as the interface is approached, see Fig. 6.2a for ϕ_{30} and see Fig. 6.3a for ϕ_{60}. The vertical lines in these figures indicate the average stress in each film, $\langle\sigma_{11}\rangle_{\mathrm{f}}$. This data is tentatively fitted in Figs. 6.2b and 6.3b to power laws of the form $\sigma_{11} \propto h^{-p}$. Since different values of

p are needed to fit the data, such kind of a power law appears not to be appropriate.

6.5 Closed-form solution of the thin film problem

We simplify the three-slip system model used in the DD simulations (Fig. 6.1) to one with only two slip systems. In the ϕ_{60} orientation, the slip plane parallel

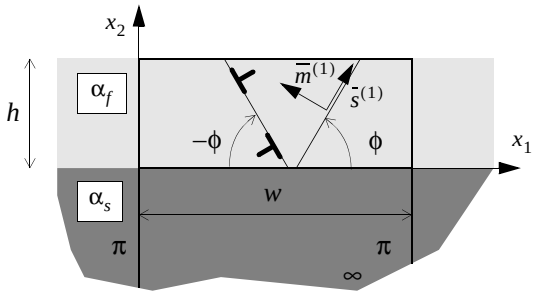

Figure 6.4 Geometry of the thin film problem in symmetric double slip.

to the interface is hardly active and is therefore ignored. For the same reason, the 90° slip plane in the ϕ_{30} orientation is not considered in the application of the continuum theory. Thus, we consider the crystal to be oriented for symmetric double slip with the angle $\phi^{(\beta)}$ between slip plane and film–substrate interface being $\phi^{(1)} \equiv \phi$ and $\phi^{(2)} = \pi - \phi$. Then

$$\boldsymbol{s}^{(1)} = \cos\phi\boldsymbol{e}_1 + \sin\phi\boldsymbol{e}_2\ ,\ \boldsymbol{m}^{(1)} = -\sin\phi\boldsymbol{e}_1 + \cos\phi\boldsymbol{e}_2\ ; \tag{6.22}$$

$$\boldsymbol{s}^{(2)} = -\cos\phi\boldsymbol{e}_1 + \sin\phi\boldsymbol{e}_2\ ,\ \boldsymbol{m}^{(2)} = -\sin\phi\boldsymbol{e}_1 - \cos\phi\boldsymbol{e}_2 \tag{6.23}$$

The macroscopic boundary conditions prescribed are the traction-free conditions at the top of the film:

$$\sigma_{12}(x_1,h) = \sigma_{22}(x_1,h) = 0\,. \tag{6.24}$$

The additional, microscopic boundary conditions are the micro-free condition at the film top, where dislocations can freely leave the film, and the micro-clamped condition at the film–substrate interface where slip cannot occur, i.e.

$$n_i\xi_i^{(\beta)}(x_1,h) = \xi_2^{(\beta)}(x_1,h) = 0\,, \qquad \gamma^{(\beta)}(x_1,0) = 0\,. \tag{6.25}$$

Since the film is infinitely long in the x_1-direction and initially homogeneous, the solution depends only on x_2. With all stress components independent of x_1,

equilibrium together with the macroscopic boundary conditions (6.24) requires that $\sigma_{12} = \sigma_{22} = 0$ throughout the film. The elastic solution is a spatially uniform field $\sigma_{11}(x_2) = \text{const}$, so that yield takes place uniformly in the crystal when $\tau^{(\beta)} = |\pi_0|$ on both slip systems, with

$$\tau^{(1)} = -\tau^{(2)} = -\tfrac{1}{2}\sigma_{11}\sin 2\phi \equiv -\tau. \tag{6.26}$$

Because of the double slip orientation and symmetry,

$$\gamma^{(1)} = -\gamma^{(2)} \equiv -\gamma, \tag{6.27}$$

where it is expected that $\gamma \geq 0$ since $\tau \geq 0$ for the orientations studied here.

Owing to (6.27), the yield conditions on the two slip systems lead to the same differential equation for $\gamma(x_2)$. The time derivative of this equation can be expressed as:

(i) for the isotropic energy, eq. (6.16)

$$\frac{d^2\dot{\gamma}}{dx_2^2} = -\frac{\dot{\sigma}_{11}}{\ell^2\pi_0\sin 2\phi}; \tag{6.28}$$

(ii) for the Ψ_{S0} energy, eq. (6.19)

$$\frac{d^2\dot{\gamma}}{dx_2^2} = -\frac{\dot{\sigma}_{11}}{\ell^2\pi_0 2\sin 2\phi\cos^2\phi}; \tag{6.29}$$

(iii) for the Ψ_S energy, eq. (6.17)

$$\frac{d^2\dot{\gamma}}{dx_2^2} = -\frac{\dot{\sigma}_{11}}{(1-k)\ell^2\pi_0 2\sin 2\phi\cos^2\phi}; \tag{6.30}$$

(iv) for the pile-up energy, eq. (6.20)

$$\frac{d^2\dot{\gamma}}{dx_2^2} = -\frac{\dot{\sigma}_{11}\cot\phi}{\ell^2\pi_0}. \tag{6.31}$$

The stress field $\sigma_{11}(x_2)$ is not uniform and unknown at this stage. Because of symmetry and because strain rate components do not depend on x_1, $\dot{\varepsilon}_{11}$ must be uniform throughout the film. The stress field can be determined by ensuring that this is the case. The total strain splits up into an elastic part, a plastic part and a thermal part given by $\varepsilon_{ij}^T = (1+\nu)\alpha\Delta T\delta_{ij}$ ($(1+\nu)$ stems from the plane

strain formulation). Considering that the substrate expands by $\varepsilon_{11} = (1+\nu)\alpha_s \dot{T}$, compatibility of deformation between the film and the substrate requires that $\dot{\varepsilon}_{11}$ is the same and uniform throughout the film. Hence,

$$(1+\nu)\alpha_s \dot{T} = \dot{\varepsilon}^e_{11} + \dot{\varepsilon}^p_{11} + (1+\nu)\alpha_f \dot{T} \tag{6.32}$$

so that

$$(1+\nu)(\alpha_s - \alpha_f)\dot{T} = \frac{(1-\nu^2)}{E}\dot{\sigma}_{11} + \dot{\gamma}\sin 2\phi\,. \tag{6.33}$$

Eliminating $\dot{\sigma}_{11}$ by means of (6.28), we obtain the following ordinary second-order differential equation for $\dot{\gamma}$:

$$\frac{d^2\dot{\gamma}}{dx_2^2} - \lambda^2\dot{\gamma} = -F \tag{6.34}$$

with constant coefficients λ and F given through

$$\lambda^2 = \frac{E}{(1-\nu^2)\ell^2\pi_0 f(\phi)}\,, \qquad F = \frac{E(\alpha_s - \alpha_f)\dot{T}}{(1-\nu)\ell^2\pi_0 \sin 2\phi\, f(\phi)}\,. \tag{6.35}$$

Here, $f(\phi)$ is a function of orientation ϕ which, depending on the energy considered, takes the following forms:

(i) for the isotropic energy, eq. (6.16)

$$f(\phi) = 1 \tag{6.36}$$

(ii) for the Ψ_{S0} energy, eq. (6.19)

$$f(\phi) = 2\cos^2\phi \tag{6.37}$$

(iii) for the Ψ_S energy, eq. (6.17)

$$f(\phi) = (1-k)2\cos^2\phi \tag{6.38}$$

(iv) for the pile-up energy, eq. (6.20)

$$f(\phi) = \frac{1}{2\cos^2\phi}\,. \tag{6.39}$$

Dependence on the dissipative hardening modulus H_0 was found to be so weak that the solution is here given for $H_0 = 0$. Solving eq. (6.34) subject to the microscopic boundary conditions (6.25) and (6.26) we obtain the solution

$$\dot{\gamma} = \frac{F}{\lambda^2}[1 - \cosh\lambda x_2 + \tanh\lambda h \sinh\lambda x_2], \tag{6.40}$$

where for all energies

$$\frac{F}{\lambda^2} = \frac{(1+\nu)(\alpha_s - \alpha_f)\dot{T}}{\sin 2\phi}. \tag{6.41}$$

Substituting equation (6.40) back into (6.33), we find a linear relation between $\dot{\sigma}_{11}$ and $\dot{T}$, which, after integration from the onset of yield (at temperature $T_y < T_0$) to the current temperature T, gives

$$\sigma_{11} = \sigma_y + (\sigma_n - \sigma_y)[\cosh\lambda x_2 - \tanh\lambda h \sinh\lambda x_2]. \tag{6.42}$$

Here,

$$\sigma_y = -\frac{E}{1-\nu}(\alpha_f - \alpha_s)(T_y - T_0), \qquad \sigma_n = -\frac{E}{1-\nu}(\alpha_f - \alpha_s)(T - T_0) \tag{6.43}$$

are the (uniform) film stress at the onset of yield (at temperature T_y) and the stress in the absence of plasticity, respectively. The solutions for the different defect energies differ only through the ϕ-dependence of λ.

6.6 Comparison of the non-local theory with DD simulations

6.6.1 The isotropic energy

The closed-form expression for the stress distribution (6.42) can readily be integrated over the film thickness to give the film-average stress as a function of h. Evidently, the solution depends on the values of four material parameters: E, ν, π_0 and ℓ. For the elastic constants we take the same characteristic values for aluminum ($E = 70$GPa and $\nu = 0.33$) as in the DD simulations presented in Sec. 6.4. The initial shear strength π_0 is taken from the DD results to be $\pi_0 = 15.5$MPa, corresponding to a film stress of $4/\sqrt{3}\pi_0 = 36$MPa [14]. Yield in the DD simulations is determined by the strength of the weakest dislocation source. The values of the source strengths in the simulations were chosen out of a Gaussian distribution with average $\tau_{nuc} = 25$MPa and standard deviation of 5MPa.

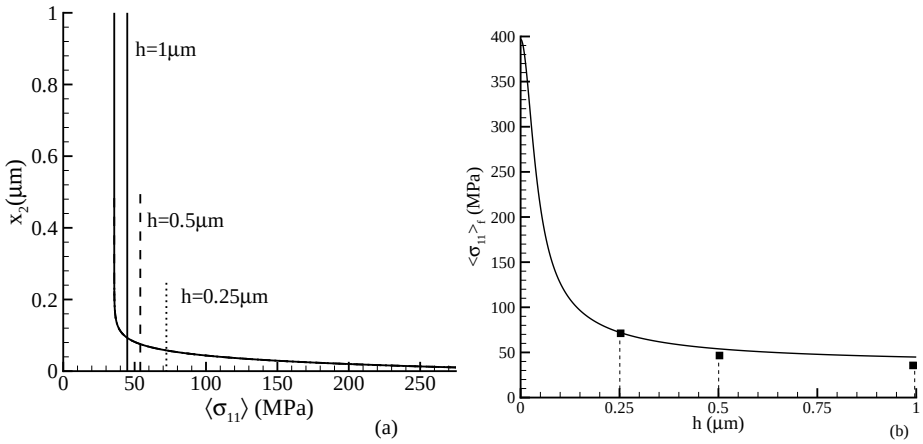

Figure 6.5 Predictions according to the isotropic defect energy theory, eq. (6.16), for $\phi = 30^\circ$ with $\ell = 1.8\mu$m at the same final temperature as in Fig. 6.2. (a) Profiles of the in-plane stress across the film thickness. Vertical lines indicate the average stress in the films, which are plotted in (b) as a function of film thickness h (scaling behavior $\langle\sigma_{11}\rangle_f \propto \tanh\lambda h/\lambda h$). Square symbols indicate the data points from the DD simulations.

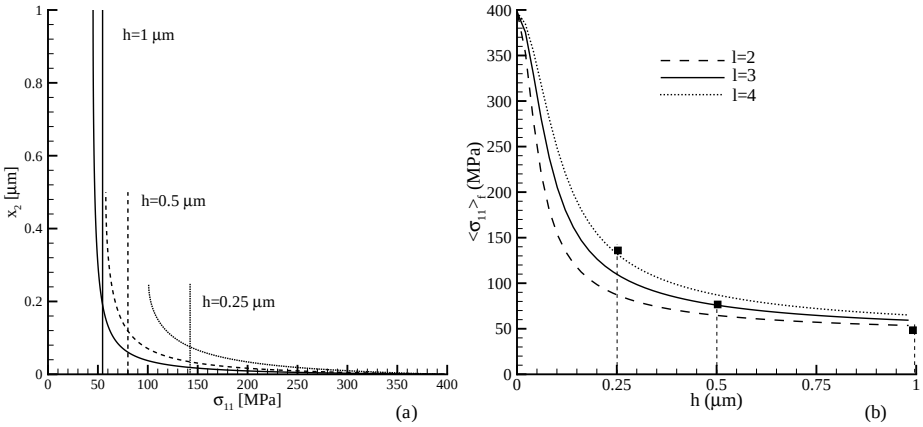

Figure 6.6 Predictions according to the isotropic defect energy theory, eq. (6.16), for $\phi = 60^\circ$ at the same final temperature as in Fig. 6.3. (a) Profiles of the in-plane stress across the film thickness with $\ell = 1.8\mu$m. (b) The average film stress as a function of film thickness h for three values of ℓ: $\ell = 2$, 3 and 4μm. Square symbols indicate the data points from the DD simulations.

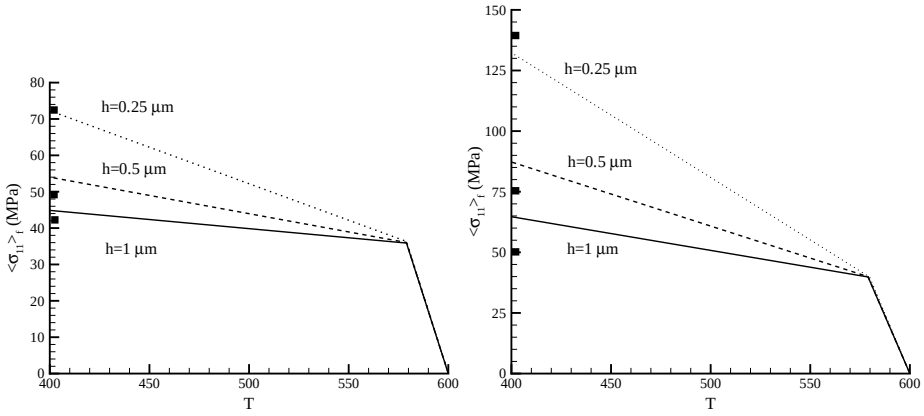

Figure 6.7 Film-average stress-temperature curves according to the strain gradient solution eq. (6.42) according to the isotropic defect energy theory, eq. (6.16), for (a) $\phi = 30^\circ$ with $\ell = 1.8\mu$m and (b) for $\phi = 60^\circ$ with $\ell = 4\mu$m. Square symbols indicate the stress at final temperature in the DD simulations, as shown also in Figs. 6.2, 6.5 and Figs. 6.3, 6.6.

The only parameter left free is the length scale ℓ originating from (6.16). It is clear from eq (6.42) that the DD results for the two crystal orientations cannot be fitted using a single value of the material parameter ℓ: the equation depends on ϕ only through $\sin 2\phi$, which is the same number for $\phi = 60^\circ$ and $\phi = 30^\circ$. A value of $\ell = 1.8\mu$m gives a $\langle\sigma_{11}\rangle_f$–$h$ curve which agrees quite well with the DD data points in the case of ϕ_{30}, as shown in Fig. 6.5b. We tried, without success, to find a value of ℓ giving a similar fit to the $\langle\sigma_{11}\rangle_f$–$h$ dislocation data for the slip plane orientation with ϕ_{60}. Figure 6.6b shows three curves for $\ell = 2$, 3 and 4μm, each of them agreeing only with the DD data for a single particular thickness h. Figures 6.5a and 6.6a show the stress profiles across the film height according to (6.42), which indeed exhibit a stress gradient. Another noteworthy feature of the solution is that the stress at the film–substrate interface is independent of h, and equal to the elastic stress σ_n, eq. (6.43). Figure 6.7, finally, shows the stress–temperature curves given by the solution (6.42), which reinforces the difficulties in obtaining a good fit for ϕ_{60}.

6.6.2 The S0 Defect Energy

The solution for this theory, with $f(\phi)$ according to (6.37), also has only the length scale ℓ as a free material parameter. For $\ell = 1.5\mu$m it is possible to fit the DD

results for the ϕ_{30} orientation, but the solution for the same material length scale for the orientation ϕ_{60} does not match the DD results. The curves in Fig. 6.8 show an opposite trend with respect to the DD predictions: the size effect is smaller for the ϕ_{60} orientation than for the ϕ_{30}.

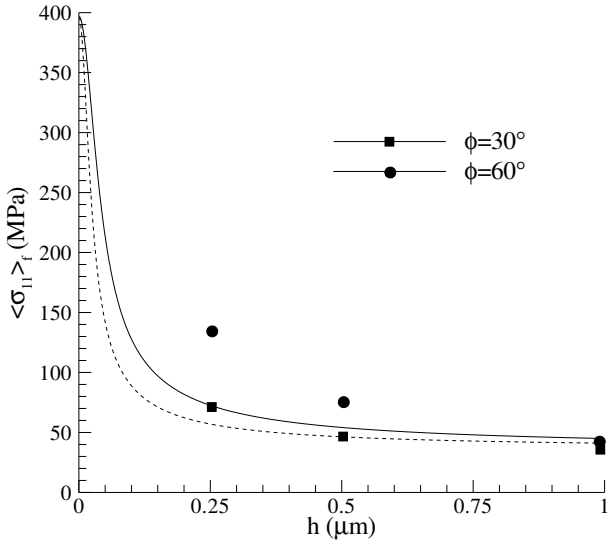

Figure 6.8 Average stress in the films versus film thickness *h* predicted by the S0 defect energy theory, eq. (6.19), for $\phi = 30^\circ$ and $\phi = 60^\circ$. The symbols represent the discrete dislocation results.

6.6.3 The S Defect Energy

In this case, with $f(\phi)$ according to (6.38), there is an additional free parameter, *k*, beside the material length scale ℓ. This allows for a good fit of the two orientations, provided that *k* is different for the ϕ_{30} and for the ϕ_{60} orientation. In particular, *k* must be positive for the ϕ_{30} orientation, negative for the ϕ_{60}. Figure 6.9 shows the fit obtained for $\ell = 3\mu$m.

6.6.4 The Pile-up Defect Energy

By considering the free energy in the form of the pile-up defect energy, eq. (6.20), we again have only one free material parameter for the fit with the simulations, ℓ. Even though the fit shown in Fig. 6.10 is not as good as the one obtained for the

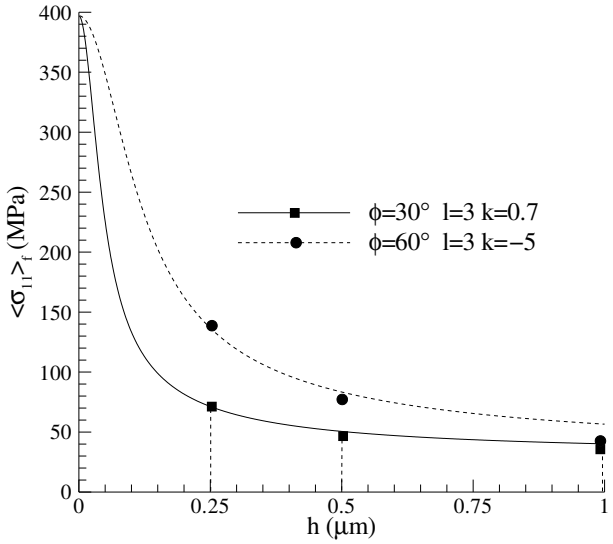

Figure 6.9 Film-average tensile stress as a function of film thickness *h* for two orientations according to the S-theory.

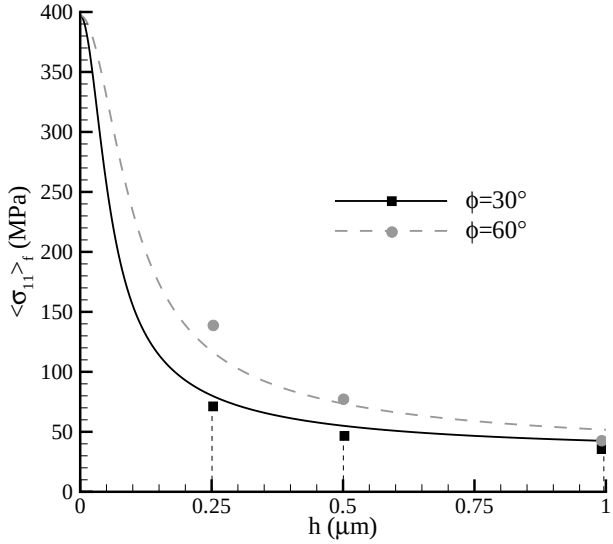

Figure 6.10 Film-average tensile stress as a function of film thickness *h* for two orientations according to the pile-up theory.

S-energy, there still is a quite good agreement for $\ell = 3\mu$m. It is worth noticing that the S-energy reduces to the S0-energy for $k = 0$, to the pile-up energy for $k = 1 - 1/4\cos^2\phi$ ($k_{30} = 0.\overline{5}$, $k_{60} = -3$).

6.7 Conclusions

Different forms for the free energy in Gurtin's strain gradient plasticity theory have been discussed. The problem of a thin film strained by a large substrate during cooling has been solved by discrete dislocation plasticity simulations and by the strain gradient theory, using different expressions for the free energy. The best fit between simulations and theory has been found for a defect energy in the form of a pile-up energy.

References

[1] H.H.M. Cleveringa, Discrete Dislocation Plasticity, PhD Thesis, ISBN 90-423-0091-4.

[2] H.H.M. Cleveringa, E. Van der Giessen, A. Needleman, Acta Mater. **45** (1997) 3143.

[3] J.W. Hutchinson, Int. J. Solid Struct **37** (2000) 225.

[4] A. Needleman, Acta Mater. **48** (2000) 105.

[5] E.C. Aifantis, Int. J. Eng. Sci. **30** (1992) 1279.

[6] E.C. Aifantis, Int. J. Frac. **95** (1999) 299.

[7] N.A. Fleck, J.W. Hutchinson, Adv. Appl. Mech. **33** (1997) 295.

[8] N.A. Fleck, J.W. Hutchinson, J. Mech. Phys. Solids **49** (2001) 2245.

[9] J.L. Bassani, J. Mech. Phys. Solids **49** (2001) 1983.

[10] Y. Huang, H. Gao, W.D. Nix, J.W. Hutchinson, J. Mech. Phys. Solids, **48** (2000) 99.

[11] M.E. Gurtin, J. Mech. Phys. Solids **48** (2000) 989.

[12] M.E. Gurtin, J. Mech. Phys. Solids **50** (2002) 5.

[13] M.E. Gurtin, Int. J. Plast. **19** (2003) 47.

[14] L. Nicola, E. van der Giessen and A. Needleman, J. Appl. Phys **93** (2003) 5920.

[15] L. Nicola, E. van der Giessen, A. Needleman, submitted for publication.

Chapter 7

Freestanding thin films under tensile loading: a comparison with experiments

While previous chapters were concerned with structures on top of large substrates, this chapter deals with free-standing thin films. The tensile deformation is now applied directly to the film rather than via the substrate. Vlassak and co-workers at Harvard University employ a bulge test machine that offers the possibility of performing a tensile test under plane strain conditions [1]. The latter provides an excellent opportunity for our two dimensional plane strain discrete dislocation plasticity simulations to be confronted with experiments.

Xiang et al. [1] find a thickness dependent response of passivated films that is qualitatively similar to the one we found for polycrystalline films on a substrate [2] (see chapter 4). By simulating free-standing thin films under tension, we intend to reproduce the experimental curves, by fitting some of the unknown parameters we have used in previous simulations, such as dislocation source density and strength. The dependence of hardening on the presence of a passivation layer is also analyzed.

7.1 Main experimental results obtained by Xiang et al.

To start with, freestanding Cu films have been prepared with various thickness ($h = 0.98$, 1.9 and 4.2 μm) but constant microstructure [1]. This is achieved by vacuum annealing 5.2 μm thick Cu membranes at high temperature to stabilize the grain size and by subsequently thinning them to the required thickness by mechanical polishing. For each thickness three specimens are prepared: (i) with no passivation, (ii) with one side passivated by 20 nm Ti, (iii) with both sides passivated.

After preparation the specimens are analyzed to check if the microstructure is effectively independent of the specimen thickness. As expected, both grain size

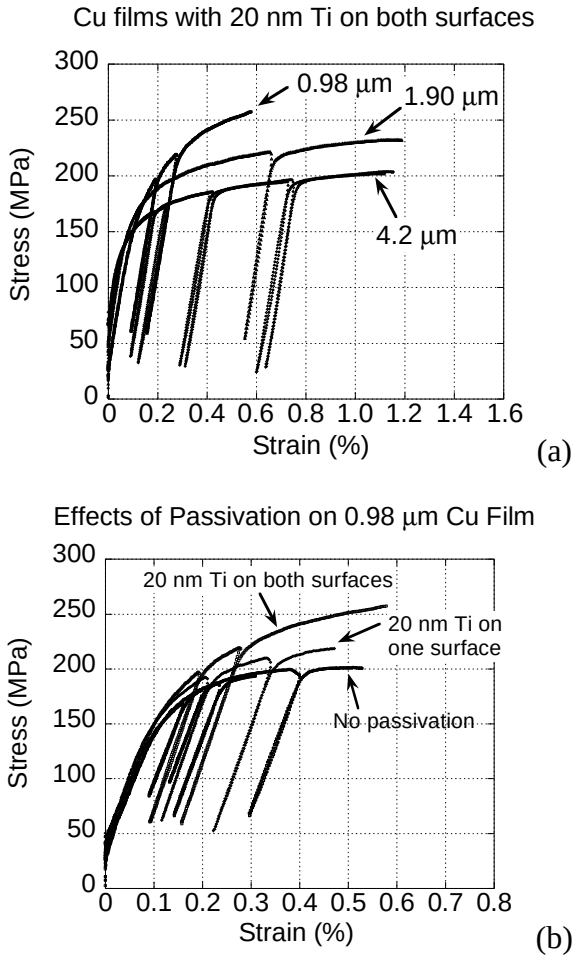

Figure 7.1 (a) Size effect in passivated freestanding films. (b) Influence of the presence of passivation layers (from [1]).

and crystallographic texture are found to be roughly the same in the different films. The mean grain size ranges from $d = 2.4\mu$m in the thinnest film to $d = 2.9\mu$m in the thickest. TEM observations show the presence of extensive twinning in all specimens and absence of dislocations.

The results of the experiments are summarized in Fig. 7.1. Figure 7.1a shows stress-strain curves as a function of film thickness for the films with both surfaces passivated; the size effect is evident. Figure 7.1b shows the effect of the coating

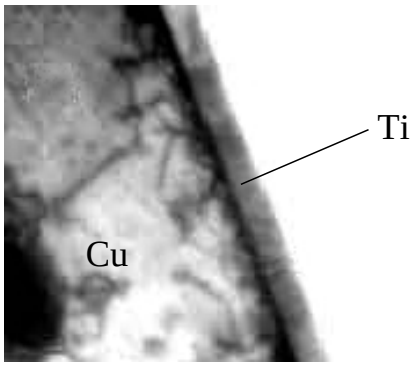

Figure 7.2 Dislocation pile-ups close to the Cu–Ti interface after deformation (from [1]).

on hardening for the thinnest films. Hardening of the thinnest film increases with the number of passivated surfaces. For the thicker films the effect is much less pronounced [1].

After deformation (up to 0.35% residual strain) the specimens are again observed at the TEM. It is observed that many dislocations have piled up close to the film–coating interface (see Fig. 7.2). The thickness of the layer with high dislocation density is only around 50 nm.

7.2 Two-dimensional model for a freestanding film

The free-standing film is modeled as an infinite array of rectangular grains of height h and width d. The film is periodic in x_1-direction with periodicity w. The unit cell is taken to contain eight grains, each of them characterized by a certain crystal orientation, given by the orientation of three sets of slip systems. The angle between the three sets of parallel slip planes in a grain is 60°. The orientation of the grain is identified by the angle ϕ at which the three sets of planes are inclined with respect to the film–coating interface. The angle ϕ for each grain is chosen at random. Two passivation layers of thickness p are coating the film.

Tension is imposed by a uniform displacement difference between cells that linearly increases in time. While the passivation layers respond elastically, plastic relaxation occurs in the film by glide of edge dislocations on the slip planes in the grains. The grain boundaries as well as the film–coating interfaces are taken to be

flat and perfectly impenetrable for dislocations. Since the elastic constants of the film (Cu) and the coating (Ti) are very similar, we take them to be the same in the simulations. Elastic anisotropy is ignored.

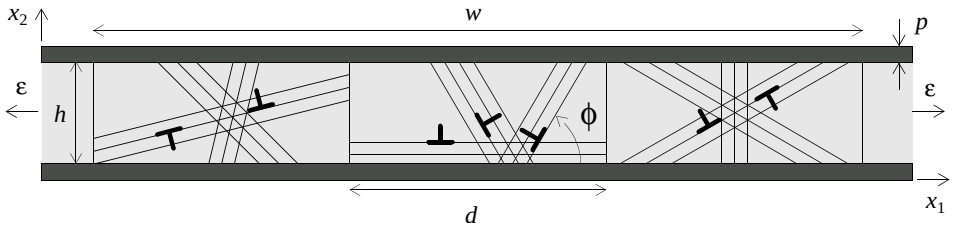

Figure 7.3 Two-dimensional model of a freestanding passivated thin film under tensile loading.

7.3 Method of analysis

The solution of the problem is obtained using the Van der Giessen-Needleman approach presented in [3]. The methodology is based on the solution of an elastic boundary value problem for the unit cell, with boundary conditions changing while the dislocation structure evolves. The complete solution is obtained, at each incremental step of the simulation, by adding the singular elastic fields of the discrete dislocations to the solution of the boundary value problem.

The governing equations for the boundary value problem, which is solved here by finite elements, are

- the equilibrium condition

$$\sigma_{ij,j} = 0 \tag{7.1}$$

- the compatibility equation

$$\varepsilon_{ij} = \frac{1}{2}(u_{i,j} + u_{j,i}) \tag{7.2}$$

- the constitutive equation

$$\varepsilon_{ij} = \frac{1+\nu}{E}\left(\sigma_{ij} - \frac{\nu}{1+\nu}\delta_{ij}\sigma_{kk}\right). \tag{7.3}$$

Tensile loading is prescribed by enforcing

$$u_i(0,x_2) = u_i(w,x_2) + U\delta_{i1} \tag{7.4}$$

at the periodic boundaries of the unit cell (δ_{ij} is the Kronecker delta). The cell-to-cell displacement $U = U_0 + \int \dot{U} dt$ increases linearly with time and determines the overall tensile strain as $\varepsilon = U/w$. At the top and bottom surfaces traction-free conditions are prescribed,

$$\sigma_{12}(x_1,0) = \sigma_{22}(x_1,0) = 0, \qquad \sigma_{12}(x_1,h+2p) = \sigma_{22}(x_1,h+2p) = 0\,, \tag{7.5}$$

where p is the thickness of the passivation layer.

Additional constitutive equations are introduced to determine the evolution of the dislocation ensemble, governed by the resolved shear stress on the slip planes. The rules control nucleation of the dislocation dipoles from point sources, dislocation glide, annihilation and pinning of dislocations at point obstacles. The simulations start from a dislocation free state and with sources randomly distributed on the slip planes. Each source is characterized by a critical nucleation strength τ_{nuc}, chosen out of a Gaussian distribution of strengths. A source becomes active when the resolved shear stress on it is larger than τ_{nuc} for a time span t_{nuc}. When this happens, a dislocation couple is generated: two dislocations of opposite sign are introduced on the slip plane at a distance L_{nuc}. This distance is such that the attractive stress field that the dislocations exert on each other is equilibrated by the resolved shear stress at nucleation (τ_{nuc}):

$$L_{\text{nuc}} = \frac{\mu}{2\pi(1-\nu)} \frac{b}{\tau_{\text{nuc}}}\,. \tag{7.6}$$

After nucleation, dislocations glide, driven by the Peach-Koehler force acting on them. For any dislocation I the Peach-Koehler force is computed as

$$f^{(I)} = n_i^{(I)} \left(\hat{\sigma}_{ij} + \sum_{J \neq I} \sigma_{ij}^{(J)} \right) b_j^{(I)}\,, \tag{7.7}$$

with $n_i^{(I)}$ denoting the normal to the slip plane of dislocation I and $b_j^{(I)}$ its Burgers vector. Here, $\tilde{\sigma}_{ij}^{(J)}$ is the long-range, singular stress field of dislocation J and $\hat{\sigma}_{ij}$ is the image stress field computed by finite elements. Dislocation climb is not accounted for. In case two opposite signed dislocations are closer to each other than the critical distance L_{ann} they are supposed to annihilate and are removed

from the calculation. Impenetrable point obstacles are present at grain boundaries and at the film–coating interface. When a dislocation arrives at an obstacle, it gets pinned there.

The conditions (7.4) and (7.5) prescribed at the boundaries of the unit cell are not sufficient to find a solution for our problem. It is necessary to apply an additional constraint in order to prevent rigid body motion of the structure. This is done by fixing a single node of the mesh; for instance by prescribing

$$u_i(0,0) = 0. \tag{7.8}$$

Due to the periodic nature of the problem, this condition corresponds to imposing $u_i(0,nw) = 0$, for $n = 0,1,2....$ This leads to a correct uniform solution as long as the response is elastic. As soon as dislocations are nucleated, the uniformity of the field brakes down and because of the constraint imposed by the fixed nodes, the film starts to bend. With increasing plastic deformation, a wave of period w forms in the film. This is directly seen in the deformed mesh shown in Fig. 7.4 but can also be recognized in the stress distribution in Fig. 7.5.

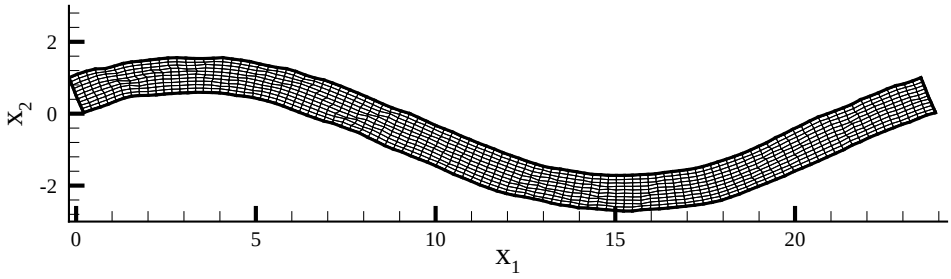

Figure 7.4 Deformed mesh for a passivated film with boundary conditions (7.4), (7.5) and (7.8) at 0.5% imposed strain. The displacements are magnified by a factor 20 for visibility.

This pronounced bending is quite unrealistic. Real films, extended in the out-of-plane direction, will not exhibit this behavior since the columnar grains are constrained by adjacent grains located in front of and behind the plane of view; this is illustrated schematically in Fig. 7.6. These grain-grain interactions are likely to constrain the film deflection in the x_2 direction. In order to mimic this with our two dimensional model, we consider it more appropriate to impose an additional constraint, namely zero vertical displacements along the centerline,

$$u_2(x_1, h/2) = 0. \tag{7.9}$$

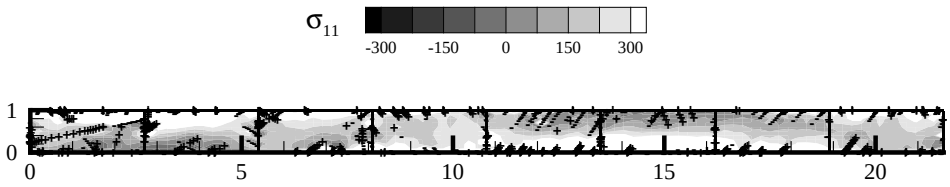

Figure 7.5 Stress and dislocation distribution at 0.5 % applied strain for the passivated film in Fig. 7.4.

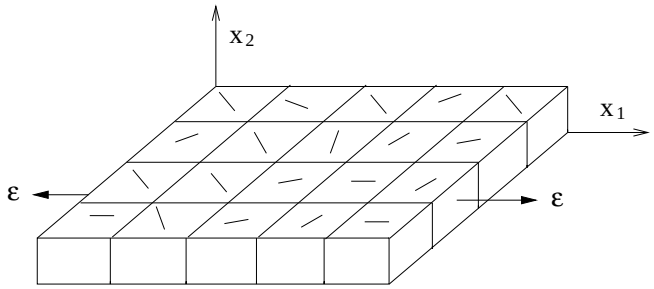

Figure 7.6 Schematic representation of a freestanding film in three dimensions: surrounding grains have different crystal orientations.

To test to which extent the condition (7.9) controls a mesh dependent response, simulations are carried out for passivated films of grain size $d = 2.7\mu$m using condition (7.9), or a weaker form of it,

$$u_2(nd, h/2) = 0, \qquad n = 0, 1, 2... \tag{7.10}$$

where only the grain boundaries are constrained. Curves for the average tensile stress,

$$\langle \sigma_{11} \rangle = \int_0^w \int_0^{h+p} \hat{\sigma}_{ij} + \sum_J \sigma_{ij}^{(J)} dx_1 dx_2$$

versus strain are shown in Fig. 7.7. The third curve is the response of the simulation shown in Fig. 7.4 and 7.5, based on (7.8) without any prescription at the middle nodes. Considering that the results for boundary condition (7.9) and (7.10) do not differ much, we choose to continue the analysis by using condition (7.9).

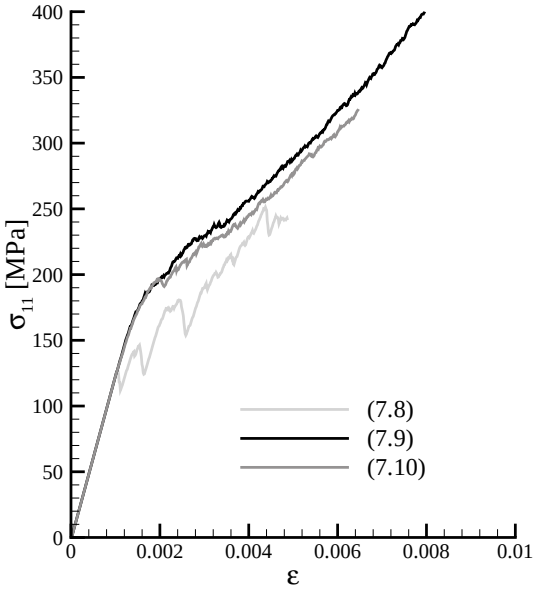

Figure 7.7 Stress–strain curves for freestanding passivated films with different b.c.

7.4 Numerical results

7.4.1 Effect of film thickness on the plastic response of coated films

The simulations are performed for films of the same thickness as tested by Xiang et al. [1], $h = 1$, 1.9 and 4.2 μm. The choice of a grain size d suitable for the comparison is less straightforward: the average grain size reported by [1] is $d = 2.7\mu$m, but the presence of many twins suggests the necessity of considering a higher density of grain boundaries. Since twinning is accompanied by crystal rotation, we will model twins in the same way we model grains. Hence, for the simulations we take $d = 1.5\mu$m, the average grain size measured in the specimens when twins are included.

The films are passivated on both sides by elastic coatings of thickness $p =$ 20nm. The films are subjected to a displacement rate of $\dot{U} = 3 \times 10^4 \mu\text{m/s}$.

The calculations start with stress free and dislocation free films. Dislocation sources are evenly distributed among the grains, randomly positioned on the slip planes. Parallel slip planes are spaced by 200 Burgers vectors. The density of dislocation sources, their average critical strength and standard deviation are un-

known values and therefore are treated here as the parameters that can be fitted to the experimental results. The average stress-strain curves are shown in Fig. 7.8. A reasonable fit to the experimental results for all thicknesses (see Fig. 7.1a) is obtained by using a source density of $15/\mu m^2$ with a mean strength of 100 MPa and a standard deviation of 20 MPa. The source density mainly determines the hardening rate (here hardening is approximately linear) and the source strength determines the flow strength. Results are strongly dependent on these two values. On the contrary, dependence on the standard deviation of the source strength distribution is found to be very weak. While in single crystal simulations it is essential that this value is different from zero to prevent simultaneous nucleation of sources on slip planes with the same Schmid factor (see chapter 2), the variety of slip plane orientations accounted for in polycrystals is already sufficient to ensure that the nucleation events occur at different moments.

Figure 4.7 shows stress state and dislocation distribution in the films at 0.35% residual strain. Grain boundaries are characterized by a high dislocation density. Hard boundary layers are present at the film–coating interfaces.

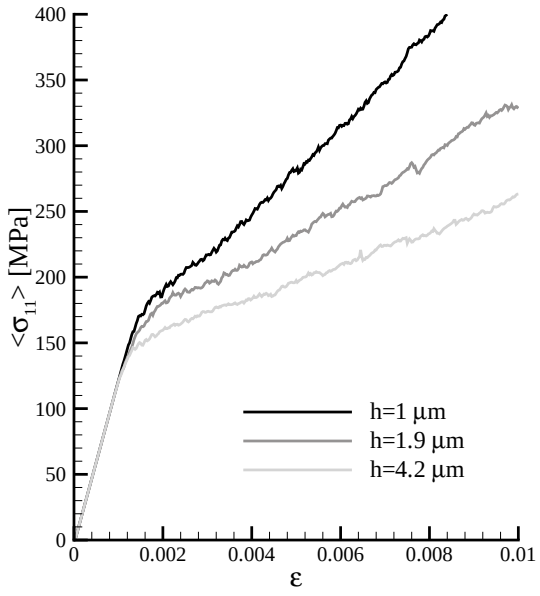

Figure 7.8 Size effect: simulated stress-strain curves for free-standing films with double-sided passivation.

7.4.2 Effect of passivation layer

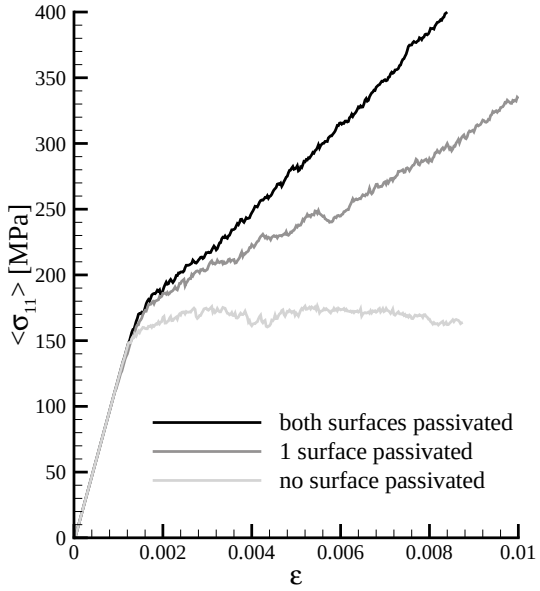

Figure 7.9 Effect of the presence of passivation layer(s) on hardening.

Figure 7.9 shows the average stress $\langle\sigma_{11}\rangle$ versus strain curves for the thinnest film without passivation, and with one or both sides passivated. In agreement with the experiments (see Fig. 7.1b), the simulations show that hardening increases with the number of passivation layers. But, while in experiments hardening occurs even for bare films, the simulated bare film does not harden. The reason for this is that two-dimensional discrete dislocation simulations are able to capture hardening only if sufficiently many dislocations remain inside the film, pinned either at obstacles or boundaries. The reason is that the presence of discrete dislocations influences the stress state at the sources and therefore the nucleation activity. In the case of a bare film, coatings are not present to stop dislocations from leaving the film surfaces and the density of grain boundaries is too low to stop a significant number of dislocations. A few sources on slip planes that do not cross grain boundaries carry out most of the relaxation by continuously nucleating dislocations that subsequently glide out of the film. Contrary to simulations of passivated films, simulations of bare films are strongly dependent on the standard deviation of dislocation strength: the weakest sources are responsible for the

whole relaxation and the strongest never get activated.

7.5 Conclusions

In this chapter a comparison between experimental results and results of discrete dislocation plasticity simulations of free-standing films under tension has been presented. Experimental results and discrete dislocation simulation results are in qualitative good agreement: they both capture the thickness dependent hardening of passivated films and a dependence of hardening on the presence of passivation layers. The best fit has been obtained by using a source density of $15/\mu m^2$ with a mean strength of 100 MPa and a standard deviation of 20 MPa.

References

[1] Y. Xiang, J.J. Vlassak, M.T. Perez-Prado, Mat. Res. Soc. Symp. Proc. **795** (2003).

[2] L. Nicola, E. Van der Giessen, A. Needleman, J. Mater. Res., in press.

[3] E. Van der Giessen, A. Needleman, Simul. Mater. Sci. Eng. **3** (1995) 689.

Chapter 8

Discussion and outlook

The simple model presented in this thesis has proved to be capable of capturing thickness dependent hardening in thin metal films under tensile loading. What causes a size effect in these simulations is the formation of dislocation pile-ups at the interface between film and substrate (see chapters 2, 3 and 4) or film and coating (chapters 4 and 7). The back stress associated to these pile-ups has proved to be the major cause for thickness-dependent hardening (chapter 3).

The formation of a boundary layer has been shown to occur in films with a perfectly impenetrable interface with the substrate (or coating) while it does not occur if the interface is perfectly absorbing (see chapter 3). A more realistic view of the formation of a boundary layer could be obtained by modelling the interface as being partially capable to absorb dislocations, as in the case of an interphase. The numerical difficulty that arises when dislocations penetrate the substrate is the proper treatment of the displacement step that each dislocation would leave.

A similar remark can be made about grain boundaries in polycrystalline films: modeling them as impenetrable, flat and unidimensional (in two dimensions) is restrictive. In case the boundary were partially penetrable, the grain–size dependent hardening found in chapter 5 would probably be less pronounced. The difficulty in modelling partially penetrable grain boundaries in this framework is in the fact that dislocations, by moving from one grain into another, must climb on a slip plane with different orientation.

A difference in the interface boundary layer as well as in the surface boundary layer found for polycrystalline films with small grains (see chapter 5) can be expected if nucleation from interface and free surface were accounted for. By modelling generation of a new dislocation loop as a dislocation pair at the nucleation distance L_{nuc} (see chapter 1), the sources need to be placed at a distance $\frac{1}{2}L_{\text{nuc}}\sin\phi$ from interface or surface in order for the freshly generated couple to be contained inside the film. Therefore, there is a thin layer close to interface, free surface and grain boundary where dislocation sources are absent. If sources were

present also there, the boundary layer would be less uniform and the size effect less pronounced.

The effect of having nucleation partly occurring from the interface, the surface and grain boundaries would very likely only decrease hardening, so that the size effect would simply shift to smaller film thickness. Nevertheless, since experiments and molecular dynamics simulations suggest that nucleation in thin films occurs predominantly from grain boundaries and interfaces, it would be interesting to model sources accordingly, since this could affect the results of the simulations substantially.

What is certainly missing in this model are three-dimensional effects, such as line tension and dynamic formation of dislocation entanglements. In the present two-dimensional model dislocations form entanglements only if their edge parts meet in the plane of deformation. Interactions of dislocations on other planes are not accounted for. This is evident in the results of the simulation of the unpassivated freestanding thin film presented in chapter 7, for which hardening never occurs. Three-dimensional discrete dislocation plasticity models would be more appropriate to address this problem, or at least a two-dimensional model as the one proposed by Benzerga et al. [1], where three-dimensional effects are partly incorporated. With such a model, hardening of unpassivated films could be captured for a large enough strain, by increasing the density of forest dislocations during deformation.

Three-dimensional discrete dislocation plasticity simulations are at present computationally very expensive, due to the difficulty in treating the boundary conditions and the complicated line shapes and interactions [2]. In addition, the number of mechanisms included and numerical algorithms involved, makes the interpretation of the results quite difficult and may not add to a significant improvement of understanding.

References

[1] A.A. Benzerga, Y. Brechet, A. Needleman, Modelling. Simul. Mater. Sci. Eng. **12** (2004) 159.

[2] D. Weygand, L.H. Friedman, E. Van der Giessen and A. Needleman, Modelling. Simul. Mater. Sci. Eng. **10** (2002) 437.

Summary

According to experimental findings there are types of loading for which it is more difficult to plastically deform small metal structures than the corresponding massive metal. This occurs when at least one of the dimensions of the structure is at the micrometer scale or smaller. It is for instance the case of thin metal coatings: the thinner is the film, the more difficult it is to deform it plastically. This feature is in contrast with what expected on the basis of classical plasticity theories, which predict a size-*in*dependent mechanical response.

In this thesis the size effect in thin films is studied by means of two-dimensional discrete dislocation plasticity. Plasticity is treated as the collective motion of edge dislocations on prescribed slip systems. The framework contains an intrinsic length scale –the dislocation Burgers vector– which is a necessary condition to capture a size effect.

After a brief introduction of the method in the first chapter, attention is focused on the mechanical behavior of single crystal thin films on a large substrate (chapters 2 and 3). The practically relevant loading studied is that the film-substrate system is being subjected to a change in temperature. Tensile stress develops in the film during cooling, due to the difference in the coefficients of thermal expansion of film and substrate. Stress relaxation by plastic deformation in films that are between 0.25 and 1μm thick (chapter 2) is found to be dependent on this film thickness. The thickness dependence of the resulting film stress is in good qualitative agreement with the experimental findings. The origin of this size effect is the formation of a hard boundary layer comprising dislocation pile-ups at the film–substrate interface, which is modelled as impenetrable for the dislocations. Since the layer does not scale with film thickness, its contribution to the overall response increases with decreasing film thickness, hence giving rise to the size effect. Nevertheless, as shown in chapter 3, the boundary layer is not the only cause for the size effect in thin film: films thinner than a material-dependent threshold-thickness harden mainly because of insufficient nucleation activity.

Chapter 4 is devoted to the analysis of stress relaxation in single crystal metallic interconnects for integrated circuits. A cross–sectional analysis of the line is

carried out, with plane strain condition imposed in the direction along the line. The dependence of stress development and relaxation on line size and aspect ratio is explored. Stress relaxation by dislocation glide is not effective in lines with hight-to-width aspect ratio close to unity, for which the stress is almost hydrostatic. In lines with a smaller aspect ratio relaxation is quite effective in the center of the line, with dislocations forming boundary layers at the top and bottom of the interconnect. The presence of this boundary layers is responsible for a size effect in lines with a small cross-section.

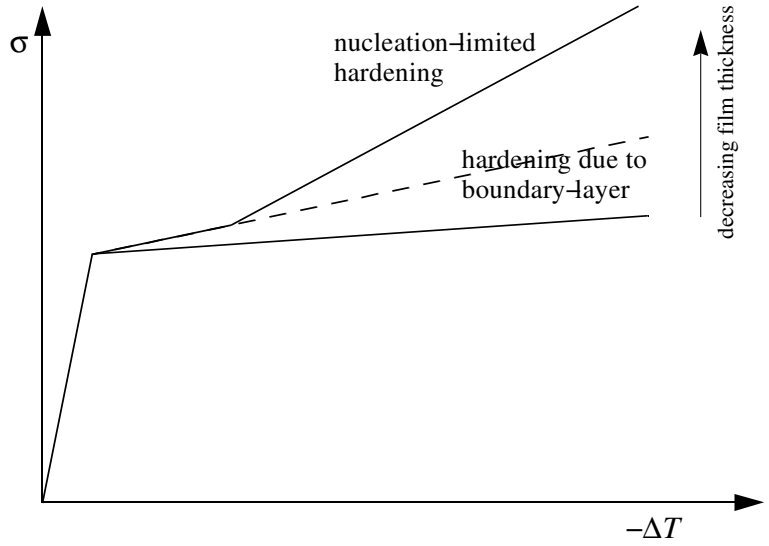

Figure 1 Schematic summary of the two hardening mechanisms found in crystalline thin films on a hard substrate. Average film stress is σ, temperature rise is ΔT.

In chapter 5 the thin film problem analyzed in chapters 2 and 3 is extended to polycrystalline films. The columnar grains, of which deposited films are generally made of, are modelled as rectangular single crystals of constant width. In this way a new length scale is introduced, i.e. the grain size, which gives an additional microstructural constraint to stress relaxation. The model permits to independently vary film thickness and grain size. The simulations show both film-thickness and grain-size dependent hardening. The latter is known in bulk as the Hall-Petch effect, but its scaling relation does not seem to apply to thin films.

An alternative to discrete dislocation plasticity is to develop a nonlocal version

of standard continuum plasticity theory so as to introduce a material length scale. The form of such a theory is not known however, and several formulations can be found in the literature. In chapter 6 the strain gradient plasticity theory proposed by Gurtin [1] for single crystals is discussed. This theory attributes the nonlocal or gradient effect to the net Burgers vector of dislocations; this makes it well suitable for a comparison with discrete dislocation simulations. Different forms for the defect energy in the strain gradient theory are proposed and then used to solve the thin film problem of chapter 2. By comparing the solutions with the results of the simulations, it is possible to fit the length scales appearing in Gurtin's theory. The best fit is found for a defect energy that is proportional to the energy in dislocation pile-ups.

While all previous chapters dealt with films on a strong substrate, the last chapter supplements this with a study of free-standing thin films. Discrete dislocation simulations of such films under tension are confronted against experimental results in which grain size and film thickness are varied independently. The experimental work is carried out by Xiang and Vlassak [2] on a bulge testing machine, where the specimens are kept under plane strain conditions, which should support the assumption of a two-dimensional problem. Stress-strain curves show a size effect for passivated films of thickness ranging between 1 and 4.2 μm. Moreover, hardening is found to depend on the presence of passivation layers. The simulations are performed in order to reproduce the experimental curves by fitting two unknown parameters, namely the dislocation source density and strength.

References

[1] M.E. Gurtin, J. Mech. Phys. Solids, **50** (2002) 5.

[2] Y. Xiang, J.J. Vlassak, M.T. Perez-Prado, Mat. Res. Soc. Symp. Proc., **795** (2003) paper U11.37.

Samenvatting

Experimenten hebben laten zien dat er belastingssituaties zijn waarbij kleine metalen structuren moeilijker plastisch vervormbaar zijn dan hetzelfde materiaal in bulk. Dit doet zich voor wanneer minstens één van de afmetingen van de ordegrootte van een micrometer is of kleiner. Het verschijnsel treedt bijvoorbeeld op in dunne metalen coatings: hoe dunner de film, hoe moeilijker het is om deze plastisch te deformeren. Dit verschijnsel is in tegenspraak met klassieke plasticiteitstheoriën, die uitsluitend een schaal-*on*afhankelijke respons beschrijven.

Dit proefschrift handelt over de bestudering van dit schaaleffect in dunne lagen met behulp van een tweedimensionaal discrete-dislocatie plasticiteitsmodel. In dit model wordt plasticiteit beschreven door middel van het collectief gedrag van randdislocaties op voorgedefinieerde glijsystemen. Dit raamwerk bevat een intrinsieke lengteschaal –de Burgers vector van de dislocatie– hetgeen een noodzakelijke voorwaarde is om schaaleffecten te kunnen beschrijven.

Na een korte inleiding van de methode, in hoofdstuk 1, richt ik mij eerst op het mechanisch gedrag van één-kristallijne dunne lagen op een dik en stijf substraat. De praktisch relevante belastingssituatie is dat het film-substraat systeem onderworpen wordt aan een temperatuursverandering. Als gevolg van het verschil in thermische uitzettingscoëfficiënt tussen substraat (meestal silicium) en film ontstaat bij afkoeling een trekspanning in de film. De mate waarin deze spanning kan relaxeren door plastische deformatie blijkt, in films die tussen 0.25 and 1μm dik zijn, afhankelijk te zijn van die laagdikte (hoofdstuk 2). De resulterende spanning is laagdikte-afhankelijk op een wijze die in kwalitatief goede overeenstemming is met experimentele resultaten. De oorzaak blijkt te liggen in de vorming van een relatief harde grenslaag die een gevolg is van de opeenhoping van dislocaties aan de interface tussen film en substraat, die verondersteld wordt geen dislocaties door te laten. Aangezien de dikte van deze grenslaag niet schaalt met de dikte van de laag, is de relatieve bijdrage groter in dunne films waardoor de totale respons harder is. Echter, zoals in meer detail besproken wordt in hoofdstuk 3, is de grenslaag niet de enige oorzaak: beneden een materiaalafhankelijke drempelwaarde van de laagdikte treedt er additionele versteviging op wegens ge-

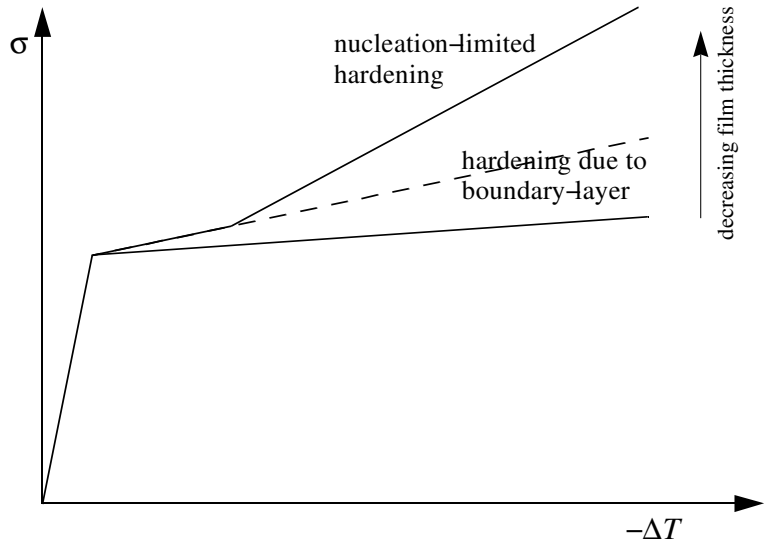

Figure 1 Schematische samenvatting van de twee gevonden verstevigingsmechanismen in kristallijne dunne lagen op een hard substraat. Gemiddelde spanning in de film is σ, temperatuurtoename is ΔT.

brek aan voldoende nucleatie van nieuwe dislocaties.

Hoofdstuk 4 behandelt de analyse van spanningsrelaxatie in één-kristallijne verbindingen in geïntegreerde schakelingen. Ook hier is weer een tweedimensionaal model gebruikt, d.w.z. van de dwarsdoorsnede van de lijn, onder de aanname dat er een vlakke vervormingstoestand heerst in de lengterichting van de lijn. De berekeningen zijn voornamelijk gericht op het achterhalen van de invloed van afmeting en vorm van de lijn op spanningsontwikkeling en relaxatie. Het blijkt dat spanningsrelaxatie door dislocatiebeweging niet effectief is in lijnen met een bijna vierkante doorsnede omdat de spanningstoestand dan vrijwel hydrostatisch is. In plattere lijnen treedt relaxatie vooral op in het midden van de doorsnede, terwijl zich grenslagen vormen aan boven- en onderzijde, tegen de passiveringslaag respectievelijk het substraat. Deze grenslagen zijn verantwoordelijk voor een schaaleffect in dunne lijnen.

In hoofdstuk 5 wordt het dunne-laagprobleem van hoofdstukken 2 en 3 uitgebreid naar polykristallijne films. Als gevolg van depositie zijn de kristallieten kolomvormig; ze worden gemodelleerd als rechthoekige korrels met een uniforme breedte. Aldus zijn er in polykristallijne films twee lengteschalen: de filmdikte en

de korrelgrootte. Beiden leggen beperkingen op aan spanningsrelaxatie en beiden kunnen onafhankelijk worden gevarieerd in het model. Uit de simulaties vinden we op deze manier dat versteviging zowel van filmdikte als van korrelgrootte afhangt. Het laatste effect is in bulk bekend als het Hall-Petch effect, maar de schalingsregelmatigheid in bulk lijkt niet op te gaan voor dunne lagen.

Een alternatief voor discrete-dislocatieplasticiteit is een niet-lokale versie van continuumplasticiteit om aldus een materieële lengteschaal te introduceren. De vorm van een dergelijke theorie is echter niet bekend, en er zijn diverse formuleringen in de literatuur te vinden. Hoofdstuk 6 behandelt één ervan, namelijk de kristalplasticiteitstheorie van Gurtin [1]. Deze theorie koppelt het niet-lokale of rekgradiëntseffect aan de netto Burgers vector van dislocaties. Dit maakt de theorie uitermate geschikt voor confrontatie met dislocatieplasticiteit. Ik bekijk verschillende functionele vormen voor de defect-energie, waarmee vervolgens het dunne-filmprobleem van hoofdstuk 2 wordt opgelost. Uit vergelijking met de discrete-dislocatieresultaten kunnen de lengteparameters in Gurtin's theorie worden gefit. De beste fit wordt gevonden met een defect-energie die evenredig is met de energie in dislocatie opeenhopingen.

In tegenstelling tot en in aanvulling op eerdere hoofdstukken, handelt hoofdstuk 7 tenslotte over vrijstaande dunne lagen. Discrete dislocatie berekeningen aan dergelijke films onder trek worden gezet tegenover experimentele resultaten waarin korrelgrootte en filmdikte onafhankelijk konden worden gevarieerd. De experimenten zijn verricht door Xiang en Vlassak [2] op een zgn. 'bulge-testing machine' waarbij de films in één richting in een vlakke vervormingstoestand gehouden worden ter onderbouwing van de tweedimensionale simulaties. Versteviging blijkt af te hangen van de aanwezigheid van passiveringslagen. Voor twee passiveringslagen vertonen de spanning-rek curves een schaaleffect voor filmdiktes tussen 1 en 4.2 μm. De twee belangrijkste vrije parameters in het model, namelijk de dichtheid van dislocatiebronnen en hun sterkte, zijn gefit aan de experimentele curves.

Verwijzingen

[1] M.E. Gurtin, J. Mech. Phys. Solids, **50** (2002) 5.

[2] Y. Xiang, J.J. Vlassak, M.T. Perez-Prado, Mat. Res. Soc. Symp. Proc., **795** (2003) paper U11.37.

Acknowledgements

I am most grateful to my supervisor Erik van der Giessen for his prompt guidance and encouragement during these years, for the many stimulating discussions and for giving me the chance of attending several conferences abroad.

I am very grateful to Alan Needleman, not only for his invaluable scientific insight, but also for correcting awkward English expressions in the papers he co-authored.

I would also like to thank Morton Gurtin for the long e-mail discussion on defect energy.

Chapter 7 could not have been written without the experimental work performed by Joost Vlassak and Yong Xiang.

I would also like to acknowledge the Reading Committee composed of Professors Jeff de Hosson, Hans de Raedt and Bart van Wees for their useful comments.

Lucia Nicola

Propositions
appended to the dissertation

Stress and dislocations in thin metal layers

Lucia Nicola
3 September 2004

1 Computer simulations in material science should be only intended as a tool for a better understanding of physical phenomena and an aid in the development of a suitable theory and not to mimic the real world as accurately as possible.

2 A model used to capture a size effect needs to contain at least one material length scale. However, the presence of several length scales, which is unavoidable in models based on discrete entities, makes the interpretation of the results not trivial.

3 Even though the predictions of the discrete dislocation plasticity model presented in this thesis are in qualitative good agreement with experiments, the attempt of finding a quantitative agreement by fitting the unknown parameters in the model to the experimental curves is not very meaningful, since the model does not incorporate all possible relaxation mechanisms.

4 As far as stress relaxation is concerned, the optimal shape for the cross-section of a passivated interconnect line is not a square.

5 Accurate measurements of hardness by micro-indentation are difficult to obtain. Simulations of indentation are also quite difficult: they are meaningful only if the contact area between indenter and specimen is represented accurately, which is easily obtainable only with flat indenters.

6 Glass-to-glass anodic bonding is an efficient and inexpensive technique which can be used in the production of chemical sensors. It only works, however, if the mobility of sodium ions in the coating layer on the anode glass wafer is lower than in the glass itself.